MODELLED RESPONSE OF THE ELECTRICALLY STIMULATED HUMAN AUDITORY NERVE FIBRE

by

Jacoba Elizabeth Smit

Submitted in partial fulfillment of the requirements of the degree
Philosophiae Doctor (Biosystems)
in the
Faculty of Engineering, the Built Environment and Information Technology
UNIVERSITY OF PRETORIA

April 2008

SUMMARY

Modelled response of the electrically stimulated human auditory nerve fibre

by

Jacoba Elizabeth Smit

Promotor	:	Prof T Hanekom
Co-promotor	:	Prof JJ Hanekom
Department	:	Electrical, Electronic and Computer Engineering
Degree	:	Philosophiae Doctor (Biosystems)

SUMMARY

This study determined whether the Hodgkin-Huxley model for unmyelinated nerve fibres could be more comprehensively modified to predict excitation behaviour at Ranvier nodes of a human sensory nerve fibre, as specifically applied to the prediction of temporal characteristics of the human auditory system. The model was developed in three phases. Firstly, the Hodgkin-Huxley model was modified to describe action potential dynamics at Ranvier nodes using recorded ionic membrane current data from single human myelinated peripheral nerve fibres. A nerve fibre cable model, based on a combination of two existing models, was subsequently developed using human sensory nerve fibre morphometric data. Lastly the morphological parameters of the nerve fibre model were changed to resemble a Type I peripheral auditory nerve fibre and coupled to a volume-conduction model of the cochlea.

This study is the first to show that the Hodgkin-Huxley model equations can be modified successfully to predict excitation behaviour of a generalised human peripheral sensory nerve fibre without using the Goldman-Hodgkin-Katz equations. The model includes a more comprehensive establishment of temperature dependence of the physiological and electrical parameters compared to existing models.

Two versions of the human Type I auditory nerve fibre model were developed, one simulating an undamaged (non-degenerate) fibre and another a damaged (degenerate) fibre. Comparison between predicted and measured results indicated similar transient and persistent sodium, as well as slow potassium ionic membrane currents to those found in generalised sensory nerve fibres. Results confirm that chronaxie, rheobase current, mean latency, threshold and relative refractory periods depend on the amount of degeneracy of fibres. The model could account for threshold differences observed between different asymmetric waveforms. The combination of persistent sodium and slow potassium ionic membrane currents could in part predict non-monotonic excitation behaviour observed experimentally.

A simplified method was developed to calculate electrically evoked compound action potential responses following neural excitation. It provided a computationally effective way to obtain an estimate of profile widths from the output of models that calculate neural excitation profiles, and an indirect way to estimate stimulus attenuation by calculating the value of the parameter that produces the best fit to experimental data. Results also confirmed that electrode arrays located closer to the modiolus produce more focussed neural excitation spread than more laterally located arrays.

KEY WORDS

human, auditory nerve fibre, computational model, Hodgkin-Huxley model, generalised sensory nerve fibre, ionic membrane currents, strength-duration time constant, evoked compound action potential, conduction velocity, temporal characteristics

OPSOMMING

Gemodelleerde gedrag van 'n elektries-gestimuleerde menslike ouditiewe senuweevesel

deur

Jacoba Elizabeth Smit

Promotor	:	Prof T Hanekom
Mede-promotor	:	Prof JJ Hanekom
Departement	:	Elektriese, Elektroniese en Rekenaar-Ingenieurswese
Graad	:	Philosophiae Doctor (Biosisteme)

SLEUTELWOORDE

mens, ouditiewe senuweevesel, berekeningsmodel, Hodgkin-Huxley-model, veralgemeende sensoriese senuweevesel, ioniese membraanstrome, sterkte-duur tydskonstante, ontlokte saamgestelde aksiepotensiaal, geleidingspoed, temporale eienskappe

OPSOMMING

In hierdie proefskrif is 'n moontlike uitbreiding van die Hodgkin-Huxley-model vir ongemiëliniseerde senuweevesels ondersoek. Die aanpassings is daarop gemik om die opwekkingsgedrag by Ranvier-nodes van 'n menslike sensoriese senuweevesel te kan voorspel, met spesifieke toepassing op voorspelling van temporale eienskappe van die menslike ouditiewe stelsel. Die model is in drie fases ontwikkel. Gemete ioniese membraanstroomwaardes vir 'n enkele, menslike gemiëliniseerde perifere senuweevesel is gebruik om aksiepotensiaaldinamika by Ranvier-nodes te beskryf. Daarna is morfometriese inligting van menslike senuweevesels gebruik om 'n toepaslike kabelmodel, wat op twee bestaande modelle gebaseer is, te ontwikkel. Laastens is morfologiese veranderlikes van hierdie model aangepas vir 'n Tipe I ouditiewe senuweevesel en aan 'n volume-geleidingsmodel van die koglea gekoppel.

Hierdie studie is die eerste wat bewys dat vergelykings van die Hodgkin-Huxley-model suksesvol aangepas kan word om opwekkingsgedrag van 'n algemene, menslike perifere sensoriese senuweevesel te voorspel, sonder om van die Goldman-Hodgkin-Katz-vergelykings gebruik te maak. In vergelyking met bestaande modelle bevat hierdie model 'n meer uitgebreide daarstelling van die temperatuurafhanklikheid van die fisiologiese en elektriese veranderlikes.

Twee weergawes van die menslike Tipe I ouditiewe senuweevesel-model is ontwikkel, waarvan een 'n onbeskadigde (nie-gedegenereerde) vesel en die ander 'n beskadigde (gedegenereerde) vesel voorstel. 'n Vergelyking van voorspelde en eksperimenteel gemete resultate het aangedui dat kortstondige en meer blywende natrium-, sowel as stadige kaliumioon-membraanstrome bestaan, soortgelyk aan wat in algemene sensoriese senuweevesels aangetref word. Die afhanklikheid van kronaksie, reobasisstroom, gemiddelde vertraging, drempels en relatiewe refraktêre periodes tot die hoeveelheid degenerasie van vesels is aangedui. Die model kon ook drempelverskille tussen verskillende asimmetriese golfvorms voorspel. Die kombinasie van blywende natrium- en stadige kaliumioon-membraanstrome kon, gedeeltelik eksperimenteel waargeneem, nie-monotone opwekkingsgedrag voorspel.

'n Vereenvoudigde metode is ontwikkel om die elektries ontlokte saamgestelde aksiepotensiaalreaksies van neurale opwekking, te bepaal. Die metode bied 'n berekeningseffektiewe manier om profielwydtes van die uitsette van modelle wat neurale opwekkingsprofiele bereken, te voorspel. Dit verskaf ook 'n indirekte manier om stimulusverswakking te bereken deur die waarde wat gemete resultate die beste voorspel, te bereken. Resultate het ook bevestig dat elektrodeskikkings nader aan die modiolus meer gefokusde neurale opwekkingsverspreidings voorspel as meer laterale elektrodeskikkings.

Acknowledgements

I acknowledge and thank the following persons for the role they played in my life during this research period:

My parents and sister for their love, support and encouragement during this time.

Friends who had endured the up and downs that accompany a research degree. Sincere thanks for all the support and encouragement, the cups of coffee and tea, conversations, emails and good energy!

Many others including family, acquaintances and fellow students whose kind enthusiasm for my pursuit has kept me going.

Specifically My promotors for their interest in the study. Jackie Nel and Raymond Sparrow for valuable discussions on aspects of Physical Chemistry and biological membrane properties. Hans Grobler for expert administration of the computing clusters in the Engineering Faculty and for technical assistance. Linda Pretorius for advise on writing and editing. Niel Malan for introducing me to LaTeX. Walter Meyer for support and encouragement. Mrs Barbara Bradley for patiently proofreading the thesis. Mrss Hannetjie Boshoff and Annamarie Bezuidenhout, the two angles in the library who can perform miracles obtaining interlibrary loans.

Anyone else who do not fall under any of the above categories, but has played a part – no matter how small.

Lastly, my Creator and giver of inspiration.

This research has been supported by the National Research Foundation of South Africa.

My efforts regarding this study can be summed up by the following quote:

> "Everything is vague to a degree you do not realize till you have tried to make it precise."
> – Bertrand Russell

But I enjoyed all of it.

Contents

List of abbreviations

3D	:	Three dimensional	(p. 73)
AP	:	Action potential	(p. 35)
ARP	:	Absolute refractory period	(p. 18)
ANF	:	Auditory nerve fibre	(p. 1)
ECAP	:	Electrically evoked compound action potential	(p. 2)
FE	:	Firing efficiency	(p. 20)
GHK	:	Goldman-Hodgkin-Katz	(p. 6)
GSEF model	:	Generalised Schwarz-Eikhof-Frijns model	(p. 12)
HH model	:	Hodgkin-Huxley model	(p. 4)
IPG	:	Interphase gap	(p. 101)
IPI	:	Interpulse interval	(p. 20)
MCL	:	Most comfortable level	(p. 2)
MPI	:	Masker probe interval	(p. 19)
NRT	:	Neural Response Telemetry	(p. 2)
ODE	:	Ordinary differential equation	(p. 34)
RRP	:	Relative refractory period	(p. 18)
SEM	:	Scanning electron microscopy	(p. 14)
SFAP	:	Single-fibre action potential	(p. 17)
TEM	:	Transmission electron microscopy	(p. 14)

Chapter 1

INTRODUCTION

1.1 PROBLEM STATEMENT

1.1.1 Context of the problem

Cochlear implants have been developed to help rehabilitate profoundly deaf persons by providing them with a measure of sound perception through electrical stimulation of auditory nerve fibres (ANFs). The cochlear implant injects electric currents directly into the cochlea by means of an electrode array to stimulate the ANFs directly. The challenge facing researchers is how to convey meaningful speech information to the brain via electrical stimulation. Modern implants are multiple-electrode implants, typically utilizing 16 to 22 electrodes, to take advantage of the tonotopic organization of the ANFs (Loizou, 1998).

However, while the average performance of cochlear implants has improved over the last three decades, large variability in speech performance across individual implant users is still a major problem (Shannon, Fu, Galvin III and Friesen, 2004). This can in part be ascribed to dissimilar neural excitation spread patterns, both intrasubject and intersubject, as a result of variability in factors such as implant type, degree of degeneration of the auditory nerve fibre population across human subjects, electrode geometry, intrascalar electrode location and stimulation strategy (Nadol Jr, 1990; Schuknecht, 1993; Zimmermann, Burgess and Nadol Jr, 1995; Nadol Jr, 1997; Arts, Jones

and Anderson, 2003; Cohen, Richardson, Saunders and Cowan, 2003; Abbas, Hughes, Brown, Miller and South, 2004; Abbas and Miller, 2004; Van Wieringen, Carlyon, Laneau and Wouters, 2005; Fayad and Linthicum Jr, 2006). Even though potential implantees undergo pre-operative auditory testing, the successful outcome of the implantation is not known until after the implant has been switched on (Niparko, 2004). Ideally the electrodes should be situated closest to the sites of surviving ANFs, since this leads to reduced power consumption in the implant, lower stimulation thresholds, narrower neural excitation spread patterns and an increased dynamic range (Townshend and White, 1987; Shepherd, Hatshushika and Clark, 1993; Rebscher, Snyder and Leake, 2001; Abbas and Miller, 2004; Leake and Rebscher, 2004; Glueckert, Pfaller, Kinnefors, Rask-Andersen and Schrott-Fischer, 2005a). A telemetric measuring system for cochlear implants, called Neural Response Telemetry (NRT) by Cochlear Limited, is available to measure the electrically evoked compound action potential (ECAP) of the ANFs (see for example Abbas, Brown, Shallop, Firszt, Hughes, Hong and Staller, 1999; Dillier, Lai, Almqvist, Frohne, Müller-Deile, Stecker and van Wallenberg, 2002). ECAP data can be used to obtain an objective estimate of the dynamic range, and thus the extent of neural survival, through measurement of the behavioural threshold and most comfort level (MCL) of implantees (see for example Abbas *et al.*, 1999; Franck and Norton, 2001; Dillier *et al.*, 2002). It is also used to examine the extent to which psychophysical measurements reflect the amount of neural excitation spread (Cohen *et al.*, 2003).

The primary means of modelling the electrically stimulated human auditory system is using mammalian research animals, especially cats and guinea-pigs (see for example Javel, Tong, Shepherd and Clark, 1987; Abbas and Miller, 2004). Since these animals' cochleae have larger dimensions than those of smaller rodents, multi-electrode arrays similar to those implanted in humans, can be used. Computational models are used in combination with animal studies to enhance understanding of the underlying physiology of electric hearing (Abbas and Miller, 2004). Several ANF models have been developed (Bruce, White, Irlicht, O'Leary, Dynes, Javel and Clark, 1999c; Frijns, Briaire and Schoonhoven, 2000; Matsuoka, Rubinstein, Abbas and Miller, 2001; Rattay, Lutter and Felix, 2001b; Briaire and Frijns, 2005; Macherey, Carlyon, van Wieringen and Wouters, 2007). The ANF models are frequently used in combination with volume-conduction models of the cochlea to predict neural excitation profiles (Frijns *et al.*, 2000; Hanekom, 2001b; Rattay, Leao and Felix, 2001a). An advantage of the computer models is that it is possible to isolate and manipulate critical model para-

meters, as well as modelling of the differences in cochlear anatomy and ANF physiology between species, which is not always feasible with animal studies (Morse and Evans, 2003). Most of these models are at least partially based on animal data. However, the differences in cochlear structures between animals and humans, differences in the number and percentage myelination of auditory nerve fibres and innervation patterns of both inner and outer hair cells across species, may be physiologically significant and care must be taken when extrapolating the animal results to predict results in human implantees (Nadol Jr, 1988; Frijns, Briaire and Grote, 2001). Computer models can only approximate a real neural system, owing to the complexity of the latter. The modeller therefore has to make certain simplification assumptions when abstracting the real system and this place some limitations on the model as to the realistic correctness and completeness of the physiology and anatomy represented (Morse and Evans, 2003).

1.1.2 Research gap

Human ANF models have been developed by Briaire and Frijns (2005; 2006) and Rattay *et al.* (2001b). These models are partially based on human morphometric[1] data, while the ionic current dynamics are still those of rat and squid respectively. However, the Briaire and Frijns (2005) model cannot fully account for the ECAP morphology[2] observed in humans, while Macherey *et al.* (2007) argue that the ion channels of the squid based model, on which the Rattay *et al.* (2001b) model is based, are not sufficient to account for non-monotonic excitation behaviour experimentally observed. Hence, a more comprehensive computer model is needed, based on human cochlear dimensions and peripheral ANF characteristics, incorporating simulation of temporal characteristics.

Even though the physical structure of human ANFs has been investigated (refer to

[1] In Murray, Simpson and Weiner (1989) morphometry is defined as: "The process of measuring the shape and dimensions of landforms, living organisms, or other objects; (also) the shape and dimensions of an object so measured."

[2] Morphology is defined in Murray *et al.* (1989) as: "**1.** *Biol.* The branch of biology that deals with the form of living organisms and their parts, and the relationships between their structures. Formerly: *spec.* the comparison of the forms of organisms and their parts in order to identify homologous structures (cf. quots. 1853, 1859, 1872). **2.** orig. and chiefly *Science.* Shape, form, external structure or arrangement, esp. as an object of study or classification. Also: a particular shape, form, or external structure, esp. of (a part of) an organism, landform, etc."

Section 2.2), the properties and types of ionic membrane currents of spiral ganglion cells have been characterised in murine (Mo, Adamson and Davis, 2002; Reid, Flores-Otero and Davis, 2004; Hossain, Antic, Yang, Rasband and Morest, 2005; Chen and Davis, 2006) and guinea-pig (Bakondi, Pór, Kovács, Szucs and Rusznák, 2008), but not in human. Since the human ANF is of the peripheral sensory type, the possibility exists that similar ionic membrane currents to those found in a peripheral sensory fibre might be present. Ionic membrane current data from single human myelinated peripheral nerve fibres have been recorded by Reid, Bostock and Schwarz (1993), Scholz, Reid, Vogel and Bostock (1993), Schwarz, Reid and Bostock (1995) and Reid, Scholz, Bostock and Vogel (1999), but only the Schwarz *et al.* (1995) data have been used to develop a human nerve fibre model. However, to date none of these data have been applied to simulate human ANFs (Section 2.1.1). The development of a general human peripheral sensory nerve fibre can hence serve as an intermediate step to develop a human ANF model, until ionic membrane current data from human ANFs become available.

1.2 RESEARCH OBJECTIVE AND QUESTIONS

The objective of this study is to determine whether parameters of the nerve fibre model by Rattay *et al.* (2001b), which assumes a propagating action potential driven by Hodgkin-Huxley (HH) dynamics (Hodgkin and Huxley, 1952), can be modified with human morphometric and physiological data to predict excitability behaviour of human ANFs more accurately, including temporal characteristics. When coupled to the volume-conduction cochlear model by Hanekom (2001b) simulation of the ECAP method is effected to facilitate comparison between simulated and measured psychophysical forward masking experimental results. These expansions on current ANF modelling capabilities could lead to a better understanding of neural excitation behaviour as measured in psychoacoustic experiments.

The following research questions can be formulated from this objective:

1. The original HH model is developed for the giant unmyelinated nerve fibre of squid. Is it possible to replace the squid morphometric and physiological properties by human morphometric and physiological properties to improve predicted

human ANF responses? What properties should be changed?

2. Different cochlear implant designs are available and their placements inside the cochlea differ. Does the new ANF model provide additional or improved estimates of the effects of these differences on nerve fibre excitation behaviour to those provided by existing ANF models?

3. Current nerve fibre models do not explicitly take temporal characteristics of the input signal into account. Will the adapted nerve fibre model be able to isolate the effects that these temporal characteristics have on measured data? How well will the model predict variations in temporal characteristics compared to the current models?

4. One way of comparing predicted results with measured psychophysical forward masking experimental results gained from human implantees is modelling the ECAP method used in NRT. A comprehensive model to predict ECAP data has been developed by Briaire and Frijns (2005). However, their results indicate that their nerve fibre model can not fully predict measured ECAP data. If the adapted nerve fibre model developed in this study is used in conjunction with their ECAP method, how well will the modelled ECAP results compare with results from literature? How well do these results predict nerve fibre excitation behaviour?

1.3 HYPOTHESIS AND APPROACH

The hypothesis is that a more accurate model of the electrically stimulated human Type I ANF will be able to predict excitation behaviour measurements better, for example ECAP profile widths and stimulus temporal characteristics (mean latency, threshold, threshold-distance and strength-duration relationships), compared to those predicted by current ANF models. Simulated results will be verified against experimental results from humans only. A bottom-up approach is followed, starting with the current Hodgkin-Huxley and Rattay *et al.* (2001b) models and ending with the revised ANF model. The revision is implemented in phases.

The solution to the main research questions can be broken down into five goals:

1. Expansion of the existing ANF model by Rattay *et al.* (2001b) to represent a more accurate model of the human ANF with regard to physiology and morphometry, both for damaged (degenerate) and non-damaged (non-degenerate) nerve fibres. Model development is broken down into three phases. Firstly, the HH model has to be modified to describe action potential dynamics at Ranvier nodes using recorded ionic membrane current data from single human myelinated peripheral nerve fibres (Reid *et al.*, 1993; Scholz *et al.*, 1993; Schwarz *et al.*, 1995; Reid *et al.*, 1999). Secondly, a general human peripheral sensory nerve fibre cable model, based on a combination of the models by Rattay *et al.* (2001b) and Blight (1985), has to be constructed using human sensory nerve fibre morphometric data. Thirdly, a Type I human ANF model, based on the model by Rattay *et al.* (2001b), but with the axon replaced with the generalised human sensory nerve fibre model, has to be developed.

2. Development of a simple method to simulate the ECAP method and to estimate stimulus attenuation values by calculating the values that best fit the modelled excitation profile widths to the measured ECAP profile widths.

3. Comparison of predicted simulated ECAP profile widths with NRT results documented in literature to gain a better understanding of the effect neural excitation has on speech perception. Firstly the simulated data have to be compared with existing results (see for example Cohen *et al.*, 2003; Polak, Hodges, King and Balkany, 2004) to verify model outcomes. Then, using the same parameters used during the psycho-physical experiments, the simulated ECAP profile width results have to be compared with experimental results.

4. Evaluation of the temporal characteristics of the model. The model should be able to predict single-pulse and pulse-train responses as documented in literature.

5. Prediction of neural excitation threshold and excitation patterns (compare with Van Wieringen *et al.*, 2005; Macherey *et al.*, 2007) for different stimulation parameters (including pulse width, intensity, pulse rate, pulse shape, and stimulation mode).

1.4 RESEARCH CONTRIBUTION

The research contributions made by this study include the following:

1. The modification of the original HH model to predict the excitation behaviour of a generalised human peripheral sensory nerve fibre. This study was the first to show that the HH model equations could be modified successfully without using the Goldman-Hodgkin-Katz (GHK) equations. As far as is known, the proposed model is the most comprehensive available at present.

2. A more comprehensive establishment of temperature dependence of the model's physiological and electrical parameters compared to other existing models.

3. The development of a more realistic model of the human Type I ANF to predict excitation behaviour of the electrically stimulated human auditory system.

4. From the comparison between predicted and experimentally measured results of Type I ANF fibres, the existence of similar transient and persistent sodium as well as slow potassium ionic membrane currents to those present in general sensory nerve fibres can be deduced.

5. Confirmation that chronaxie, rheobase current, mean latency, threshold and relative refractory periods are dependent on the amount of degeneracy of the ANF.

6. Confirmation that electrode arrays located closer to the modiolus produce more focused neural excitation spread than more laterally located electrode arrays.

7. Evidence that the ANF model can account for threshold differences observed between different asymmetric waveforms.

8. Evidence that the combination of persistent sodium and slow potassium ionic membrane currents can in part predict non-monotonic excitation behaviour.

9. The simplified method to solve the inverse problem, i.e. to calculate the ECAP response as a result of neural excitation, contributes to the modelling approach to cochlear implant research in the following ways:

   (a) it provides a means to compare NRT experimental data with the results obtained from any model that predicts neural excitation profiles on the

neural level (including the detailed finite element volume-conduction neural model used in this study and purely analytical volume-conduction models where potential distribution is calculated in a homogeneous medium (Jolly, Spelman and Clopton, 1996; Hanekom, 2001a) coupled to a nerve fibre model) for verification of such models,

(b) it provides a computationally effective way to obtain an estimate of ECAP profile widths from the output of models that calculate the excitation profiles at the neural level, and

(c) it provides an indirect way to estimate stimulus attenuation by calculating the value of the parameter that produces the best fit to experimental data.

1.5 OVERVIEW OF THE STUDY

The development of a comprehensive model of the implanted human cochlea can be broken down into two parts, namely a volume-conduction model of the implanted cochlea and a model of the electrically stimulated ANF (Figure 1.1). As stated previously, the development of the human ANF model is covered in this study, as indicated by the black square blocks in the diagram in Figure 1.1. The ANF consists of dendritic, somal and axonal sections, as indicated by the dot-dashed block. The methods used to compare and verify simulated results against experimental data such as psychoacoustic phenomena and ECAP widths are grouped together in the grey dashed block in the figure.

Related issues not covered by the study include:

1. Modelling of ephaptic excitation between groups of nerve fibres (Jönsson, Hanekom and Hanekom, 2008).
2. An extension of the double cable model as suggested by Nygren and Halter (1999) to aid in the modelling of demyelisation of the long-term degenerate ANF (Schuknecht, 1993).
3. Modelling of stochastic nerve fibre membrane properties. ANF stochastic models have been described by Rubinstein (1995), Matsuoka *et al.* (2001) and Bruce (2007).

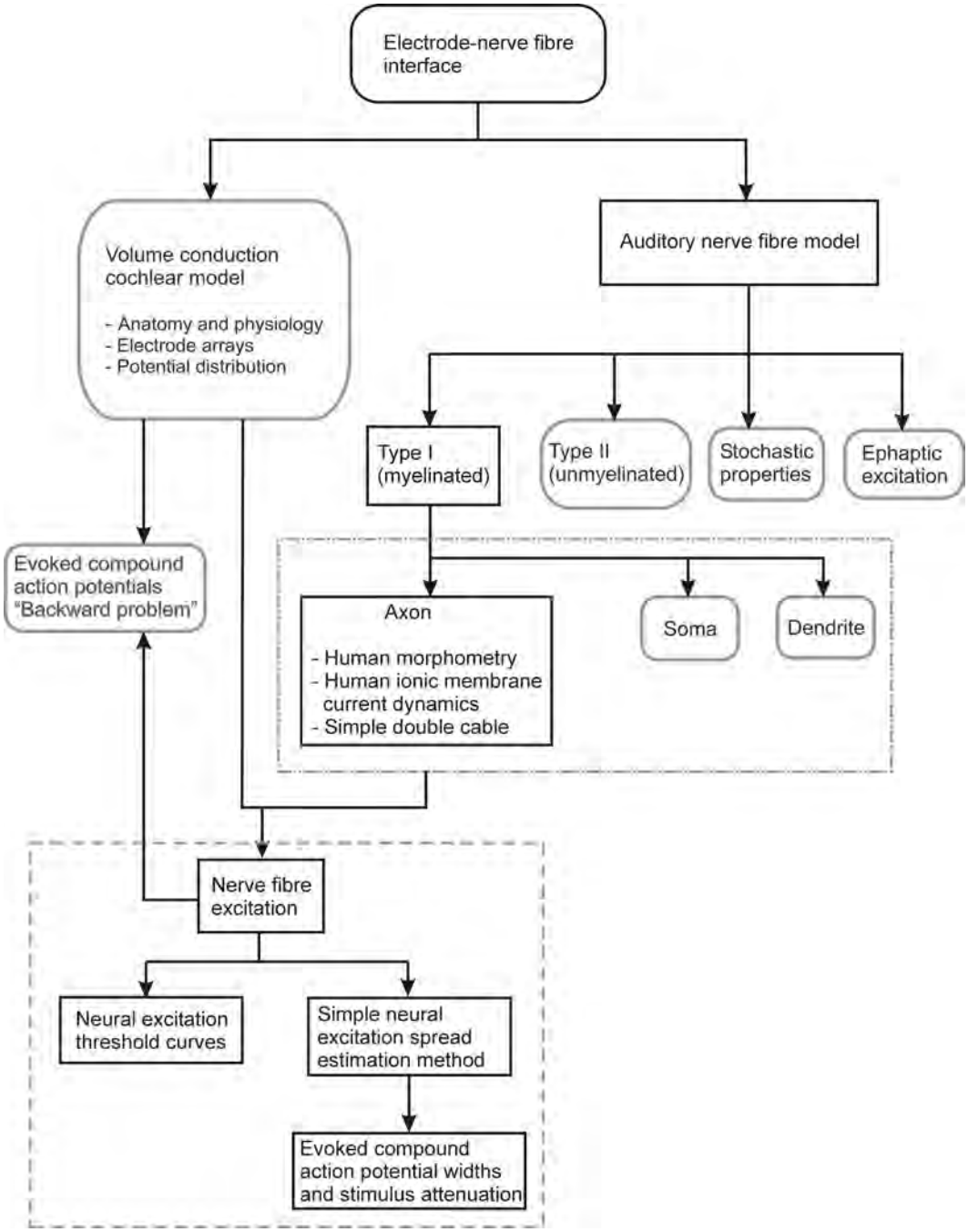

Figure 1.1: Diagram of the electrode-nerve fibre interface. Issues covered by this study are indicated by the black square blocks, while the grey rounded blocks represent related issues. Nerve fibre sections are included in the dot-dashed block. Simulation methods used to verify the model results are grouped together in the grey dashed block.

4. An expansion of the volume-conduction model to make provision for simulation of the full 2.75 turns, the tapering of the cochlear ducts and capacitances of the cochlear structures.

The thesis is divided into the following chapters:

In Chapter 2 the background argument necessary to understand the research problem is presented.

In Chapter 3 the development of the human Ranvier node model based on the modification of the HH model is described.

In Chapter 4 the Ranvier node model is incorporated into a generalised human peripheral sensory nerve fibre model.

In Chapter 5 the Type I ANF model of Rattay *et al.* (2001b) is modified by replacing the axon with the generalised sensory nerve fibre model.

In Chapter 6 the development of a simple method to simulate ECAPs and subsequent calculation of neural excitation widths are discussed.

In Chapter 7 the influence of the temporal characteristics of different waveforms on simulated behavioural threshold is investigated and compared to measured data.

In Chapter 8 the thesis is concluded with a general discussion and conclusion of the study, as well as the provision of directives for future research.

Chapter 2

BACKGROUND REVIEW

Modern medicine increasingly uses electrical stimulation of nerve tissue to help patients regain lost functionality (Rattay, Resatz, Lutter, Minassian, Jilge and Dimitrijevic, 2003). Computational models aid in enhancing understanding of the behaviour of the electrically stimulated nerve fibre. In the cochlear implant research field much research is being done to unravel the secrets of the way the auditory system of a person with profound hearing loss translates an input sound signal presented through electrical stimuli into a perceptible sound (see for example Cohen *et al.*, 2003; Macherey, van Wieringen, Carlyon, Deeks and Wouters, 2006). Especially, a better understanding of the way the implanted auditory system decodes the temporal information carried in speech needs to be gained before improved implants can be developed.

Computational models of the ANF can be divided into physiologically based (Colombo and Parkins, 1987; Frijns, Mooij and ten Kate, 1994; Rubinstein, 1995; Matsuoka *et al.*, 2001; Rattay *et al.*, 2001b; Rubinstein, Miller, Mino and Abbas, 2001; Morse and Evans, 2003; Briaire and Frijns, 2005) and phenomenological ANF models (Shannon, 1989; Bruce, White, Irlicht, O'Leary and Clark, 1999b; Miller, Abbas and Rubinstein, 1999a; Zhang, Heinz, Bruce and Carney, 2001; Carlyon, van Wieringen, Deeks, Long, Lyzenga and Wouters, 2005; Macherey *et al.*, 2007). These models can be further subdivided into deterministic (for example Frijns *et al.*, 1994; Rattay *et al.*, 2001b; Briaire and Frijns, 2005) and stochastic models (for example Bruce *et al.*, 1999b; Rubinstein *et al.*, 2001; Macherey *et al.*, 2007).

The present study focuses on the development of a physiological, deterministic model based on the Rattay *et al.* (2001b) cable model, but with human morphometric and physiological data replacing the corresponding squid data. In this chapter a background argument is presented, which is necessary for developing such a model. Physiologically based deterministic models of both animal and human are presented, together with the temperature dependence of parameters. This is followed by an overview of the morphometric and physiological properties of the human peripheral Type I ANF.

The developed model will be verified against experimentally measured temporal characteristic data. Most of the earlier measurement studies centred on observations from single fibres in cats and guinea-pigs, while more recent studies increasingly made use of gross ensemble observations through ECAP measurements. The measurement of ECAPs can be used to examine the extent to which psychophysical measurements reflect the amount of neural excitation spread (Cohen *et al.*, 2003; Miller, Abbas, Nourski, Hu and Robinson, 2003). The development of a comprehensive model to simulate ECAPs falls outside the scope of this study. However, ECAP profile widths can be used to estimate stimulus attenuation and hence the extent of neural excitation spread inside the cochlea. Lastly an overview of the main temporal characteristics touched upon in this study is provided. Additional background information relevant to specific topics is provided in Chapters 3 to 7 when the respective topics are discussed.

2.1 PHYSIOLOGICALLY BASED MODELS

2.1.1 Animal-based models

Originally physiologically based models have been based on *in vitro* recorded experimental data from squid (Hodgkin and Huxley, 1952), toad (Frankenhaeuser and Huxley, 1964), rabbit (Chiu, Ritchie, Rogart and Stagg, 1979) and rat (Schwarz and Eikhof, 1987). These models consist of a cable model describing the way in which the action potential propagates along the nerve fibre. Fitting into this cable model is a membrane model, which describes the local action potential at the active nerve fibre sections (usually the nodes of Ranvier in myelinated nerve fibres). The main problem therefore is to decide upon the most applicable model.

Rubinstein (1993) developed a passive membrane cable model of a myelinated single ANF. Mammalian peripheral nerve fibre electrical parameter values and anatomical parameter values from cat Type I spiral ganglion ANFs at 37 °C were used in the model. Ranvier node kinetics were changed to a modified Frankenhaeuser-Huxley (1964) modelled fibre (Rubinstein, 1995). The axonal model consists of a deterministic representation of the internodes, a stochastic representation of the Ranvier nodes and no cell body representation (Rubinstein, Wilson, Finley and Abbas, 1999). Biophysical model parameters of the sodium channels, membrane capacitance and leakage current are chosen to best fit recorded single nerve fibre temporal properties in acutely deafened cats, while other anatomical parameters are the same as in the original passive membrane cable model.

Frijns and ten Kate (1994), Frijns, de Snoo and Schoonhoven (1995) and Frijns *et al.* (2000) developed a model based on the Schwarz-Eikhof nerve fibre model for rat (Schwarz and Eikhof, 1987), but modified with guinea-pig morphometry. Recently this Generalised Schwarz-Eikhof-Frijns (GSEF) model was modified for human ANF simulations by employing human morphometric data only (Briaire and Frijns, 2005; Briaire and Frijns, 2006). The ionic current dynamics of this model, however, are still those of rat. Even though similarities exist between the properties of ionic currents at the rat and human Ranvier node (Safronov, Kampe and Vogel, 1993; Röper and Schwarz, 1989), differences such as those in the activation and deactivation characteristics of voltage-gated potassium ion (K^+) channels can result in differences in nerve fibre conduction behaviour predictions (Reid *et al.*, 1999).

Moore, Joyner, Brill, Waxman and Najar-Joa (1978) simulated impulse conduction in myelinated nerve fibres, using the HH model, but with a tenfold increase in the ion channel density at the Ranvier nodes. Although the original HH model fails to conduct at temperatures higher than 30 °C, their high-density model can conduct impulses even at temperatures higher than 40 °C. A study comparing the applicability of the aforementioned animal models to predict human auditory nerve fibre excitation favours the HH model, provided the nodal ion channel kinetics are accelerated tenfold (Rattay, 1990; Rattay and Aberham, 1993). Replacement of the squid morphometric properties by human morphometric properties further improve predicted human auditory nerve fibre responses (Rattay *et al.*, 2001b). This modified HH model shows improved human auditory nerve fibre response predictions, as well as an improved prediction of chronaxie time of 340 μs versus 15 – 45 μs of the GSEF model (Frijns *et al.*, 1994), by

changing the cable morphometric properties to those of human (Rattay *et al.*, 2001b). Huxley (1959) also suggested that by accelerating the activation and inactivation of membrane sodium ion permeability of the HH model fourfold, firing behaviour at a myelinated amphibian Ranvier node can be represented.

Matsuoka, Abbas, Rubinstein and Miller (2000b) and Morse and Evans (2003) discussed the differences and similarities between animal and human data. In most animal studies, animals deafened acutely within a week before experiments are used. However, degeneration of the ANF morphology due to ototoxic effects can take several weeks and therefore a larger relatively intact neural population is expected, in contrast to the more degenerative neural population of the longer-term deafened animal or human (Morse and Evans, 2003). Acutely deafened animal models can thus only give a best case scenario for the electrical excitation of the human ANF (Abbas and Miller, 2004). In many of the animal experiments, a single electrode is placed inside the cochlea (Van den Honert and Stypulkowski, 1984), while in humans multiple-electrode arrays are used. The anatomy of the animal and human nerve fibres also differs (Rattay *et al.*, 2001b; Briaire and Frijns, 2005). Thus, nerve fibre models based on animal physiology at this stage can only roughly approximate human ANF behaviour.

2.1.2 Human-based models

Even though ionic membrane current data from single human myelinated peripheral nerve fibres have been recorded by Reid *et al.* (1993; 1999) and Scholz *et al.* (1993), no computational models have been developed employing these data. Schwarz *et al.* (1995) experimentally measured and computationally modelled the action potential and membrane currents at the human Ranvier node and compared the modelled results to a measured human Ranvier node action potential. Bostock and Rothwell (1997) used this model to explain differences in recorded latent addition results between motor and sensory human peripheral nerve fibres. Also, Wesselink, Holsheimer and Boom (1999) developed a fibre cable model partially based on the data and Ranvier node model by Schwarz *et al.* (1995) to predict human myelinated sensory nerve fibre responses to electrical stimulation of the spinal cord. However, to date none of these models has been applied to simulate human ANFs.

2.1.3 Temperature dependence of nerve fibre excitation behaviour

Nerve fibre excitation behaviour is affected by temperature changes (Burke, Mogyoros, Vagg and Kiernan, 1999; Moore *et al.*, 1978). Studies on human peripheral nerve fibres indicate an increase in action potential (AP) amplitude and duration, the absolute and relative refractory periods and chronaxie times when the temperature is decreased from 37 °C; while the rheobase current and conduction velocity decrease under the same temperature conditions (Kiernan, Cikurel and Bostock, 2001; Lowitzsch, Hopf and Galland, 1977; Buchthal and Rosenfalck, 1966). Temperature dependence of the sodium channel kinetics is included in computational models describing excitation behaviour in human nerve fibres; for example the models of Schwarz *et al.* (1995) and Wesselink *et al.* (1999), but not for the potassium channel and leakage kinetics, as well as other electrical parameters used. Similar to the HH model, temperature dependence of rate constants is effected using Q_{10} factors.

Temperature dependence of some of the parameters in ANF models has also been included. In the version of the HH model used by Rattay and co-workers, only the temperature dependence of the rate constants is considered (Rattay, 1990; Rattay and Aberham, 1993; Rattay *et al.*, 2001b). In the GSEF model the temperature dependence of the sodium and potassium membrane currents, rate constants, axoplasmic resistivity and external medium resistivity are included (Frijns *et al.*, 1994; Frijns *et al.*, 1995; Briaire and Frijns, 2005).

2.2 PERIPHERAL AUDITORY NERVE FIBRE

2.2.1 General overview and degeneration

The peripheral auditory pathway begins in the inner ear (or cochlea), where the ANFs innervate hair cells in the Organ of Corti which is housed inside the cochlea. From there the ANF bundle runs in a spiralled fashion inside a spongy bony canal, referred to as the modiolus, to the more central parts of the auditory system (Schuknecht, 1993). Detailed descriptions, together with transmission (TEM) and scanning (SEM) electron

microscopic studies of the auditory structures of the cochlea, are provided by Schuknecht (1993), Glueckert *et al.* (2005a), Glueckert, Pfaller, Kinnefors, Rask-Andersen and Schrott-Fischer (2005b) and Glueckert, Pfaller, Kinnefors, Schrott-Fischer and Rask-Andersen (2005c).

In normal hearing adult persons, the hair cells in the Organ of Corti are innervated by approximately 32,000 to 41,000 afferent myelinated ANFs (Schuknecht, 1993; Felder, Kanonier, Scholtz, Rask-Andersen and Schrott-Fischer, 1997; Nadol Jr, 1997). Innervation density varies from the cochlear base to the apex (Glueckert *et al.*, 2005a), with roughly 300 – 400 fibres per millimetre in the base and apex and about 1,400 fibres per millimetre in the lower second turn in a normal hearing person (Spoendlin and Schrott, 1989; Zimmermann *et al.*, 1995; Nadol Jr, 1997).

In mammals two distinct types of ANFs exist. The Type I ANF constitutes about 90% to 95% of the population, is bipolar, has a myelinated axon, thinly myelinated to unmyelinated somal perikaryon, and exclusively innervates the inner hair cells (Nadol Jr, 1988; Spoendlin and Schrott, 1989; Schuknecht, 1993; Rask-Andersen, Tylstedt, Kinnefors and Schrott-Fischer, 1997; Glueckert *et al.*, 2005a; Pamulova, Linder and Rask-Andersen, 2006). The Type II ANF has a smaller fibre diameter, is unmyelinated, pseudomonopolar, innervates the outer hair cells and constitutes about 5% to 10% of the population (Spoendlin and Schrott, 1989; Schuknecht, 1993; Glueckert *et al.*, 2005b; Pamulova *et al.*, 2006).

The degeneration and subsequent loss of ANFs resulting in hearing loss can be classified as primary or secondary. Primary neural degeneration is the normal age-related hearing loss a person experiences, while secondary (retrograde) neural degeneration is due to various factors including ototoxic substances, disease or trauma to the cochlear structures (Nadol Jr, 1990; Schuknecht, 1993). Retrograde neural degeneration, in which the dendrites retract but the somas and axons survive, occurs in persons with profound sensory hearing loss (Spoendlin and Schrott, 1989; Nadol Jr, 1990; Schuknecht, 1993). The surviving degenerate somas and axons are significantly smaller than in non-degenerate ANFs (Nadol Jr, 1990; Zimmermann *et al.*, 1995; Glueckert *et al.*, 2005a). The degree of retrograde neural degeneration depends on the severity of tissue alterations in the Organ of Corti during the original insult, as well as surgical trauma to cochlear structures due to electrode insertion, and concerns mostly Type I ANFs (Schuknecht, 1993; Fayad and Linthicum Jr, 2006). Even though retrograde

degeneration occurs at a slow pace, persons with long-term hearing loss have fewer surviving Type I ANFs than persons with shorter-term hearing loss (Linthicum Jr and Anderson, 1991; Nadol Jr and Xu, 1992; Schuknecht, 1993; Zimmermann *et al.*, 1995; Felder *et al.*, 1997; Fayad and Linthicum Jr, 2006). Type II ANFs are more resistant to retrograde degeneration and their relative percentage compared to Type I ANFs increases (Spoendlin and Schrott, 1989).

2.2.2 Type I auditory nerve fibre properties

In addition to the above-mentioned properties, the large Type I ANF can be subdivided into two subtypes based on morphological, morphometrical (somal, nuclear, dendritic and axonal diameters) and physiological data (Nadol Jr, Burgess and Reisser, 1990; Rosbe, Burgess, Glynn and Nadol Jr, 1996).

Dendritic lengths vary between 1.4 mm in the lower basal turn, 1.1 mm in the second turn and 0.8 – 1.0 mm in the apex (Spoendlin and Schrott, 1989; Glueckert *et al.*, 2005a; Glueckert *et al.*, 2005b). They are thinly myelinated having about 23 myelin layers, i.e. about 0.25 μm thick (Spoendlin and Schrott, 1989), with diameters between 1.2 and 1.4 μm (Nadol Jr *et al.*, 1990).

In general somal diameters vary between 24.6 and 32.4 μm (Spoendlin and Schrott, 1989; Nadol Jr *et al.*, 1990; Schuknecht, 1993; Rosbe *et al.*, 1996; Glueckert *et al.*, 2005a). Somal nucleae are almost spherical (Spoendlin and Schrott, 1989; Rosbe *et al.*, 1996), with diameters varying between 11.0 and 14.5 μm (Spoendlin and Schrott, 1989; Nadol Jr *et al.*, 1990; Rosbe *et al.*, 1996). Type I cells tend to cluster together in groups where they frequently share the same Schwann cell sheaths (Rask-Andersen *et al.*, 1997; Tylstedt and Rask-Andersen, 2001; Glueckert *et al.*, 2005a). Unmyelinated nerve fibres, possibly the dendrites of other Type I ANFs or nerve fibres belonging to the intra-ganglionic spiral bundle, form close associations with these cells (Rask-Andersen *et al.*, 1997; Tylstedt and Rask-Andersen, 2001; Glueckert *et al.*, 2005a). It is suggested that these neuronal interactions and cell clustering provide a trophic supply to the remaining cells and may in part explain the slow rate of the retrograde degenerative process and hence the longer survival of the somas and axons of ANFs compared to dendrites (Felder *et al.*, 1997; Tylstedt and Rask-Andersen, 2001; Glueckert *et al.*, 2005a; Pamulova *et al.*, 2006).

SEM photographs and measured data indicate that the largest fibre diameter in the basal turn is 4.3 μm and the smallest in the upper middle turn 3.2 μm, the average fibre diameter being about 3.75 μm (Rosbe *et al.*, 1996; Glueckert *et al.*, 2005a). Axonal diameters vary between 2.34 and 3.7 μm (Rosbe *et al.*, 1996; Glueckert *et al.*, 2005a). The number of myelin layers around the axons varies between 60 and 83, i.e. a myelin thickness between 0.7 and 1.0 μm and total axonal lengths vary between 30 and 40 mm (Spoendlin and Schrott, 1989).

2.3 SINGLE-FIBRE VERSUS GROSS ENSEMBLE AUDITORY NERVE FIBRE STUDIES

While computational models are used to explore separate physiological mechanisms of the ANFs and how these mechanisms influence temporal characteristic predictions, results from animal studies are used for validation. These animal studies are broadly divided into single-fibre and gross ensemble fibre studies (Abbas and Miller, 2004).

Most of the early work performed in determining the temporal characteristics of electrical stimulation were performed on single-fibre preparations of cats and guinea-pigs (Moxon, 1971; Kiang and Moxon, 1972; Hartmann, Topp and Klinke, 1982; Van den Honert and Stypulkowski, 1984; Javel *et al.*, 1987; Van den Honert and Stypulkowski, 1987a; Van den Honert and Stypulkowski, 1987b; Hartmann and Klinke, 1990; Javel, 1990; Dynes and Delgutte, 1992; Klinke and Hartmann, 1997; Shepherd and Javel, 1997; Shepherd and Javel, 1999; Javel and Shepherd, 2000). Although the results of these single-fibre studies aid in understanding and characterising single-fibre responses to electrical stimuli, gross ensemble potential studies are instead performed on humans where recent studies rely on the measurement of the electrically evoked compound action potential (ECAP) (Shannon, 1985; Brown, Abbas and Gantz, 1990; Abbas *et al.*, 1999; Miller, Abbas and Brown, 2000; Tykocinski, Cohen, Pyman, Roland, Treaba, Palamara, Dahm, Shepherd, Xu, Cowan, Cohen and Clark, 2000; Dillier *et al.*, 2002; Saunders, Cohen, Aschendorff, Shapiro, Knight, Stecker, Richter, Waltzman, Tykocinski, Roland, Laszig and Cowan, 2002; Cohen *et al.*, 2003; Abbas *et al.*, 2004; Cohen, Saunders and Richardson, 2004; Etler, Abbas, Hughes, Brown, Dunn, Zubrod and van Voorst, 2004; Cohen, Saunders, Knight and Cowan, 2006; Lai and Dillier, 2008). The ECAP requires the synchronous firing of the

ANFs to elicit a measurable potential, since it is in essence the summation of all the action potentials produced by the nerve fibre population (Abbas and Miller, 2004).

Miller *et al.* (1999a) used a phenomenological approach to develop an empirical model simulating ECAP responses, with the ECAP response assumed to be the summation of all the single-fibre responses. The model is based on their single-fibre cat data for cathodic responses from the Miller, Abbas, Robinson, Rubinstein and Matsuoka (1999b) study. Simulation results suggest that the ECAP amplitude is proportional to the number of actively responding nerve fibres. ECAP studies assume that the neural response to each individual stimulus is identical. Such assumptions depend on the level and rate of stimulus presentation, but can potentially be affected by the properties of the stimulated nerve fibres and their neuropathological state (Abbas and Miller, 2004).

Briaire and Frijns (2005) developed a model to calculate the ECAP response as measured via the NRT system. ECAP responses were simulated by solving what they termed the full "backward problem", i.e. calculating the ECAP responses at the electrode array level in the volume conduction cochlear part of the model from the single-fibre action potentials (SFAPs) calculated with the nerve fibre model discussed in Section 2.1.1. The superposition of these SFAPs then gives the ECAP response. The model is used to investigate the validity of the assumptions that the ECAP amplitude is proportional to the number of actively responding nerve fibres and that the neural response to each individual stimulus is identical, i.e. every nerve fibre contributes equally to the ECAP response. Results indicate that the nerve fibres from the centre of the excitation area make a different contribution to those around the edges. Electrodes placed closer to the outer wall are predicted to cause excitation in the peripheral part of the neurons, in contrast to electrodes placed closer to the modiolus. Their results also show that as the number of excited neurons increases, the ECAP response amplitude first increases up to a certain stimulus intensity, after which it decreases. However, the model cannot fully account for the ECAP morphology observed in humans and rather resembles the ECAP and AP shapes of the rat model by Schwarz and Eikhof (1987) on which the nodal kinetics of the GSEF model are based. They hence suggested the implementation of the human nodal kinetics model by Wesselink *et al.* (1999).

2.4 GROSS ENSEMBLE STUDIES: PREDICTING NEURAL EXCITATION SPREAD INSIDE THE COCHLEA

ECAP data are obtained by a forward masking paradigm and it is generally assumed that psychophysical forward masking profiles provide an indirect measure of neural excitation patterns (van der Heijden and Kohlrausch, 1994; Chatterjee and Shannon, 1998; Abbas *et al.*, 2004). In the case of ECAP data, the measure is more direct than in the case of psychophysical forward masking, since it is assumed that the central auditory processes do not contribute to the masking profile. Furthermore, the amplitude measurement of the ECAP gives an indication of the number of responding fibres (Miller *et al.*, 1999a). Cohen *et al.* (2003) reported that larger ECAP profile widths are measured for stimulation at higher most comfortable levels (MCLs) rather than for lower MCLs, indicating a wider spread of neural excitation in the former. The spread in excitation also increases with an increase in stimulus level (Abbas *et al.*, 2004). Miller *et al.* (2003) used the fact that the ECAP reflects the gross ensemble response of a neural population to investigate the effects of stimulation mode on neural excitation spread. The results indicate that monopolar stimulation produces wider ECAP profiles than bipolar stimulation, consistent with the observation that monopolar stimulation causes wider neural excitation (Van den Honert and Stypulkowski, 1987a). Townshend and White (1987) developed a paradigm based on the psychophysical thresholds measured for two human implantees to calculate the current spread patterns around the electrodes of a modelled electrode array. Their simulations confirmed wider neural excitation spread with monopolar compared to bipolar stimulation, as well as a reduction in excitation spread for an electrode array placed closer to the modiolus.

Stimulus attenuation directly relates to current distribution and thus the extent of neural excitation inside the cochlea. There have been only a few studies to determine the stimulus attenuation inside the cochlea. Black and Clark (1980) and Black, Clark, Tong and Patrick (1983) measured length constants of 8.0 – 16.0 mm (0.54 – 1.09 dB/mm) for monopolar stimulation in living cats. This compared well with the length constants of 4.0 – 13.0 mm (0.67 – 2.12 dB/mm) predicted with their lumped parameter model. Tank measurements by Kral, Hartmann, Mortazavi and Klinke

(1998) compared well with cadaver measurements from the basal part of cat cochleae. They found a length constant of 1.43 mm (6.07 dB/mm) for monopolar stimulation, which is a much larger attenuation value than those found in other studies.

2.5 TEMPORAL CHARACTERISTICS

Excitation behaviour in ANFs is described in terms of the temporal characteristics of pulses, whether these be single pulses or pulse trains. The most familiar of these are:

1. discharge rate
2. adaptation
3. alternation
4. absolute (ARP) and relative (RRP) refractory periods of the action potential
5. entrainment, also referred to as time-locking
6. phase-locking
7. synchronisation
8. mean latency and jitter
9. threshold
10. the threshold-distance relationship
11. strength-duration relationship

In the following subsections the main findings regarding the temporal characteristics investigated in this study are presented. These are refractory periods, mean latency, thresholds, threshold-distance relationships and strength-duration relationships. The review is, however, not exhaustive. The temporal characteristics not covered here are reviewed in Addendum A.

2.5.1 Absolute and relative refractory periods of the action potential

Stimulation in cochlear implants is typically in the form of pulse trains and, in the case of earlier implants, continuous stimulation. The refractory properties of the neural membrane play an important role in the choice of stimulation used and can limit ANFs' ability to encode the temporal characteristics of input stimuli (Miller, Abbas and Robinson, 2001a; Abbas and Miller, 2004) by

- placing a lower limit on the interphase / interpulse interval, hence raising the threshold stimulus intensity needed to elicit further responses during the RRP (see Section 2.5.3). Note that during the ARP, the fibre can elicit no further responses, even if the stimulus intensity is increased.
- placing an upper limit on the stimulus rate used. Most of the temporal phenomena discussed in the sections on entrainment, alternation, mean latency and jitter and discharge rate can possibly be attributed to the effects of neural refractoriness.

In studies on nerve fibre refractoriness, a two-pulse masker-probe paradigm is used (see for example Cartee, van den Honert, Finley and Miller, 2000; Miller *et al.*, 2001a). The masker probe interval (MPI) is varied and the amount of reduced excitability noted. In studies performed on cats, Hartmann, Topp and Klinke (1984) observed a reduction in fibre excitability for MPIs shorter than 5.0 ms. Bruce, Irlicht, White, O'Leary, Dynes, Javel and Clark (1999a) developed a phenomenological model of the ANF and estimated an ARP of 0.7 ms and a recovery time constant of 1.3 ms for pulse train stimulation. More recently, refractory observations in cat studies by Cartee *et al.* (2000) (monopolar, cathodic pseudomonophasic pulses) and Miller *et al.* (2001a) (monopolar, cathodic monophasic pulses) using a forward-masking paradigm, have shown a decrease in threshold intensity needed for the probe pulse as the interpulse interval (IPI) was increased. Cartee *et al.* (2000) suggested a mean ARP of 0.7 ms, while RRP values can be up to 5.0 ms (Cartee *et al.*, 2000; Abbas and Miller, 2004). ECAP responses measured in cats also suggest an ARP between 0.3 ms (Miller *et al.*, 2000) and 0.5 ms (Brown and Abbas, 1990). A mean ARP of about 330 μs and a mean recovery time constant of about 410 μs are estimated for cat auditory fibres by

Miller *et al.* (2001a). ECAP studies on humans suggest an ARP value larger than 0.5 ms and an RRP value around 5.0 ms (Brown *et al.*, 1990).

2.5.2 Mean latency and jitter

Spike latency is defined as the time latency between stimulus onset and maximum AP amplitude, while mean latency is the arithmetic mean of all the spike latencies measured for a specific stimulus intensity (Van den Honert and Stypulkowski, 1984; Rubinstein, 1995; Miller *et al.*, 1999b). Latency jitter, also just known as jitter, is defined as the standard deviation from the mean latency (Van den Honert and Stypulkowski, 1984; Rubinstein, 1995; Miller *et al.*, 1999b). Closely related is the concept of firing efficiency (FE), defined as the ratio of the number of observed spikes to the number of presented stimuli (Van den Honert and Stypulkowski, 1984; Rubinstein, 1995). Experimentally FE is computed as the percentage of stimuli that elicits an AP (Miller *et al.*, 2001a), and increases with an increase in stimulus intensity.

In single-fibre studies preformed on normal hearing cats, the mean latency shows a decrease with an increase in stimulus intensity, and hence with an increase in FE, reaching an asymptotic level at high stimulus intensities, while for laminectomated animals, in which the dendrites and somas are removed but the axons left intact, the mean latencies are much shorter and approximate the latency behaviour of normal fibres excited at high stimulus intensities (Van den Honert and Stypulkowski, 1984). Javel *et al.* (1987) used bipolar, biphasic stimuli on acutely deafened cats implanted with a multi-electrode array. They confirmed the findings of van den Honert and Stypulkowski by observing highly synchronised, short-latency responses with increased stimulus intensity. Responses have double peaks with latencies $\sim$ 0.3 and 0.6 ms and are considered to be a result of direct depolarisation of the neural membrane. These short latency responses are also maintained at higher discharge rates than is possible with acoustic stimulation.

Van den Honert and Stypulkowski's (1984) results indicate a decrease in jitter with increasing stimulus levels and hence FE, as well as a difference in jitter between normal and damaged fibres. Both the normal and damaged fibres show short latency jitter responses, while for longer latencies the high jitter responses are missing in the damaged fibres. Jitter in the damaged fibres is also greatly reduced. This is consistent

with the results of Kiang and Moxon (1972), showing shorter latencies and reduced jitter responses to electrical stimulation compared to normal neuronal responses, which reflect the characteristics of resonant systems.

At high stimulus intensities similarities in latency and jitter measurements are observed between normal and damaged fibres (Van den Honert and Stypulkowski, 1984). These authors suggest that the site of fibre excitation shifts more centrally towards the modiolus as the stimulus intensity is increased, since excitation in damaged fibres occurs in the axonal part of the fibre. In the double-peak response observed by Javel *et al.* (1987) the longer latency response is replaced by the shorter latency response as the stimulus intensity is increased. The authors argued that the former reflects peripheral dendritic excitation and that the shift in latency indicates a shift in excitation to a more centrally located site along the fibre, but they didn't rule out the possibility that the double-peak response is due to excitation by both phases.

Both latency and jitter are polarity-dependent and both phases of a biphasic stimulus pulse can elicit a discharge. The site of excitation shifts from peripheral dendritic excitation (longer latency and lower threshold) to a more centrally located site (shorter latency and higher threshold) for bipolar cathodic monophasic stimulation in the former compared to anodic stimulation in the latter (Van den Honert and Stypulkowski, 1987b). Miller *et al.* (1999b) recorded mean latencies and jitter in cats for monopolar, monophasic stimuli. Their results confirm results from previous studies that both latency and jitter are polarity-dependent, with longer latencies and greater jitter for cathodic stimuli compared to anodic stimuli. Latency and jitter are also higher for longer pulse durations, with a greater increase for cathodic stimuli compared to anodic stimuli. Both latency and jitter decrease with increasing FE, with the greatest decreases for cathodic stimuli. Some of the fibres tested have longer latencies than the average and the results indicate that these longer latency fibres have undergone greater reductions in latencies as FE increased. It is hypothesised that, given the position of the stimulating electrodes and the distribution of fibres through the cochlea, most fibres are excited centrally to the soma by both polarities, but that in a minority of the fibres excitation can occur both peripherally and centrally. There is thus a difference in the location of excitation between anodic and cathodic stimulation, consistent with observed trends in electrically stimulated neural tissue (Ranck Jr, 1975).

Bipolar, biphasic stimulation shows an order-dependent double-peak response (Van den

Honert and Stypulkowski, 1987b). Low stimulus intensity anodic first bipolar stimuli with an interphase gap show a long latency suprathreshold second peak response. With increased stimulus intensity, the response pattern becomes bimodal, with the first peak growing in intensity. For high stimulus intensities the second peak disappears and only the shorter latency first peak is elicited. It is concluded that the second peak is destroyed by the antidromic propagation of the first peak from a more central location to the peripheral dendritic sites, rendering the peripheral sites refractory during the times that the second peak should have been elicited. This same trend is also reported by Javel *et al.* (1987) using biphasic, no interphase gap stimuli. The bimodal response patterns have also only been observed during biphasic stimulation and not during monophasic stimulation. When the polarity is reversed, only a single-peak response is observed owing to the cathodic-first stimulation pulse, with no bimodal response pattern or observed shift in latency. The authors reasoned that the orthodromic propagation of the cathodic pulse response renders the more centrally located excitation site of the anodic pulse response refractory during its stimulus period.

A similar bimodal response pattern is also observed by Miller *et al.* (1999b). At low stimulus intensities only one long-latency response peak is observed, but at stimulus levels producing almost 100% FE, a discreet jump to a second shorter-latency response peak is observed. At high stimulus levels, only the shorter-latency peak is observed, consistent with the results from previous studies. Note, however, that in the previous studies (Javel *et al.*, 1987; Van den Honert and Stypulkowski, 1987b), bimodality is observed with biphasic stimuli in which each of the phases can elicit a response (Van den Honert and Stypulkowski, 1987b), whereas in the Miller *et al.* (1999b) study it is observed with monophasic stimuli only about 2% of tested fibres. Bimodality seems to be polarity-dependent, with some cats responding bimodally to anodic stimuli and others responding to cathodic stimuli. Since previous studies with monophasic stimuli (see for example Van den Honert and Stypulkowski, 1984) indicate no bimodality and the Miller *et al.* (1999b) study reports a very low incidence of bimodality, the authors caution against the conclusion of the influence the soma has on latency shifts observed with biphasic stimuli (see for example Shepherd and Javel, 1997). The discreet shift to shorter latencies is consistent with previous conclusions of a shift in excitation site from a more peripheral to a more central location across an unstimulable fibre segment such as the soma.

NRT measurements in human subjects implanted with the Nucleus 24 electrode arrays

also indicate the existence of similar response waveforms having either single positive or double positive peaks (see for example Lai and Dillier, 2000). The NRT waveform is characterised by a negative (*N1*) peak, followed by the positive peak(s) (*P1* and *P2*). For a single positive peak waveform, the *N1* peak occurred around 0.3 – 0.4 ms and the *P1* peak around 0.6 – 0.7 ms. In the double positive peak responses, the *N1* peak occurred at times too short to measure with the NRT system (< 0.11 ms), while the *P1* and *P2* peaks occurred around 0.4 – 0.5 ms and 0.6 – 0.7 ms respectively. Calculated latencies for the single-peak case are hence ~ 0.3 ms, while for the double-peak case it is ~ 0.4 ms and ~ 0.7 ms. Lai and Dillier (2000) concluded that the double-peak response indicates the existence of almost intact ANF fibres, while the single-peak response may be due to retrograde degeneration.

Miller *et al.* (1999a) used a phenomenological approach to develop an empirical model simulating ECAP responses. The model is based on their single-fibre cat data for cathodic responses from the Miller *et al.* (1999b) study. The model results confirm the decrease in both mean latency and jitter with an increase in stimulus intensity. The ECAP morphology is also polarity-dependent, with cathodic responses measured in guinea-pig and cat indicating longer latencies than measured for anodic responses (Miller, Abbas, Rubinstein, Robinson, Matsuoka and Woodworth, 1998; Miller *et al.*, 2001a; Miller, Robinson, Rubinstein, Abbas and Runge-Samuelson, 2001b). For cathodic stimuli, latencies in general also increase when the MPI is decreased (Miller *et al.*, 2001a), while longer latencies are also observed for monophasic stimuli compared to biphasic stimuli (Miller *et al.*, 2001b).

2.5.3 Threshold

Threshold indicates the stimulus level at which a firing response is elicited from a fibre. Miller *et al.* (1999b) used a slightly different definition of threshold, defining threshold to be at 50% FE.

Van den Honert and Stypulkowski (1984) reported lower thresholds for damaged fibres than for electrically stimulated normal fibres. Strength-duration curves also indicate lower thresholds at longer pulse durations for both normal and damaged fibres, with a significant reduction in threshold for damaged fibres compared to normal fibres for bipolar stimulation. Also no correlation is found between threshold and characteristic

frequency. The authors reasoned that the difference in threshold behaviour suggests a difference in site of spike initiation, with excitation of the peripheral dendrites the most likely place for low stimulus intensities with both monopolar and bipolar intracochlear electrodes for normal fibres. Also no significant difference in threshold is found between extracochlear monopolar and intracochlear bipolar stimulation in normal fibres (Van den Honert and Stypulkowski, 1987a). In contrast, Liang, Lusted and White (1999) demonstrated threshold changes of up to 10 dB/mm near monopolar stimulated electrodes and attributed the contrast with the Van den Honert and Stypulkowski (1987a) results to the more basal placement of the electrodes in the latter study.

Results from Moxon (1971) and Kiang and Moxon (1972) showed a frequency dependency of electrical threshold for sinusoidal stimulation, with a broad minimum threshold near 100 Hz for all fibres. A local minimum around 100 pps was also observed in humans for biphasic monopolar stimulation of pulse durations longer than 400 μs (Shannon, 1985). Dynes and Delgutte (1992) used electrical sinusoidal stimulation delivered to bipolar intracochlear electrodes in acutely deafened cats. Their results indicate a monotonical increase in threshold with increasing stimulus frequency. Although the growth of threshold with frequency is more than 3.0 dB/octave in some fibres, most resemble the 3.0 dB/octave growth found in previous studies (Kiang and Moxon, 1972; Hartmann and Klinke, 1990).

Single-fibre studies by Van den Honert and Stypulkowski (1987b) and ECAP studies by Miller *et al.* (1998; 1999b; 2001a) recorded lower thresholds for cathodic monopolar stimulation than for anodic stimulation in cats, indicating a threshold dependence on stimulus polarity. The difference may be due to the observation that cathodic stimuli excite fibres more distally than anodic stimuli do, although the influence the soma plays is unclear (Miller *et al.*, 1999b). However, in guinea-pigs the situation is reversed, with anodic stimuli yielding lower thresholds (Miller *et al.*, 1998). With bipolar stimulation no preference is observed between the stimulus polarities (Miller *et al.*, 2003). Thresholds are also lower for longer pulse durations (compare also Miller *et al.*, 2001b), with a greater decrease for anodic stimuli compared to cathodic stimuli. Javel *et al.* (1987) also reported lower thresholds for longer interpulse widths in biphasic stimuli, up to at least 300 μs/phase, and that the response behaviour of different fibres are the same, even though there is a difference in threshold among the fibres.

Thresholds are reported to be dependent on stimulus mode and electrode configuration. Monopolar stimulation in cats yielded thresholds 7.0 – 8.0 dB lower than bipolar stimulation (Black and Clark, 1980; Black *et al.*, 1983; Rebscher *et al.*, 2001), while in guinea-pigs monopolar thresholds are on average 5.7 dB lower (Miller, Woodruff and Pfingst, 1995). ECAP studies on cats confirmed earlier reports of lower thresholds for monopolar stimulation (Miller *et al.*, 2003). Lower thresholds are also recorded for monophasic stimuli compared to biphasic stimuli in single-fibre and ECAP studies performed by Miller *et al.* (1995; 1999b; 2001b) on cats and guinea-pigs. Increasing the duration of the second phase of the biphasic stimuli, i.e. stimulation with pseudomonophasic stimuli, leads to a relatively large reduction in threshold (Miller *et al.*, 2001b). Reversal of stimulus polarity results in larger observed threshold differences when monophasic stimulation is used (Miller *et al.*, 1999b), compared to the differences observed with biphasic stimuli (Shepherd and Javel, 1999). Van Wieringen *et al.* (2005), Van Wieringen, Carlyon, Macherey and Wouters (2006) and Macherey *et al.* (2006) investigated the effects of pulse shape, polarity and pulse rate of pulsatile waveforms on thresholds and MCLs in humans and reported threshold reductions of 3.0 – 6.0 dB when biphasic pulses are replaced with pseudomonophasic pulses, while the threshold is reduced by 5.0 – 8.0 dB in the case of alternating monophasic pulses.

2.5.4 The threshold-distance relationship

Electrode-to-axon distances play a significant role in the distribution of threshold responses to stimuli. For a monopolar electrode in an isotropic medium, the electric field strength varies with inverse proportionality to the square of the distance from the electrode, while the extracellular potential varies with inverse proportionality to the distance from the electrode. The further away from the electrode, the weaker both the electric and potential fields become, the former more quickly than the latter, with the result that larger threshold stimulus currents are necessary to excite the fibre as the electrode-to-axon distance increases.

Single-fibre studies by Ranck Jr (1975) and model results by, among others, Rattay (1990) indicate that the threshold current increases with the square of the distance from the electrode. This has the effect that as the fibre distance from the electrode increases, the excitation region around the electrode increases, since more Ranvier nodes will fall inside the depolarised region.

Javel *et al.* (1987) reported lower thresholds for fibres located closer to the stimulating electrodes. Fibres located further from the stimulating electrode could only be excited at higher stimulus intensities. Miller, Abbas and Brown (1993) and Shepherd *et al.* (1993) showed large threshold changes and growth rate of the fibre's ECAP response when the location of the intracochlear stimulus electrode was changed. Modelling data by Briaire and Frijns (2006) and Hanekom (2001b) also predicted a reduction in neural threshold as the stimulating electrodes were moved closer to the modiolus, with the greatest reduction for fibres lying closest to the electrodes.

2.5.5 Strength-duration relationship

The strength-duration function gives the relationship between the threshold stimulus current necessary to excite a fibre and the stimulus duration. The standard way of collecting data for such a function is to stimulate with a monopolar, monophasic block (square) pulse (Loeb, White and Jenkins, 1983). Since the neural membrane integrates the stimulus current, longer stimulus duration requires less threshold current than shorter durations. An increase in the stimulus duration leads to a monotonic decrease in threshold current, until it reaches an asymptotic value known as the rheobase current (Bostock, 1983).

The shape of the strength-duration curve gives an indication of the integration properties of the neural membrane. Curves can be represented by an exponential function (Lapicque, 1907), or by a hyperbolic function (Bostock, 1983; Colombo and Parkins, 1987). A perfect integrator will be represented by a hyperbolic and a leaky integrator by an exponential function respectively. Strength-duration curves measured by Van den Honert and Stypulkowski (1984) for both normal and damaged cat fibres follow an exponential curve. For the damaged fibres, thresholds at short pulse durations were lower than for the normal fibres, most probably due the fact that the damaged fibres were only excited in the axonal (central) part of the fibre, whereas in normal fibres excitation could occur either peripherally or centrally.

Chronaxie time, i.e. the stimulus duration of twice the rheobase current, is a convenient way of characterising the neural membrane integration properties. The steeper the slope of the strength-duration curve, i.e. the more the hyperbolic the curve becomes, the shorter the chronaxie time (Bostock, 1983; Colombo and Parkins, 1987).

Van den Honert and Stypulkowski (1984) reported significantly shorter (118 μs vs. 276 μs) chronaxies for laminectomated fibres (leaving only the axons intact) compared to normal functioning fibres, indicating axonal excitation in the former.

According to Abbas and Miller (2004) chronaxies depend on:

- the shape of the externally applied electric field, together with the membrane depolarisation profile (see also Bostock, 1983).
- the electrode-axon distance. A closer separation may lead to a decrease of the strength-duration time constant and thus shorter chronaxies.
- the stimulus waveform. Miller *et al.* (1995) reported longer chronaxies and less steeply sloped strength-duration functions for monophasic than for biphasic stimulation. Also, owing to the refractory properties of the neural membrane, the second phase of a biphasic pulse has a greater effect for short pulse durations, compared to longer pulse durations.

Chapter 3

HUMAN RANVIER NODE MODEL

Smit, J. E., Hanekom, T. and Hanekom, J. J. (2008) Modelled temperature-dependent excitability behaviour of a single Ranvier node for a human peripheral sensory nerve fibre, *in review*

3.1 INTRODUCTION

The present study focusses on the development of a new human Type I ANF model. The ANF model is developed in three phases. This chapter deals with the first phase, namely the development of the human Ranvier node model. Its objective is to determine whether the Hodgkin-Huxley (HH) model for unmyelinated nerve fibres can be modified to describe action potential dynamics at Ranvier nodes using recorded ionic membrane current data from single human myelinated peripheral nerve fibres (Reid *et al.*, 1993; Scholz *et al.*, 1993; Schwarz *et al.*, 1995; Reid *et al.*, 1999) together with the temperature dependency of all parameters. Only the model parameters are modified to those of human, with the equations left unaltered. This model is developed as part of a larger model to describe excitation behaviour in a generalised human peripheral sensory nerve fibre.

3.2 MODEL AND METHODS

3.2.1 Parameters applied to the nodal model

In the original Hodgkin-Huxley (Hodgkin and Huxley, 1952) formulation, the change in the membrane potential (V) is described by

$$C_m \frac{dV}{dt} = -I_{ion} + I_{stim} \qquad \left[\mu A/cm^2\right], \tag{3.1}$$

with V offset by the resting membrane potential (V_{res}) and having an initial value $V(0)$ equal to 0. The time dependent ionic membrane current (I_{ion}) consists of a fast activating and inactivating sodium ion (I_{Na}) current, a fast activating potassium ion (I_{Kf}) current and a leakage (I_L) current

$$I_{ion} = g_{Na}^{max} m^3 h \left(V - V_{Na}\right) + g_K^{max} n^4 \left(V - V_K\right) + g_L \left(V - V_L\right) \qquad \left[\mu A/cm^2\right]. \tag{3.2}$$

Ionic currents are considered ohmic and are given in terms of the ionic conductances and change in membrane potential. Ion channel activation and inactivation probability dynamics (m, h and n respectively) are described by

$$\frac{dx}{dt} = \alpha_x \left(V\right)\left[1 - x\right] - \beta_x \left(V\right) x, \quad x = m, n, h \tag{3.3}$$

with initial values $m(0) = 0.5$, $h(0) = 0.6$, $n(0) = 0.32$, and given in terms of the voltage dependent opening and closing rates of the ion channels $\alpha(V)$ and $\beta(V)$; the latter giving an indication of the membrane's permeability to the specific species of ion.

In this study, the above equation set was modified by changing the parameter values describing the ionic and leakage conductances, corresponding equilibrium potentials, the membrane rest potential and membrane capacitance to reflect the corresponding parameter values of human, while leaving the equations unaltered. These parameters are considered temperature independent in the original HH model and only the temperature dependence of the ion channel activation and inactivation rate equations is taken into account through the use of Q_{10} factors (Hodgkin and Huxley, 1952). However, given the role that temperature plays in nerve fibre excitation behaviour, temperature dependency of the parameters was included into the new nodal model.

Lastly, the membrane's permeability to different ion species was increased or decreased by multiplying the $\alpha(V)$ and $\beta(V)$ rate equations by selected factors, as mentioned by Huxley in an article on the movement of ions during nerve stimulation (Huxley, 1959).

The ionic membrane currents in the new nodal model have been described in terms of temperature dependent sodium (g_{Na}), potassium (g_K) and leakage (g_L) ionic conductances, as well as ionic equilibrium potentials

$$\begin{aligned} I_{ion}(T) = g_{Na}^{max}(T)\, m^3 h\,(V - V_{Na}(T)) + g_K^{max}(T)\, n^4\,(V - V_K(T)) \\ + g_L(T)\,(V - V_L(T)) \qquad \left[\mu A/cm^2\right], \end{aligned} \tag{3.4}$$

and the $\alpha(V)$ and $\beta(V)$ rate equations by

$$\alpha_m, \alpha_{ns} = AQ_{10}^{(T-T_0)/10} \cdot \frac{B - CV}{D\,(\exp(B - CV)) - 1} \qquad [m/s], \tag{3.5a}$$

$$\beta_m, \beta_{ns}, \alpha_h = AQ_{10}^{(T-T_0)/10} \cdot B \exp\left(\frac{-V}{C}\right) \qquad [m/s], \tag{3.5b}$$

$$\beta_h = AQ_{10}^{(T-T_0)/10} \cdot \frac{1}{(1 + \exp(B - CV))} \qquad [m/s]. \tag{3.5c}$$

Acceleration of the activation and inactivation of the membrane's permeability to specific ion species, as suggested by Huxley (1959), is given by parameter **A** values (Table 3.1). Parameters **B**, **C** and **D** are the original HH model parameters which are considered constant (Hodgkin and Huxley, 1952).

In myelinated nerve fibres the total nodal I_{Na} is subdivided into two functionally distinct currents, where the largest proportion ($\sim 98\%$) has fast activating and inactivating kinetics (Burke *et al.*, 1999). Even though the HH model has a fast activating and inactivating I_{Na}, when an action potential simulated at 25 °C was compared to a similar human nerve fibre action potential from the Schwarz *et al.* (1995) study, the activation was too slow to describe the action potential rising phase in the human case. Activation and inactivation of I_{Na} was hence accelerated, as shown in Table 3.1 (parameter **A** values).

Voltage-gated potassium (K_v) channels provide a number of useful functions to the nerve fibre, including setting and regulating the membrane resting potential, regulating the amplitude and duration of action potentials and determining the frequency of firing (Hille, 2001). Three types of K_v channels have been measured in rat and human,

Table 3.1: Parameters used for calculation of the voltage dependent opening and closing rates of the ion channels.

Parameter	$\mathbf{Q_{10}}$	$\mathbf{T_0}$ **(°C)**	**A**	**B**	**C**	**D**
α_m	2.78	20	4.42	2.5	0.1	1
β_m	2.78	20	4.42	4.0	18	–
α_h	1.5	20	1.47	0.07	20	–
β_h	1.5	20	1.47	3.0	0.1	–
α_{ns}	1.5	20	0.20	1.0	0.1	10
β_{ns}	1.5	20	0.20	0.125	80	–

namely those with fast kinetics (K_f or F-channels), intermediate kinetics (K_i or I-channels) and slow kinetics (K_s or S-channels) (Röper and Schwarz, 1989; Reid *et al.*, 1993; Safronov *et al.*, 1993; Scholz *et al.*, 1993; Schwarz *et al.*, 1995). F- and I-channels cluster mostly under the myelin sheath, with only a few channels located at the node (Röper and Schwarz, 1989; Rasband, 2006). It has been suggested that these channels mediate I_{Kf}, but in mammals the activation of nodal I_{Kf} is too small to contribute significantly to the repolarisation of the action potential (Chiu *et al.*, 1979; Reid *et al.*, 1999). S-channels co-locate with sodium channels at the Ranvier node, where it activates and deactivates more slowly than the F- and I-channels and does not inactivate (Taylor, Burke and Heywood, 1992; Devaux, Kleopa, Cooper and Scherer, 2004; Schwarz, Glassmeier, Cooper, Kao, Nodera, Tabuena, Kaji and Bostock, 2006). Even though the S-channels' kinetics are considered too slow to contribute significantly to firing behaviour and are thus neglected in most models, a slow (I_{Ks}) potassium current is included in some human nerve fibre models (Schwarz *et al.*, 1995; Bostock and Rothwell, 1997). The HH model I_K contains only activation kinetics, which renders it suitable for use as I_{Ks}. Its activation kinetics was hence slowed down (parameter **A** values in Table 3.1).

Schwarz *et al.* (1995) measured ionic membrane currents and action potentials at Ranvier nodes from partially demyelinated human peripheral sensory nerve fibres, but no morphometric nerve fibre data were supplied. Wesselink *et al.* (1999) estimated the action potential rise and fall times and amplitudes at 20 and 25 °C from the aforementioned study, as well as predicted values at 37 °C, and these values were used for the nodal model validation.

Both Schwarz *et al.* (1995) and Wesselink *et al.* (1999) used a reference temperature

(T_0) of 20 °C, while Hodgkin and Huxley (1952) used a reference temperature (T_0) of 6.3 °C. To aid comparison with these models, the reference temperature for the new nodal model was changed to 20 °C. Optimisation of parameters was performed at this temperature and the action potential shape and amplitude compared to the corresponding estimated data from the aforementioned studies. Next, the temperature dependence of the rate equations, as expressed through Q_{10} factors, was determined by comparing simulated and estimated action potential shapes and amplitudes at 25 and 37 °C (Table 3.1).

Results from experimental studies by Reid *et al.* (1993), Scholz *et al.* (1993) and Schwarz *et al.* (1995) were used to deduce conductance and equilibrium potential values for the ionic membrane currents (Table 3.2). The equilibrium potentials were given in terms of the Nernst potential equations for the different ion species (Hille, 2001)

$$V_{Na}, V_K, V_L = \frac{1000RT_K}{F} \ln\left(\frac{[ion]_o}{[ion]_i}\right) - V_{rest} \qquad [mV]\,, \tag{3.6}$$

with R the universal gas constant, F the Faraday constant, T_K the absolute temperature (in Kelvin) and $[ion]_o/[ion]_i$ the extracellular to intracellular ion concentration ratio for Na^+, K^+ and leakage ions respectively (Table 3.2). The K^+ concentration ratio (K_{cr}) was calculated using the intra- and extracellular concentration values from Schwarz *et al.* (1995); who also measured a leakage current with a V_L of -84.0 mV at 20 °C, resulting in a leakage ion concentration ratio (L_{cr}) of about 0.036. This value was further optimised until the simulated action potential's recovery phase resembled those of the Schwarz study's action potential. Estimating a Na^+ concentration ratio (Na_{cr}) proved difficult, with previously reported values ranging from 4.4 to 14.05 (Scholz *et al.*, 1993; Schwarz *et al.*, 1995; Wesselink *et al.*, 1999; Hille, 2001). The value therefore had to be optimised for the model and this turned out to be only slightly higher than the original HH model value of 6.48 (Table 3.2).

Values for the resting membrane potential (V_{res}) at different temperatures were estimated by optimising the value until the membrane potential returned to 0 mV after stimulation. Hence, a value of -79.4 mV was estimated at 6.3 °C and became more negative as the temperature was increased to 37 °C, having a Q_{10} factor of 1.0356 for all $T \leq 20$ °C and 1.0345 for all $T > 20$ °C (Table 3.2). This gave a V_{rest} of -83.3 mV at 20 °C and -88.1 mV at 37 °C.

Table 3.2: Model electrical parameters.

Parameter	**Value**	**Q_{10}**	**T_0 (°C)**	**Reference**
Membrane resting potential (V_{rest})	-79.4 mV	1.0356 (T $\leq$ 20 °C) 1.0345 (T > 20 °C)	6.3	Hodgkin and Huxley (1952), Schwarz *et al.* (1995), Wesselink *et al.* (1999) †
Gas constant (R)	8.3145 J/K.mol			Atkins (1995)
Faraday constant (F)	9.6485×10^4 C/mol			Atkins (1995)
$[Na^+]_o/[Na^+]_i$	7.2102			Hodgkin and Huxley (1952), Schwarz *et al.* (1995), Wesselink *et al.* (1999), Hille (2001) #
$[K^+]_o/[K^+]_i$	0.0361			Reid *et al.* (1993), Scholz *et al.* (1993), Schwarz *et al.* (1995)
$[Leakage]_o/[Leakage]_i$	0.036645			Scholz *et al.* (1993), Schwarz *et al.* (1995) ††
Na^+ conductance (g_{Na})	640.00 mS/cm^2	1.1	24	Scholz *et al.* (1993), Hille (2001)
K^+ conductance (g_K)	60.0 mS/cm^2	1.16	20	Reid *et al.* (1993), Scholz *et al.* (1993), Schwarz *et al.* (1995) ††
Leakage conductance (g_L)	57.5 mS/cm^2	1.418	24	Schwarz and Eikhof (1987), Scholz *et al.* (1993), Schwarz *et al.* (1995) ††
Axoplasmic resistivity (ρ_{ax})	0.025 kΩ.cm	$(1.35)^{-1}$	37	Wesselink *et al.* (1999) †
Membrane capacitance (c_{mem})	2.8 μF/cm^2			Schwarz *et al.* (1995) *

† Value deduced from reference(s) and then optimised for model. Q_{10} value not from reference, but optimised for model

Discrepancy exists between HH model value and values for human. Value hence optimised for model

†† Values deduced from reference(s) and corrected for concentration and temperature differences

* Considered constant for temperatures between 20 °C and 42 °C

Since experimental study temperatures range from 20 – 27 °C, a Q_{10} factor for the potassium conductance (g_K) could be estimated. Leakage conductances (g_L) were measured by Scholz *et al.* (1993) and Schwarz *et al.* (1995), but not enough information was available to calculate the temperature dependence. However, g_L values were measured at 20 and 37 °C in rat, giving a Q_{10} factor of 1.418 (Schwarz and Eikhof, 1987). Estimation of the sodium conductance (g_{Na}) was more difficult, with only one study reporting a single channel value of about 13 pS (Scholz *et al.*, 1993). To convert the single channel conductance to a value for g_{Na}, the Na^+ channel density needed to be known and in mammals Na^+ channel densities vary between 700 and 2,000 /μm^2 (Hille, 2001). Also, the conductances of ion channels increase very little with a temperature increase, with Q_{10} factors typically in the vicinity of the values for aqueous diffusion; ranging from 1.0 – 1.6 in most cases (Hille, 2001). The values for g_{Na} and its Q_{10} factor played an important role in determining the action potential amplitude and were optimised by comparison with the calculated amplitudes at 20, 25 and 37 °C from Wesselink *et al.* (1999). To measure the time course and voltage dependence of activation and inactivation characteristics for ionic membrane currents, the current amplitude has to be sufficiently large so that it can be detected (Schwarz *et al.*, 2006). Hence, in experimental studies intra- and extracellular replacement Ringer solutions are substituted with isotonic concentration solutions to increase the current amplitudes, but this results in higher conductance values. Thus, conductance values had to be corrected for such concentration differences.

Similar to Wesselink *et al.* (1999) the electrical parameters were recalculated as values per unit area by assuming a fibre diameter of 15 μm and a nodal area of 50 μm^2. A nodal membrane capacitance (C_m) of 1.4 pF, i.e. a c_m of 2.8 μF.cm^{-2}, was used (Schwarz *et al.*, 1995). For squid, a positive temperature coefficient of about 1.36% per °C for C_m is found in the temperature range 3 – 21 °C, with no significant change in the range 21 – 42 °C and a sharp increase of at least 23% per °C for temperatures above 42 °C (Palti and Adelman Jr., 1969). Since no similar studies were performed for mammals, c_m was assumed to be constant over the temperature range 20 – 37 °C. The axoplasmic resistivity (ρ_{ax}) of the membrane did not influence the action potential shape and amplitude, and a value of 0.025 kΩ.cm at 37 °C and a Q_{10} factor of $(1.35)^{-1}$ were used (see Section 4.2).

3.2.2 Model output calculations

All the model output calculations were performed in Matlab. The modified equations were solved numerically using the ordinary differential equation (ODE) ode15s numerical solver, since they were too stiff to solve using the ode23t and ode45 solvers. The modelled node was externally stimulated using a monopolar external electrode positioned midway along the nodal length and 0.1 cm from the node. The external environment was considered infinite, isotropic and homogeneous with an external resistivity (ρ_e) of 0.3 kΩ.cm at 37 °C (Frijns *et al.*, 1994). External stimulation was thus considered purely resistive and given by

$$V_e = \frac{\rho_e I_{stim}}{4\pi r_{dist}} \quad [mV]\,, \tag{3.7}$$

with r_{dist} the distance between the node and the electrode.

Action potential (AP) characteristics include amplitude, duration, strength-duration behaviour, refractory period and conduction velocity. Since the nodal model only described APs generated at a single Ranvier node, refractory period and conduction velocity calculations could not be performed and have therefore not been dealt with in this chapter. AP duration is the sum of the rise and fall times. The AP is approximated by a triangle, with the apex at the maximum amplitude (Frijns and ten Kate, 1994). The rising edge intersects the AP curve at 10% of the maximum amplitude and the rise time is calculated as the time difference between this intersection point and the apex. The falling time is calculated in the same manner using the falling edge.

Rheobase current and chronaxie time characterises the strength-duration behaviour. Thresholds were calculated using a monopolar external electrode with monophasic-anodic stimulation pulses ranging from 0.2 – 2.0 ms in duration. The strength-duration curve was fitted with the linear relationship

$$I_{th}t = I_{rb}\,(t + \tau_{ch})\,, \tag{3.8}$$

with I_{th} the threshold current (μA), t the pulse duration (μs), I_{rb} the rheobase current (μA) and τ_{ch} the chronaxie time (μs) (Weiss, 1901; Bostock, 1983; Wesselink *et al.*, 1999).

The model's sensitivity to the different parameters was studied using sensitivity stud-

ies. At 25 °C, parameter values were varied from 20% to 100% of their optimised values, and their influence on the rise times, fall times and amplitudes were noted.

3.3 RESULTS

3.3.1 Action potential rise and fall times

A single Ranvier node from a general peripheral sensory nerve fibre was simulated in Matlab and externally stimulated with a monopolar electrode. Stimulation pulses were square, monophasic-anodic and only single pulses were used. The simulated node had a 15 μm diameter and 50 μm^2 area.

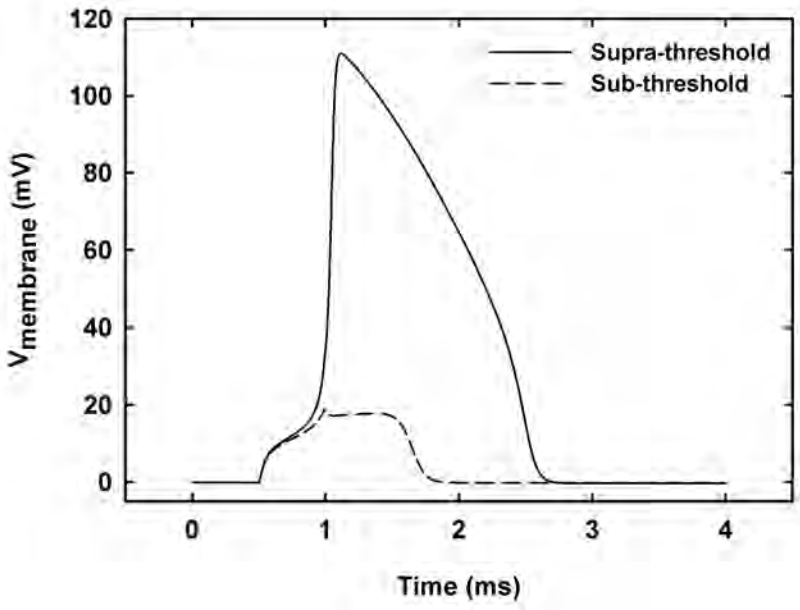

Figure 3.1: Sub-threshold and supra-threshold action potentials simulated at 25 °C.

APs were calculated at 20, 25 and 37 °C with rise and fall times compared to experimentally estimated results (Table 3.3). An example of sub-threshold and supra-threshold action potentials simulated at 25 °C are shown in Figure 3.1. The rise time

Table 3.3: Simulated characteristics of the human nodal model compared to experimentally estimated results from human Ranvier nodes.

Parameter	**Specifications**	**Value**		
	(15.0 μm fibre diameter)	**Human Node of Ranvier model**	**Experimental results**	**Reference**
Rise time (μs)	20 °C	270	270	Schwarz *et al.* (1995)
	25 °C	205	204	Schwarz *et al.* (1995)
	37 °C	123	120	Wesselink *et al.* (1999)
Fall time (μs)	20 °C	1870	1829	Schwarz *et al.* (1995)
	25 °C	1448	1464	Schwarz *et al.* (1995)
	37 °C	784	470	Wesselink *et al.* (1999)
Chronaxie (μs)	37 °C	65.5	64.9 $\pm$ 8.3	Bostock (1983)

was less than 0.5% longer than the estimated results at 25 °C and decreased by 24% (Q_{10} factor of $(1.73)^{-1}$) from 20 to 25 °C. The fall time was 2.2% longer at 20 °C and 1.1% shorter at 25 °C than the estimated results. Its decrease of 23% (Q_{10} factor of $(1.67)^{-1}$) was steeper than the 20% decrease (Q_{10} factor of $(1.56)^{-1}$) estimated from the experimental results.

Although no experimental data are available at 37 °C, a rise time of 120 μs and fall time of 470 μs has been estimated previously (Wesselink *et al.*, 1999). APs for the new nodal model had a 2.5% longer rise time and 67% longer fall time compared to these values.

Both rise and fall times were sensitive to sodium ion and leakage current parameters (Figures 3.2 and 3.3). Varying the sodium conductance Q_{10} factor values ($g_{Na}Q_{10}$) had a less than 7% influence on the rise and fall times. However, for Q_{10} values larger than 1.2 (i.e. relative parameter values larger than 1.03), the amplitude started to increase with an increase in temperature. This placed an upper limit on $g_{Na}Q_{10}$. Varying the sodium conductance (g_{Na}) had a more pronounced effect on the rise time than on the fall time. A decrease of 80% in g_{Na} increased the rise time by 100% and decreased the fall time by 70%. This was the same trend as observed for the sodium ion concentration ratio (Na_{cr}), with an increase of 30% in the rise time and a decrease of 20% in the fall time.

Surprisingly, varying the leakage current conductance (g_L) seemed to influence the rise and fall times as much as g_{Na} (Figures 3.2(b) and 3.3(b)). A 100% increase in g_L

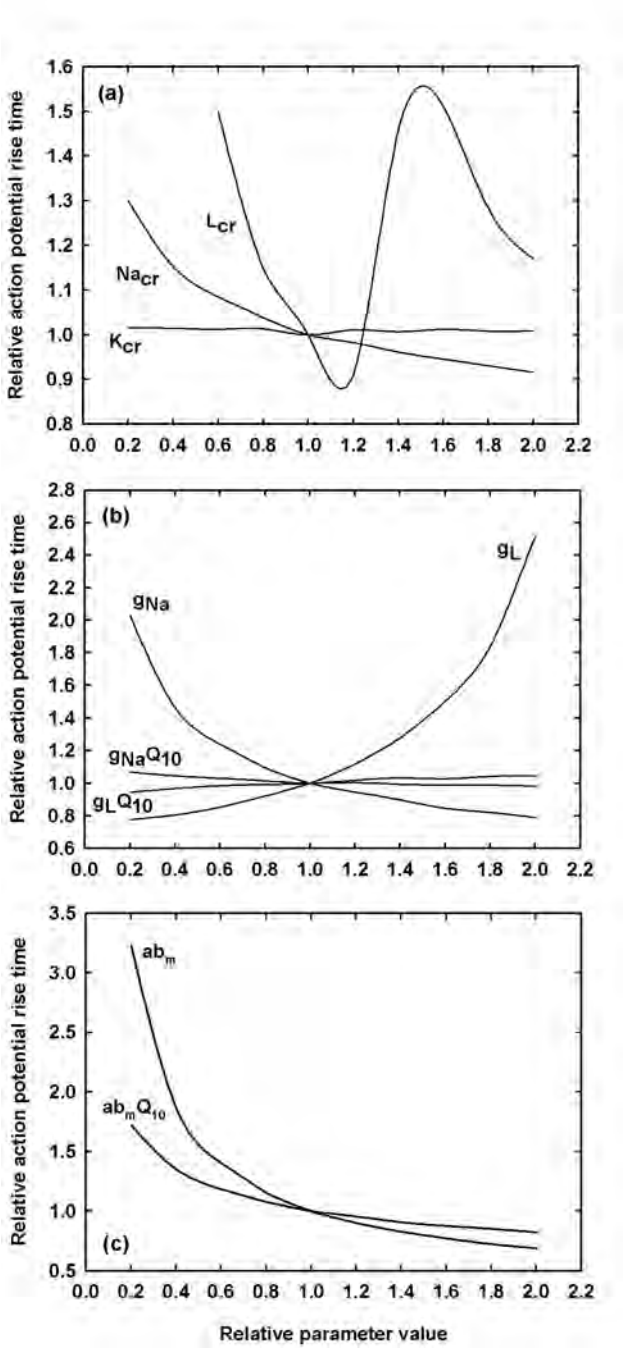

Figure 3.2: Relative sensitivity of action potential rise times to (a) sodium ion (Na_{cr}), potassium ion (K_{cr}) and leakage (L_{cr}) concentration ratios; (b) sodium conductance (g_{Na}), sodium conductance Q_{10} factor ($g_{Na}Q_{10}$), leakage conductance (g_L) and leakage conduction Q_{10} factor (g_LQ_{10}); and (c) Q_{10} factor for sodium activation rate equation (ab_mQ_{10}) and acceleration factor for sodium current activation and deactivation (ab_m). All calculations were performed at 25 °C. Parameter values were varied between 20 and 100% of the values used in the nodal model.

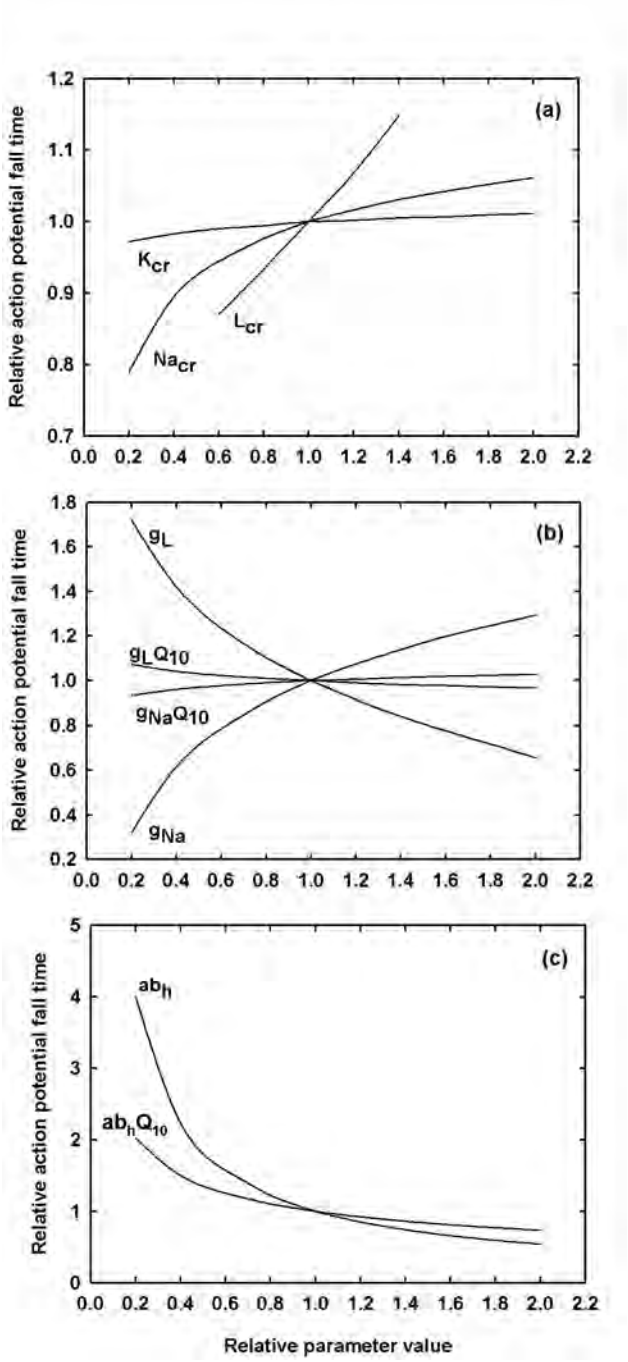

Figure 3.3: Relative sensitivity of action potential fall times (a) sodium ion (Na_{cr}), potassium ion (K_{cr}) and leakage (L_{cr}) concentration ratios; (b) sodium conductance (g_{Na}), sodium conductance Q_{10} factor ($g_{Na}Q_{10}$), leakage conductance (g_L) and leakage conduction Q_{10} factor (g_LQ_{10}); and (c) Q_{10} factor for sodium activation rate equation (ab_hQ_{10}) and acceleration factor for sodium current activation and deactivation (ab_h). All calculations were performed at 25 °C. Parameter values were varied between 20 and 100% of the values used in the nodal model.

increased the rise time by 150%, while decreasing the fall time by 35%. Decreasing g_L by 80% decreased the rise time by 22%, while the fall time increased by 70%. Similar to $g_{Na}Q_{10}$, the leakage conductance Q_{10} factor values (g_LQ_{10}) influenced the rise and fall times by less than 6%, with decreased values having a slightly larger effect than increased values.

The leakage concentration ratio (L_{cr}) seemed to have a large effect on the rise and fall times (Figures 3.2(a) and 3.3(a)). Fall times increased with an increase in L_{cr}, with no clear trend established for the rise time predictions. No action potentials could be elicited below a relative value of 0.60. In Section 3.2 it was mentioned that the membrane potential ($V(t)$) was offset by the membrane resting potential (V_{rest}), with initial value $V(0) = 0$. Decreasing L_{cr} to a relative value of 0.6 increased the offset value needed to reset $V(t)$ to zero by about -13 mV. Increasing L_{cr} two-fold raised the beginning phase of the AP's up-stroke by about 18 mV and the tail part and subsequent recovery phase of the down-stroke by about 21 mV creating the impression that the AP did not inactivate. These changes thus distorted the AP's shape. Considering the triangle method used to calculate the rise and fall times, the shape characteristics might be less sensitive to L_{cr} than indicated.

The rising phase of the AP was influenced by sodium activation kinetics (Figure 3.2(c)), with sodium inactivation kinetics having a less than 5% influence. The opposite held true for the falling phase (Figure 3.3(c)). Potassium activation kinetics had a less than 2% influence on either phase; and potassium ion concentration ratio (K_{cr}) less than 3%. K_{cr} showed the same tendency as L_{cr} to lower or raise the up-stroke and down-stroke current level, but much less pronounced as in L_{cr}.

3.3.2 Action potential amplitude

Calculated amplitudes around 116.7 mV were obtained at 20 and 25 °C, with the amplitude decreasing by less than 1% from 20 to 25 °C, while at 37 °C the amplitude was slightly larger than 115 mV. These results followed the trend of an amplitude decrease with temperature increase (Buchthal and Rosenfalck, 1966; Schwarz and Eikhof, 1987; Frijns *et al.*, 1994; Wesselink *et al.*, 1999).

The amplitude was most sensitive to g_{Na}, g_L and Na_{cr}, while it appeared to be less

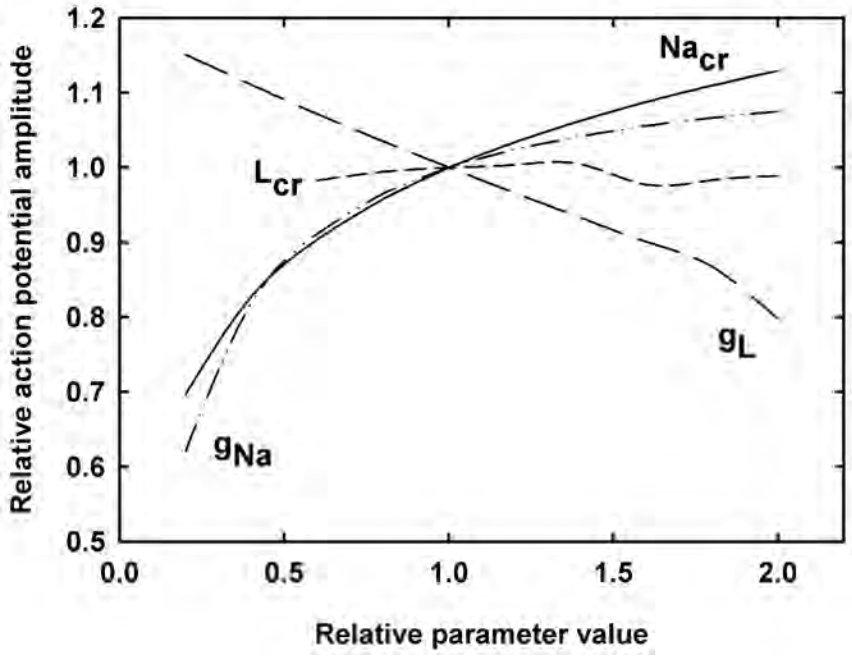

Figure 3.4: Relative sensitivity of action potential amplitude to sodium and leakage conduction and ion concentration ratio parameters, calculated at 25 °C. Nomenclature is the same as in Figures 3.2 and 3.3. Parameter values were varied between 20 and 100% of the values used in the nodal model.

so for L_{cr} (Figure 3.4). However, when the amplitude was corrected for the rise in the tail part of the action potential, in effect the amplitude was increased when L_{cr} was decreased, while an increase in L_{cr} decreased the amplitude. The corrected curve thus closely followed the g_L curve. For the other parameter values the variation in amplitude was less than 2.5%.

3.3.3 Strength-duration relationships

Strength-duration relationships were calculated at temperatures between 20 and 37 °C; with a calculated chronaxie time constant (τ_{ch}) of 65.5 μs at 37 °C (Table 3.3).

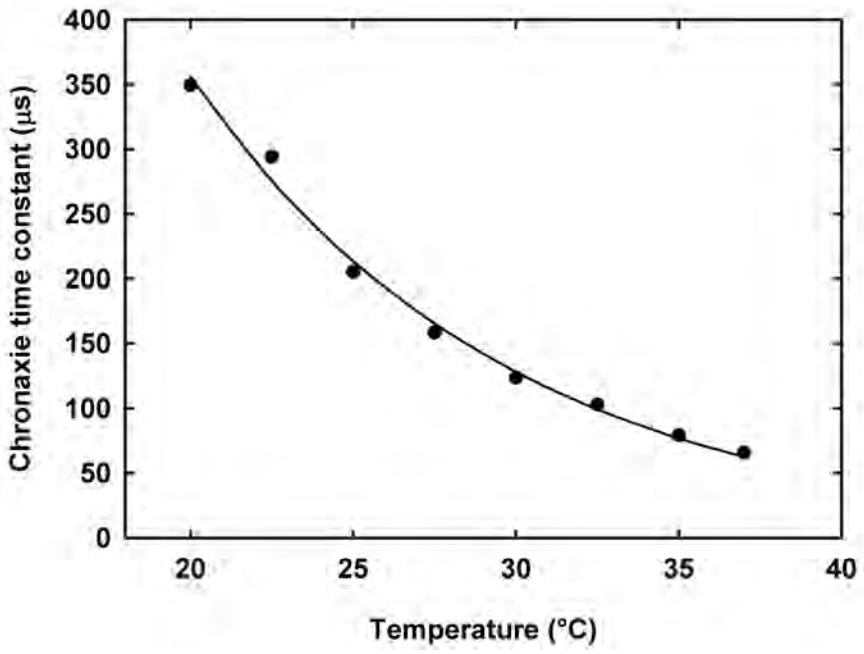

Figure 3.5: Temperature dependence of the chronaxie time constant for a single Ranvier node. Filled symbols indicate the simulated chronaxie times. The curve is obtained by regression fitting of a decaying exponential function, and corresponds to a Q_{10} of $(2.78)^{-1}$.

τ_{ch} values increased by 89% with a temperature decrease from 37 to 30 °C, corresponding to a Q_{10} factor of $(2.48)^{-1}$ (Figure 3.5), while rheobase current values decreased by

51.6% over the same temperature interval. The temperature dependence of τ_{ch} could be fitted by an exponential relationship, corresponding to a Q_{10} factor of $(2.78)^{-1}$, which is larger than the calculated Q_{10} factor.

3.4 DISCUSSION

The development of a model of a Ranvier node in a general human peripheral sensory nerve fibre was based on the HH model, modified with recorded ionic membrane current data from single human myelinated peripheral nerve fibres (Reid *et al.*, 1993; Scholz *et al.*, 1993; Schwarz *et al.*, 1995; Reid *et al.*, 1999). Temperature dependence of all parameters was included. Simulation results suggested the possibility of modifying the original HH model to describe AP excitation characteristics in human sensory nerve fibres.

Rate equation Q_{10} factors, for a reference temperature of 20 °C, tend not to differ much between previously developed models. Q_{10} factors of 2.9 and 3 are used for sodium inactivation and potassium activation respectively (Schwarz and Eikhof, 1987; Schwarz *et al.*, 1995; Wesselink *et al.*, 1999), while 2.2 are most commonly used for sodium activation (Schwarz and Eikhof, 1987; Schwarz *et al.*, 1995). Wesselink *et al.* (1999) used a value of 1.7 for the sodium activation; based on the Q_{10} factor for the measured decrease in rise time between 20 and 25 °C. Moore *et al.* (1978) used a Q_{10} factor of 3 for all rate constants in their standard high-density HH model. Optimisation of these factors for the new nodal model produced a sodium inactivation Q_{10} factor of 1.5, very close to the estimated value of 1.56 describing the experimentally observed decrease in fall time between 20 °C and 25 °C. The potassium activation kinetics had a less than 1% influence on the fall time and thus practically any Q_{10} factor value could be used. However, since this value tends to be fairly similar to the value of sodium inactivation, it was decided to use a value of 1.5 as well. The Q_{10} factor of 2.78 for the sodium activation kinetics was higher than the value of previous models, resulting in a 49% higher sodium activation at 37 °C compared to the Schwarz *et al.* (1995) results. This is in contrast to the 30% lower sodium activation at 37 °C from the Wesselink *et al.* (1999) model. These differences might be attributed to the optimisation procedure. Parameter values were hand-tuned and the possibility exists that the final solution converged to a local optimum in the solution space rather than to the global optimum,

and that a more efficient optimisation routine would be required instead (Huys, Ahrens and Paninski, 2006).

Since I_{Ks} actives and deactivates slowly, and does not inactivate, its influence on the AP shape and amplitude is almost insignificant when nerve fibres are stimulated with short duration pulses (Reid *et al.*, 1993; Schwarz *et al.*, 2006). The relative insensitivity of the simulated characteristics of I_{Ks} compared favourably to the experimental observations. Schwarz *et al.* (1995) measured a leakage current with a leakage equilibrium potential of -84.0 mV at 20 °C, resulting in an L_{cr} of about 0.036. This value is similar to the K_{cr} value (Table 3.2). Since part of the I_{Ks} current is already activated at the resting membrane potential (Schwarz *et al.*, 2006), it might be assumed that a large part of I_L consists of I_{Ks} and not from a current carried by chloride ions as in the original HH model (Hodgkin and Huxley, 1952). Schwarz *et al.* (2006) also showed that increasing the extracellular potassium ion concentration increases the holding current, as well as the amplitudes of the tail currents of recorded I_{Ks} currents. This concentration increase can be simulated by an increase in K_{cr}, and also L_{cr}. An increase in any one of these two parameters led to an increase in the initial AP rising phase up-stroke current, as well as the tail current of the down-stroke and subsequent recovery phase, and was hence in accordance with the Schwarz *et al.* (2006) results.

Scholz *et al.* (1993) measured voltage-dependent sodium single channels at room temperature (about 24 °C) in a Ringer solution with a Na_{cr} of about 14.05. This single channel conductance value can be converted to a value for g_{Na}, provided the Na^+ channel density is known (Hille, 2001). However, no values are known for corresponding human parameters, but for mammals the Na^+ channel densities vary from 700 to 2000 $/\mu m^2$ (Hille, 2001). Using the Scholz *et al.* (1993) values to predict a simulated AP of correct amplitude and shape required a Na^+ channel density of less than 300 $/\mu m^2$. Optimisation of Na_{cr} predicted a lower value than the Scholz *et al.* (1993) value and hence the single channel sodium conductance had to be corrected for the concentration difference. Calculation of g_{Na} then required a Na^+ channel density of 959 $/\mu m^2$. In myelinated nerve fibres a large Na^+ channel density is needed at the Ranvier node to elicit and maintain efficient and rapid propagating APs (Rasband and Trimmer, 2001), and even though the predicted nodal model value fell within the range of mammalian Na^+ channel densities, it might be an underestimation of the real density in human.

It is well known that voltage-dependent sodium channels are more homogeneously distributed along unmyelinated than in myelinated fibres, where the channels mainly cluster in high density at the Ranvier nodes (Salzer, 1997; Vabnick and Shrager, 1998; Boiko, Rasband, Levinson, Caldwell, Mandel, Trimmer and Matthews, 2001). Furthermore, in adult mammalian nerve fibres, one type of sodium channel, $Na_{v1.2}$, is restricted to unmyelinated fibres, whereas a different type, $Na_{v1.6}$, is found at the Ranvier nodes (Boiko *et al.*, 2001). Studies also show that as a myelinated axon matures from an unmyelinated state to a myelinated state, $Na_{v1.2}$ is initially expressed in the unmyelinated fibre and gradually replaced by $Na_{v1.6}$ as the fibre becomes myelinated (Vabnick and Shrager, 1998; Boiko *et al.*, 2001; Rasband and Trimmer, 2001). These two types also activate and inactivate at different voltages (Catterall, Goldin and Waxman, 2005). Differences also exist for voltage-dependent potassium (K_v) channels. For example, unmyelinated fibres have fast delayed rectifying K_v channels, whereas mammalian Ranvier nodes seem to lack these (Hille, 2001) and expresses potassium channels with slower kinetics instead (Taylor *et al.*, 1992; Devaux *et al.*, 2004; Schwarz *et al.*, 2006). Given these differences, it might be necessary to not only modify the model parameters, but also the model equations.

No studies regarding the measurement of strength-duration relationships for single human Ranvier nodes were found in literature. An average chronaxie time constant of 64.9 $\pm$ 8.3 μs is estimated at 37 °C for normal rat Ranvier nodes (Bostock, Sears and Sherratt, 1983). The chronaxie time of 65.5 μs calculated at 37 °C for the human nodal model compared favourably with this estimate. However, when the temperature dependence of the chronaxie time constant is considered, a Q_{10} factor of $(1.39)^{-1}$ is calculated when the temperature is decreased to 30 °C (Bostock *et al.*, 1983). This is almost a factor 2 smaller than the corresponding value for the human nodal model. In the nodal model the single Ranvier node was placed in an infinite, isotropic and homogeneous saline extracellular medium. In *in vitro* measurements the fluidic extracellular medium, in close proximity to the nerve fibre, consists mainly of Ringer or standard extracellular solutions for which the resistivity and corresponding temperature dependence may be different to those of saline. Also, the effect internodes have on the excitability behaviour of nerve fibres was not included in the nodal model. This effect will be studied in Chapter 4 on the temperature dependent excitability behaviour of a cable model representation of a human peripheral sensory nerve fibre.

3.5 CONCLUSION

In this chapter the possibility was examined to modify the HH model to predict excitability behaviour at Ranvier nodes when only the model parameters were modified to those of human, while the equations themselves were left unaltered. From the results it can be inferred that the new nodal model could satisfactorily predict AP shape and amplitude at different temperatures, but chronaxie times were overestimated at temperatures lower than body temperature.

The HH model equations are derived for an unmyelinated nerve fibre. Given the differences that were discussed between the ion channel kinetics and organisation at human Ranvier nodes compared to those in unmyelinated nerve fibres, it might well be that the activation and inactivation rate equations, in their original form, do not adequately describe the kinetics for the ion channel types found at the Ranvier node in a myelinated nerve fibre. Thus, in addition to the modifications made to the model parameters, the equations themselves might need to be modified to explain excitability behaviour in human peripheral sensory nerve fibres more accurately.

However, such an inference might only be drawn after the new nodal model has been incorporated into a more comprehensive nerve fibre cable model and validated against experimentally measured nerve fibre data. In the next chapter this nodal model will be incorporated into a cable model to investigate such excitability behaviour characteristics as refractory time periods and conduction velocity, as well as to better compare simulated and experimentally measured chronaxie times.

Chapter 4

GENERALISED HUMAN SENSORY NERVE FIBRE MODEL

Smit, J. E., Hanekom, T. and Hanekom, J. J. (2008) Modelled temperature-dependent excitability behaviour of a generalised human peripheral sensory nerve fibre, *in review*

4.1 INTRODUCTION

This chapter deals with the second phase in the development of the ANF model, namely the development of the generalised human peripheral sensory nerve fibre model, based on a combination of the models by Rattay *et al.* (2001b) and Blight (1985) and constructed using human sensory nerve fibre morphometric data. Ranvier node dynamics utilised the Ranvier node model described in Chapter 3. However, Bostock and Rothwell (1997) included a persistent sodium current in addition to the transient sodium current, as modelled in Chapter 3, and was therefore able to better explain chronaxie times compared to a model that only included the transient sodium current. Therefore the sensory nerve fibre model described in this chapter included this additional persistent sodium current.

The objective of this chapter is to determine if the human Ranvier node model, which is

based on a modified version of the HH model, together with the additional persistent sodium current can predict the excitability behaviour in human peripheral sensory nerve fibres with diameters ranging from 5.0 – 15.0 μm. The Ranvier node model is extended to include a persistent sodium current and is incorporated into a generalised simple double-cable nerve fibre model. Parameter temperature dependence is included.

4.2 MODEL AND METHODS

4.2.1 Parameters applied to the nerve fibre model

Rattay *et al.* (2001b) developed a nerve fibre cable model which assumes a propagating action potential driven by Hodgkin-Huxley (Hodgkin and Huxley, 1952) dynamics. The model consists of dendritic, somal and axonal sections. The dendritic and axonal sections are divided into cylindrical compartments, with alternative compartments representing unmyelinated Ranvier nodes and myelinated internodes. Membrane potential (V_n) change at the centre of the nth compartment is described by the cable equation

$$C_{m,n}\frac{(V_n)}{dt} = \left[-I_{ion,n} + \frac{(V_{n-1}+V_{e,n-1})-(V_n+V_{e,n})}{R_{n-1}/2+R_n/2} + \frac{(V_{n+1}+V_{e,n+1})-(V_n+V_{e,n})}{R_{n+1}/2+R_n/2}\right], \tag{4.1}$$

with V_n offset by the resting membrane potential (V_{res}) and having an initial value $V_n(0)$ equal to zero. $C_{m,n}$ is the membrane capacitance and R_n the axoplasmic resistance to the neighbouring sections at the nth compartment.

The proposed human nerve fibre model was based on the Rattay model, but consisted of an axonal section only (Figure 4.1). The modelled nerve fibre was externally stimulated with a monopolar electrode positioned sufficiently far away so that the propagating action potential was minimally distorted by the external potential field (V_e). The Ranvier nodes were considered unmyelinated active axolemmae utilising the new human Ranvier node model dynamics described in Chapter 3. For completeness the human nodal model equations will be given here, together with model parameter values (Tables 4.1 and 4.2), but for a more comprehensive description please refer.

In myelinated nerve fibres the total nodal sodium current (I_{Na}) is subdivided into

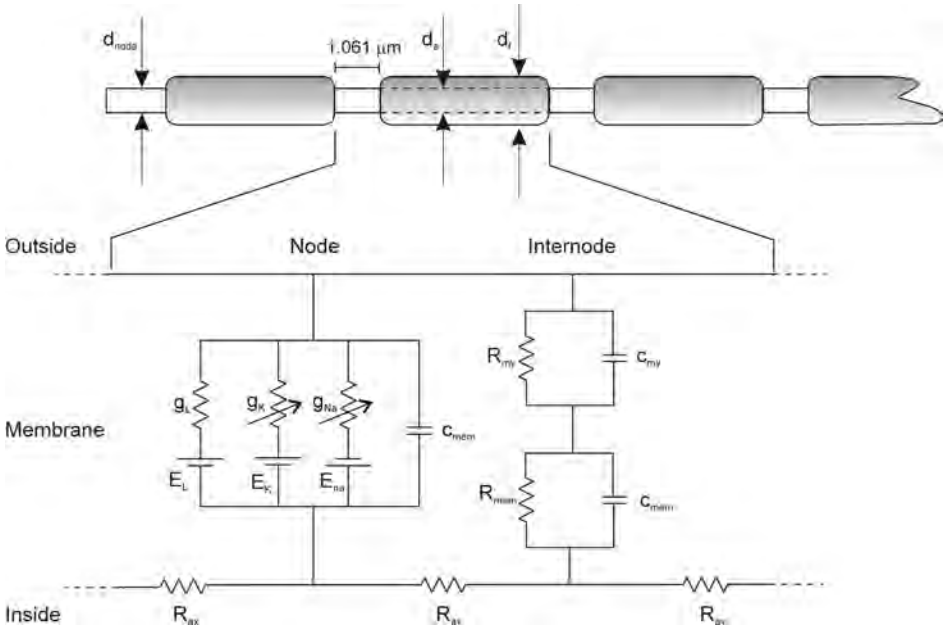

Figure 4.1: Representation of the generalised human peripheral sensory nerve fibre. The cable model consisted of a myelinated axon with 23 nodes separated by 22 internodes. Each node had a length of 1.061 μm and diameter d_{node}. The internodal axolemmal diameter (d_a) and internodal length depended on the total internodal nerve fibre diameter (d_f). The myelinated internodes were considered to be simple double cable structures as modelled by Blight (1985). In the equivalent circuit diagram the resistances and capacitances of the leaky myelin sheath (R_{my}, c_{my}) and axolemma (R_{mem}, c_{mem}) were combined together in series to form one compartment. The axoplasmic resistance (R_{ax}) was a function of the axoplasmic resistivity. The nodal circuit consisted of the axolemmal (membrane) resistance (R_{mem}) and capacitance (c_{mem}), as well as expressions for the sodium (g_{Na}), potassium (g_K) and leakage (g_L) conductances and equilibrium potentials (E_{Na}, E_K, E_L). The total nodal sodium current (I_{Na}) was subdivided into a 2.5% persistent (I_{Nap}) and 97.5% transient (I_{Nat}) sodium currents.

two functionally distinct currents. The transient sodium (I_{Nat}) current constitutes the largest proportion ($\sim$ 98%) and has fast activating and inactivating kinetics. A smaller current ($\sim$ 2%) activates equally fast, but at membrane potentials 10 – 20 mV more negative than the transient, and inactivates slowly or not at all; forming a persistent (I_{Nap}) current (Burke, Kiernan and Bostock, 2001). Schwarz *et al.* (1995) developed a human Ranvier node model including only I_{Nat}. Bostock and Rothwell (1997) developed a similar model to the one by Schwarz *et al.* (1995) and estimated chronaxie times of 176 μs at skin temperature. When the model was changed to include a 2.5% I_{Nap} activated at 10 – 20 mV more negative than I_{Nat} and the sodium activation slowed by a factor 2, the chronaxie time increased to 535 μs. The present human nerve fibre model therefore included a 2.5% I_{Nap} in addition to a 97.5% I_{Nat}.

The persistent current was set to activate at 20 mV more negative than the transient current and the sodium activation was slowed down.

The ionic membrane currents in the present human nerve fibre model could therefore be described in terms of temperature-dependent sodium (g_{Na}), potassium (g_K) and leakage (g_L) ionic conductances, as well as ionic equilibrium potentials

$$\begin{aligned} I_{ion}(T) = {} & 0.975 g_{Na}^{max}(T)\, m_t^3 h\,(V - V_{Na}(T)) + g_K^{max}(T)\, n^4\,(V - V_K(T)) \\ & + 0.025 g_{Na}^{max}(T)\, m_p^3 h\,(V - V_{Na}(T)) + g_L(T)\,(V - V_L(T)) \qquad \left[\mu A/cm^2\right]. \end{aligned} \tag{4.2}$$

Ionic currents are considered ohmic and are given in terms of the ionic conductances and change in membrane potential. Ion channel activation and inactivation probability dynamics (m_t, m_p, h and n respectively) were described by

$$\frac{dx}{dt} = \alpha_x(V)\,[1 - x] - \beta_x(V)\,x, \quad x = m, n, h \tag{4.3}$$

with initial values $m_t(0) = m_p(0) = 0.5$, $h(0) = 0.6$, $n(0) = 0.32$, and given in terms of the voltage-dependent opening and closing rates of the ion channels $\alpha(V)$ and $\beta(V)$

$$\alpha_{mt}, \alpha_{ns} = AQ_{10}^{(T-T_0)/10} \cdot \frac{B - CV}{D\,(\exp(B - CV)) - 1} \qquad [m/s], \tag{4.4a}$$

$$\beta_{mt}, \beta_{ns}, \alpha_h = AQ_{10}^{(T-T_0)/10} \cdot B \exp\left(\frac{-V}{C}\right) \qquad [m/s], \tag{4.4b}$$

$$\beta_h = AQ_{10}^{(T-T_0)/10} \cdot \frac{1}{(1 + \exp(B - CV))} \qquad [m/s], \tag{4.4c}$$

$$\alpha_{mp} = AQ_{10}^{(T-T_0)/10} \cdot \frac{B - C(V - \Delta V)}{D\,(\exp(B - C(V - \Delta V))) - 1} \qquad [m/s], \tag{4.4d}$$

$$\beta_{mp} = AQ_{10}^{(T-T_0)/10} \cdot B \exp\left(\frac{-(V - \Delta V)}{C}\right) \qquad [m/s], \tag{4.4e}$$

where ΔV indicates that the persistent sodium current activated 20 mV more negative than the transient sodium current. Acceleration of the activation and inactivation of the membrane's permeability to specific ion species, as suggested by Huxley (1959), is given by parameter **A** values (Table 4.1). In accordance with Bostock and Rothwell (1997), activation of the sodium permeability of I_{Nap} was slowed down by a factor 2.2. Parameters **B**, **C** and **D** are the original HH model parameters, which are considered constant (Hodgkin and Huxley, 1952).

Table 4.1: Parameters used for calculation of the voltage-dependent opening and closing rates of the ion channels. The transient sodium current activation parameters are subscripted with a t and the persistent sodium current activation parameters by a p.

Parameter	**Q_{10}**	**T_0 (°C)**	**A**	**B**	**C**	**D**
α_{mt}	2.16	20	4.42	2.5	0.1	1
β_{mt}	2.16	20	4.42	4.0	18	–
α_h	1.5	20	1.47	0.07	20	–
β_h	1.5	20	1.47	3.0	0.1	–
α_{ns}	1.5	20	0.20	1.0	0.1	10
β_{ns}	1.5	20	0.20	0.125	80	–
α_{mp}	1.99	20	2.06	2.5	0.1	1
β_{mp}	1.99	20	2.06	4.0	18	–

The equilibrium potentials were given in terms of the Nernst potential equations for the different ion species (Hille, 2001)

$$V_{Na}, V_K, V_L = \frac{1000RT_K}{F} \ln\left(\frac{[ion]_o}{[ion]_i}\right) - V_{rest} \qquad [mV]\,, \tag{4.5}$$

with R the universal gas constant, F the Faraday constant, T_K the absolute temperature (in Kelvin) and $[ion]_o/[ion]_i$ the extracellular to intracellular ion concentration ratio for Na^+, K^+ and leakage ions respectively (Table 4.2).

In an additional modification to the original Rattay cable model the myelinated internodes were considered to be simple double cable structures as modelled by Blight (1985). The leaky myelin sheath and axolemma were combined together in series, having high resistance and low capacitance. The internodal capacitance (c_{int}) was given by

$$c_{int} = \left(\frac{1}{c_{mem}} + \frac{N_{my}}{c_{my}}\right)^{-1} \qquad \left[\mu F/cm^2\right], \tag{4.6}$$

with c_{mem} the same value as the nodal membrane capacitance and c_{my} the myelin membrane capacitance (Table 4.2). The number of myelin layers (N_{my}) was given by

$$N_{my} = \lfloor 0.5\,(d_f - d_a)\rfloor / l_{my}, \tag{4.7}$$

with d_f the total internodal nerve fibre diameter (cm), d_a the internodal axolemmal diameter (cm) and l_{my} the myelin layer thickness equal to 0.016 μm (Blight, 1985).

Table 4.2: Model electrical parameters.

Parameter	**Value**	**Q_{10}**	**T_0 (°C)**	**Reference**
Membrane resting potential (V_{rest})	-79.4 mV	1.0356 (T $\leq$ 20 °C) 1.0345 (T > 20 °C)	6.3	Hodgkin and Huxley (1952), Schwarz *et al.* (1995), Wesselink *et al.* (1999) †
Gas constant (R)	8.3145 J/K.mol			Atkins (1995)
Faraday constant (F)	9.6485×10^4 C/mol			Atkins (1995)
$[Na^+]_o/[Na^+]_i$	7.2102			Hodgkin and Huxley (1952), Schwarz *et al.* (1995), Wesselink *et al.* (1999), Hille (2001) #
$[K^+]_o/[K^+]_i$	0.0361			Reid *et al.* (1993), Scholz *et al.* (1993), Schwarz *et al.* (1995)
$[Leakage]_o/[Leakage]_i$	0.036645			Scholz *et al.* (1993), Schwarz *et al.* (1995) ††
Na^+ conductance (g_{Na})	640.00 mS/cm^2	1.1	24	Scholz *et al.* (1993), Hille (2001)
K^+ conductance (g_K)	60.0 mS/cm^2	1.16	20	Reid *et al.* (1993), Scholz *et al.* (1993), Schwarz *et al.* (1995) ††
Leakage conductance (g_L)	57.5 mS/cm^2	1.418	24	Schwarz and Eikhof (1987), Scholz *et al.* (1993), Schwarz *et al.* (1995) ††
Axoplasmic resistivity (ρ_{ax})	0.025 kΩ.cm	$(1.35)^{-1}$	37	Wesselink *et al.* (1999) †
Membrane capacitance (c_{mem})	2.8 μF/cm^2			Schwarz *et al.* (1995) *
Myelin membrane capacitance (c_{my})	0.6 μF/cm^2			Blight (1985)
Membrane resistance (R_{mem})	4.8707×10^4 Ω.cm^2	$(1.3)^{-1}$	25	Blight (1985) †
Myelin membrane resistance (R_{my})	104 Ω.cm^2	$(1.3)^{-1}$	25	Blight (1985) †

† Value deduced from reference(s) and then optimised for model. Q_{10} value not from reference, but optimised for model

Discrepancy exists between HH model value and values for human. Value hence optimised for model

†† Values deduced from reference(s) and corrected for concentration and temperature differences

* Considered constant for temperatures between 20 and 42 °C

The internodal conductance (g_{int}) was given by

$$g_{int}(T) = \frac{1}{(N_{my} R_{my}(T)) + R_{mem}(T)} \qquad \left[mS/cm^2\right], \tag{4.8}$$

with R_{my} the temperature-dependent myelin membrane resistance and R_{mem} the temperature-dependent axolemmal membrane resistance (Table 4.2 and Blight, 1985). The assumption of a constant membrane conductance, in which the ionic membrane currents under the myelin sheath are ignored, renders the internodal current (I_{int}) constant (Rattay *et al.*, 2001b). I_{int} was therefore given by

$$I_{int}(T) = g_{int}(T)\, V \qquad \left[\mu A/cm^2\right]. \tag{4.9}$$

Similar to Wesselink *et al.* (1999) the electrical parameters of the nerve fibre cable model were recalculated as values per unit area and optimised for a fibre diameter of 15.0 μm. Electrical parameter values are listed in Table 4.2. The membrane capacitance ($C_{m,n}$) and axoplasmic resistance (R_n) of the nth compartment are defined in Equation 4.1. R_n is a function of the axoplasmic resistivity (ρ_{ax}) and the AP's conduction velocity (v_c) is influenced by ρ_{ax} (Moore *et al.*, 1978; Frijns *et al.*, 1994). Human peripheral sensory nerve fibres can be classified into groups according to conduction velocity and fibre diameter (Schalow, Zäch and Warzok, 1995). Schalow *et al.* (1995) determined v_c values of about 64.0 m.s^{-1} for fibres having a diameter of 15.0 μm and about 10.0 m.s^{-1} for 3.0 – 4.0 μm diameter fibres around 37 °C. Frijns *et al.* (1994) argued that although ρ_{ax} had not been reliably measured before, their model studies suggest a value of 0.07 kΩ.cm at 37 °C and a Q_{10} factor of $(1.3)^{-1}$. For the present human nerve fibre cable model a value of 0.025 kΩ.cm at 37 °C for ρ_{ax} and a corresponding Q_{10} factor of $(1.35)^{-1}$ were selected to give a v_c of 58.3 m.s^{-1} at 37 °C for the 15.0 μm diameter axonal fibre.

Wesselink *et al.* (1999) assumed a fibre diameter of 15.0 μm and a nodal area of 50 μm^2. This results in a nodal length of 1.061 μm, which falls well within the range of 0.88 – 1.25 μm for different nerve fibres (Chiu, Zhou, Zhang and Messing, 1999; Vabnick, Trimmer, Schwarz, Levinson, Risal and Shrager, 1999; Caldwell, Schaller, Lasher, Peles and Levinson, 2000; Waxman, 2000; Scherer and Arroyo, 2002). SEM photographs from these studies, as well as morphometric studies on human sensory nerve fibres (Behse, 1990), indicate that for internodes the axonal to fibre diameter ratio (g-ratio) varies from 0.57 to 0.7. On average smaller g-ratios are associated

with thinner fibres. It appeared that for fibres thicker than 0.34 μm the internodal axolemmal diameter (d_a) varied linearly with the fibre diameter (d_f)

$$d_a = 0.63 d_f - 3.4 \times 10^{-5} \quad [cm]\,. \tag{4.10}$$

The relationship between d_f and the internodal length (L_{int})

$$L_{int} = 7.9 \times 10^{-2} \ln\left(\frac{d_f}{3.4 \times 10^{-4}}\right) \quad [cm]\,, \tag{4.11}$$

however, was only valid for fibre diameters larger than 3.4 μm (Wesselink *et al.*, 1999). Also apparent from the same SEM photographs is the strangulation of the Ranvier node (Chiu *et al.*, 1999; Vabnick *et al.*, 1999; Caldwell *et al.*, 2000; Waxman, 2000; Scherer and Arroyo, 2002). Nodal diameter data from these SEM photographs were plotted against their corresponding d_f values, which ranged from 6.29 μm to 12.0 μm, and a curve fitted through the data points in Matlab. The best fit for the nodal diameter (d_{node}) was a third order polynomial

$$d_{node} = 8.502{\times}10^{5}\,(d_f)^3 - 1.376{\times}10^{3}\,(d_f)^2 + 8.202{\times}10^{-1} d_f - 3.622{\times}10^{-5} \quad [cm]\,, \tag{4.12}$$

and this was confirmed by fitting the curve in Sigmaplot using a different fitting procedure.

4.2.2 Model output calculations

All calculations were performed in Matlab. Differential equations were too stiff to be solved using the ode45 and ode23t numerical solvers, and hence the ode15s solver was used. Modelled nerve fibres ranged from 5.0 – 15.0 μm in diameter and were externally stimulated using a monopolar external electrode placed 1.0 cm from the nerve fibre central axis. The external environment was considered infinite, isotropic and homogeneous with an external resistivity (ρ_e) of 0.3 kΩ.cm at 37 °C (Frijns *et al.*, 1994). External stimulation was thus considered purely resistive and given by

$$V_e = \frac{\rho_e I_{stim}}{4\pi r_{dist}} \quad [mV]\,, \tag{4.13}$$

with r_{dist} the distance between the node and the electrode.

Action potential (AP) characteristics include amplitude, rise and fall times, strength-duration behaviour, refractory period and conduction velocity. Rise and fall times were calculated using the same method as described in Section 3.2.2, where the AP is approximated by a triangle, with the apex at the maximum amplitude (Frijns and ten Kate, 1994). The rising edge intersects the action potential curve at 10% of the maximum amplitude and the rise time is calculated as the time difference between this intersection point and the apex. The falling time is calculated in the same manner using the falling edge.

Strength-duration behaviour is characterised by the rheobase current and chronaxie time. Stimulation pulses were monophasic-anodic and ranged from 0.2 – 2.0 ms in duration. Even though the external stimulation was considered purely resistive, at temperatures lower than 30 °C the strength-duration curves for stimulation pulses up to 1.0 ms could not be fitted with the Weiss linear relationship (Weiss, 1901; Bostock, 1983; Wesselink *et al.*, 1999). Strength-duration curves were thus fitted with the exponential relationship of Lapicque (1907)

$$I_{th} = I_{rb} / \left(1 - e^{-t/\tau_{sd}}\right), \tag{4.14}$$

with I_{th} the threshold current (μA), t the pulse duration (μs), I_{rb} the rheobase current (μA) and τ_{sd} the strength-duration time constant (μs). The chronaxie time (τ_{ch}) is the strength-duration time constant at twice I_{rb}.

Absolute (ARP) and relative (RRP) refractory periods characterise nerve fibre refractory behaviour. Initial nerve fibre stimulation was effected with a 0.1 ms monophasic pulse with amplitude 20% above I_{th}. Stimulation with a second 0.1 ms monophasic pulse resulted in a second propagating AP. The absolute refractory period was defined as the maximum interval between the two pulses in which no second pulse, with amplitude of up to 400% I_{th}, could be elicited. The relative refractory period was the minimum interval between the two pulses in which an impulse of at most 101% I_{th} was required to elicit the second pulse (Wesselink *et al.*, 1999).

4.3 RESULTS

A general human peripheral sensory nerve fibre having diameters in the range of 5.0 – 15.0 μm was simulated in Matlab and externally stimulated with a monopolar electrode. Stimulation pulses were square, monophasic-anodic and only single pulses were used.

4.3.1 Action potential rise and fall times

AP rise and fall times were calculated in the temperature range of 20 – 37 °C. Figure 4.2 shows an example of a propagating AP for a 15.0 μm fibre calculated at 20 °C. Rise and fall times for a 15.0 μm fibre are compared to experimentally estimated results (Table 4.3). Rise times were less than 0.5% shorter than the estimated results at 20 and 25 °C, while being 4.2% shorter at 37 °C. The rise time decreased by 24.5% (Q_{10} factor of $(1.76)^{-1}$) from 20 to 25 °C.

Table 4.3: Simulated rise and fall times for a 15.0 μm diameter general human peripheral sensory nerve fibre cable model compared to experimentally estimated results from human peripheral nerve fibres.

Parameter	**Specifications**	**Value**		
	(15.0 μm fibre diameter)	**Human peripheral nerve fibre model**	**Experimental results**	**Reference**
Rise time (μs)	20 °C	269	270	Schwarz *et al.* (1995)
	25 °C	203	204	Schwarz *et al.* (1995)
	37 °C	115	120	Wesselink *et al.* (1999)
Fall time (μs)	20 °C	1840	1829	Schwarz *et al.* (1995)
	25 °C	1424	1464	Schwarz *et al.* (1995)
	37 °C	754	470	Wesselink *et al.* (1999)

Fall times were 6% longer at 20°C and 2.7% shorter at 25 °C than the estimated results, while being 60% longer at 37 °C. Compared to the results of the Ranvier node model (Section 3.3) the fall time decreased by 22.6% (Q_{10} factor of $(1.66)^{-1}$) from 20 to 25 °C, which was steeper than the 20% decrease of the experimental results. Calculated rise and fall times, and hence AP duration, varied with fibre diameter (Figure 4.3).

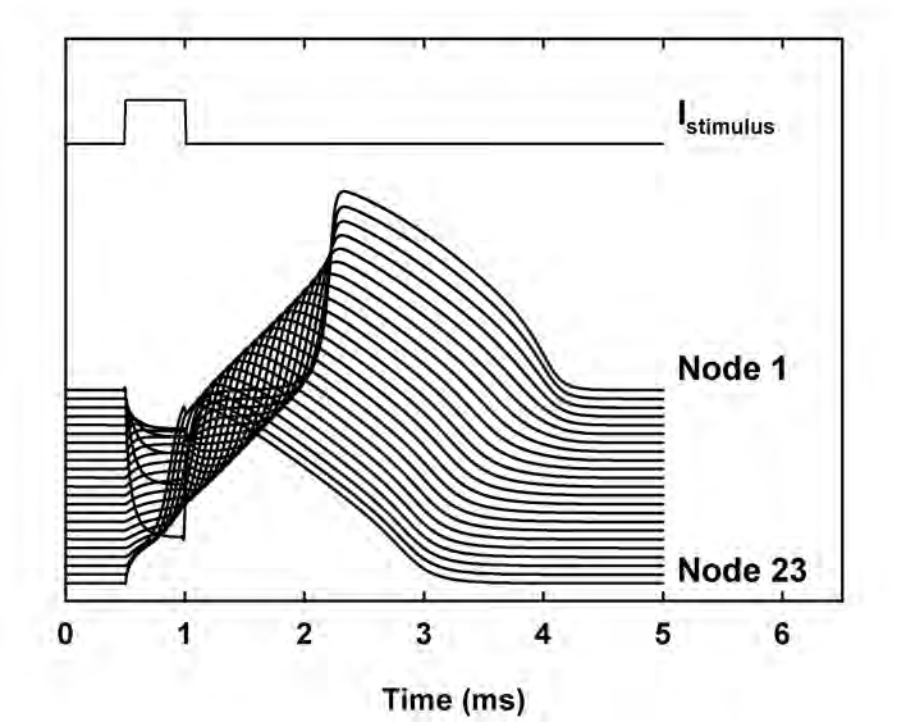

Figure 4.2: Propagating AP for a 15.0 μm fibre plotted at 20 °C. The fibre was externally stimulated with a monopolar electrode. The stimulating pulse was square, monophasic and anodic and 0.5 ms in duration. Only nodal APs are shown. Internodal APs were similar in nature than nodal APs.

In general, independent of temperature, rise times increased with a decrease in fibre diameter down to 7.5 μm (Figure 4.3(a)). However, below 7.5 μm rise times decreased again, with the rise time of a 5.0 μm diameter fibre similar to the rise time of a 12.5 μm diameter fibre.

Fall times decreased between 15.0 μm and 10.0 μm and then increased again for smaller fibre diameters, with the fall time of a 5.0 μm diameter fibre being similar to the fall time of a 15.0 μm diameter fibre (Figure 4.3(b)). The relationships between rise or fall times and fibre diameter became more pronounced as the temperature was decreased from body temperature. So, for example, the slopes of the fall time curve at 25 °C were more than twice as steep as the corresponding curve slopes at 37 °C (Figure 4.3(b)).

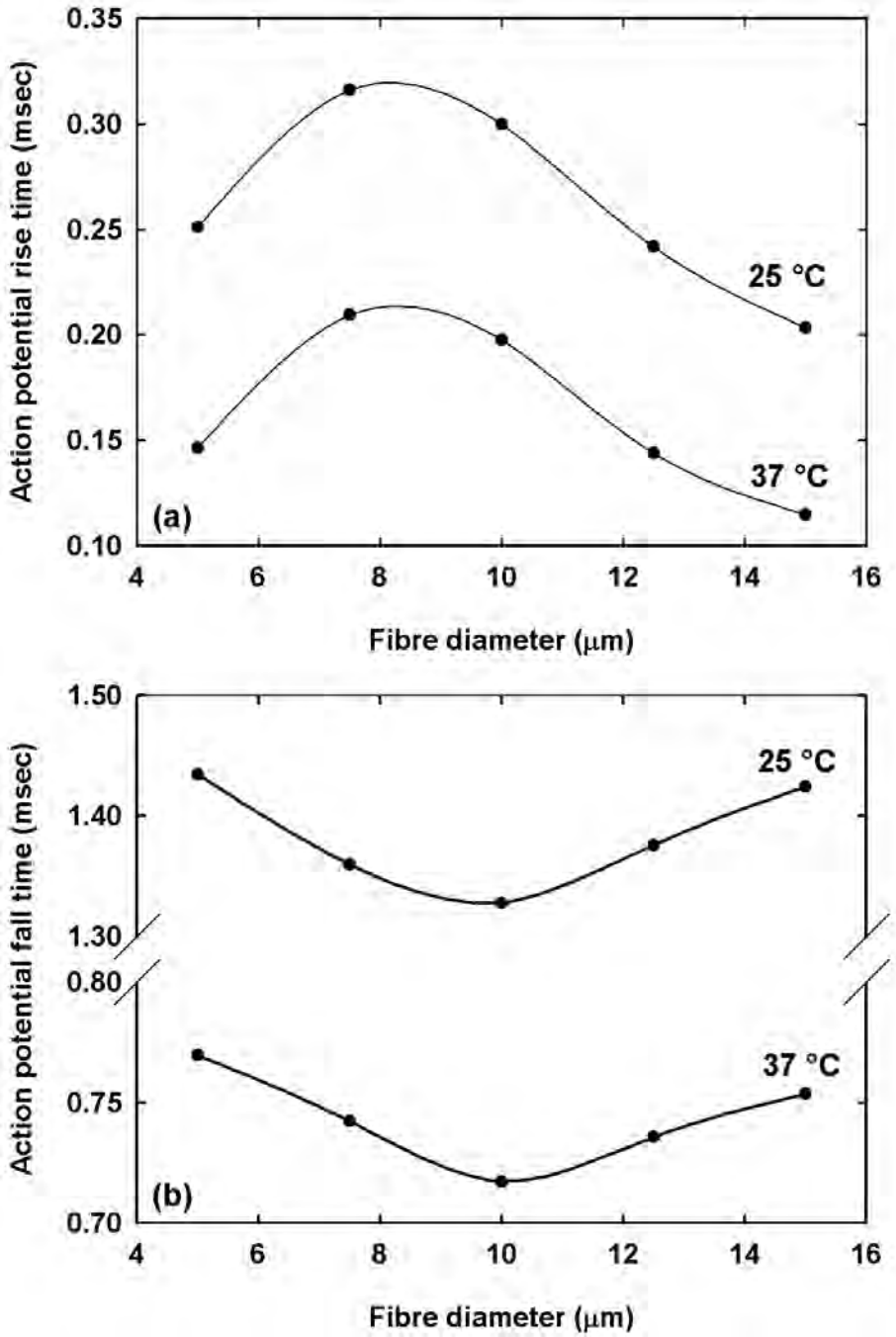

Figure 4.3: Relationship between AP rise and fall times and fibre diameter plotted at 25 °C and 37 °C. (a) AP rise times became longer with a decrease in temperature and increased with a decrease in fibre diameter down to 7.5 μm. (b) AP fall times were longer at lower temperatures compared to higher temperatures. Fall times decreased with a decrease in fibre diameter down to 10.0 μm and increased for thinner fibres.

4.3.2 Action potential duration times

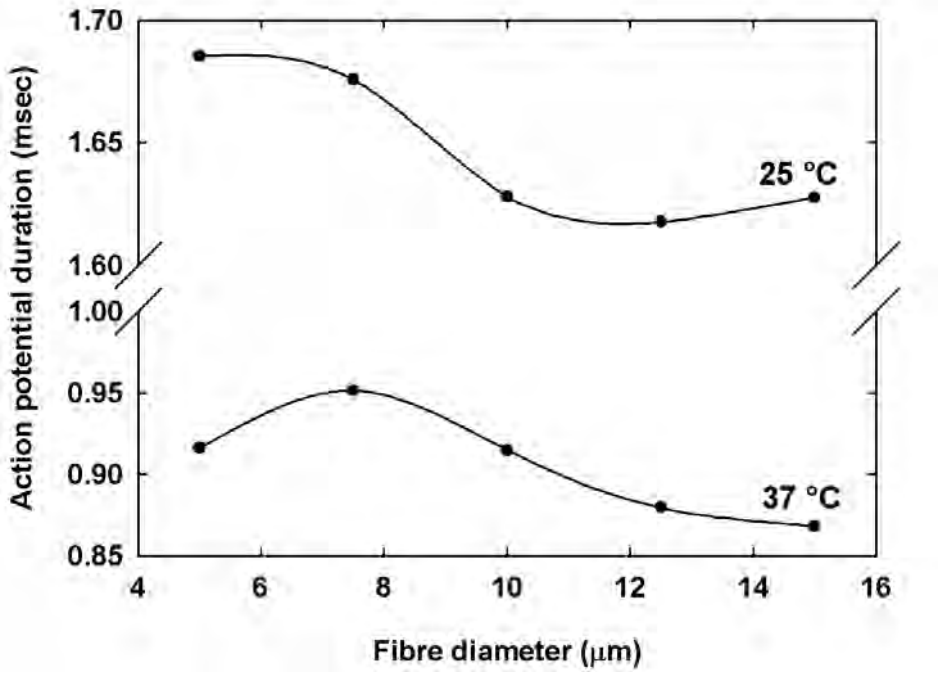

Figure 4.4: AP duration plotted against fibre diameter. For fibre diameters larger than 7.5 μm, AP duration showed an inverse relationship to fibre diameter at temperatures higher than 27 °C. At lower temperatures durations increased again for fibres larger than 12.5 μm.

The AP duration is the sum of the rise and fall times. AP duration, for fibre diameters larger than 7.5 μm, followed the trend of an inverse relationship to the fibre diameter (Paintal, 1966) at temperatures higher than 27 °C (Figure 4.4). At lower temperatures this relationship did not hold for fibre diameters larger than or equal to 12.5 μm.

Normalising these relationships to their respective values at 37 °C indicated a slightly steeper increase in AP duration in the thicker fibres with a decrease in temperature, compared to the thinner fibres; the average Q_{10} factor being about $(1.65)^{-1}$ (Figure 4.5). The curve of the 5.0 μm diameter fibre was similar to the 12.5 μm diameter curve and was thus omitted.

The change in slope around 27 °C for all fibre thicknesses is not apparent from Figure 4.5. For fibres thicker than 7.5 μm, the slopes increased by about 5.6% in the temperature range above 27 °C, compared to the less steep slope of about 3% in the

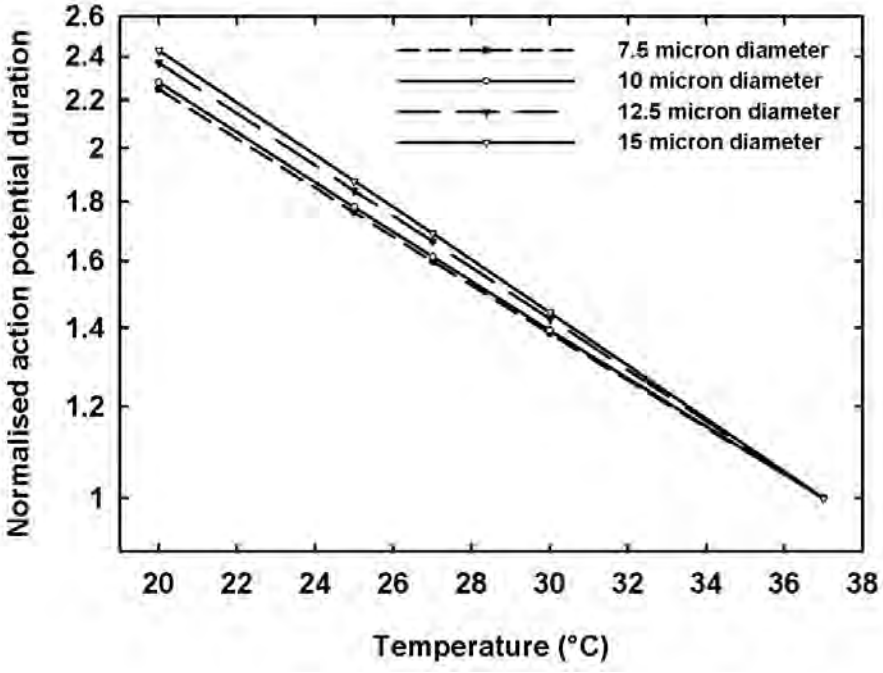

Figure 4.5: Temperature dependence of normalised AP durations plotted for fibre diameters larger than 7.5 μm. These results were obtained from curves similar to and including the curves in Figures 4.3 and 4.4. Results were normalised at AP durations at 37 °C. Curve slopes indicated a faster increase in AP duration for thicker fibres.

temperature range below 27 °C (Figure 4.6).

4.3.3 Action potential amplitude

Calculated amplitudes followed the trend of an amplitude decrease with temperature increase (Buchthal and Rosenfalck, 1966; Schwarz and Eikhof, 1987; Frijns *et al.*, 1994; Wesselink *et al.*, 1999). For the 15.0 μm fibre amplitudes around 115 mV were obtained at 20 and 25 °C and decreased by less than 1% between 20 and 25 °C. At 37 °C an amplitude around 112 mV was obtained. Amplitudes at corresponding temperatures decreased with a decrease in fibre diameter, but all amplitudes were larger than 100 mV. The exception to this trend again was the 5.0 μm fibre with amplitudes comparable to those of the 12.5 μm fibre.

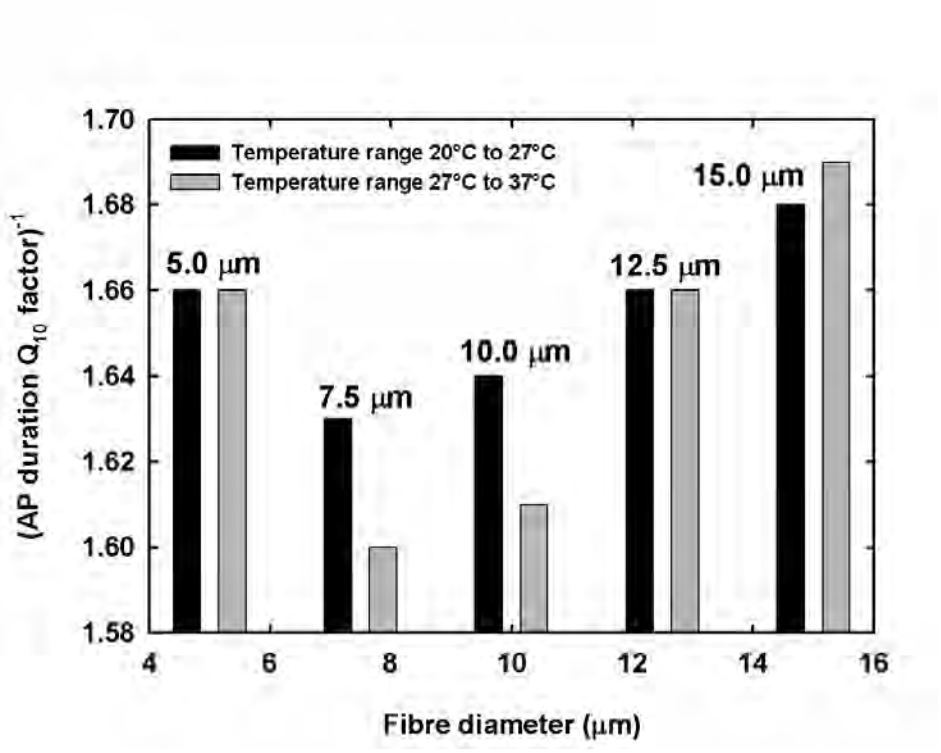

Figure 4.6: AP duration Q_{10} factors for temperature ranges 20 to 27 °C and 27 to 37 °C respectively, plotted against fibre diameter. Q_{10} factors were calculated from the curves in Figure 4.5. For fibre diameters larger than 7.5 μm, Q_{10} factors of the higher temperature range increased faster with a fibre diameter increase compared to the lower temperature range, indicating a change in AP duration slope in all fibres at 27 °C.

4.3.4 Conduction velocities

Conduction velocity (v_c) values of the new human nerve fibre cable model exhibited fibre diameter dependency (Figure 4.7), as well as temperature dependency (Table 4.4).

For fibre diameters thicker than 12.5 μm, v_c values compared well with the values measured by Schalow *et al.* (1995), but for thinner fibres v_c values were underestimated. Conduction velocities per diameter varied from 2.9 – 3.5 s^{-1} for fibre diameters ranging from 5.0 – 15.0 μm at 37 °C. Lowitzsch *et al.* (1977) measured average v_c values for human ulnar nerve sensory nerve fibres. Comparison to the data of Schalow *et al.* (1995) suggests an average ulnar fibre diameter of about 13.0 μm. Hence the v_c temperature dependency of a 13.0 μm simulated nerve fibre is compared to the results achieved by Lowitzsch *et al.* (1977) (Table 4.4). Simulated v_c values decreased with

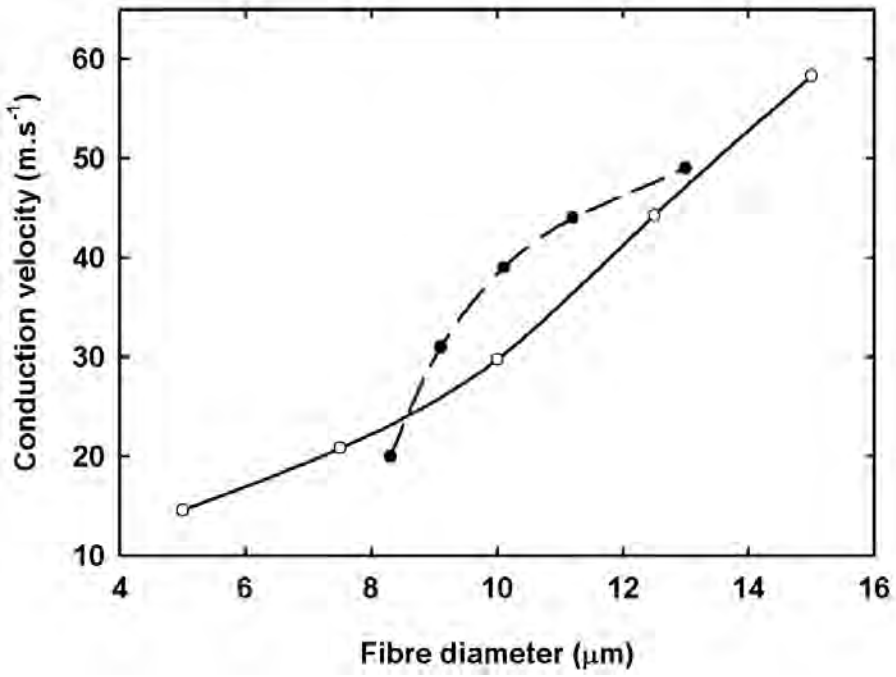

Figure 4.7: Conduction velocity plotted against fibre diameter (continuous line; open circles). Simulations were performed at 37 °C. Experimental data from Schalow *et al.* (1995) (dashed line; closed circles).

Table 4.4: Simulated temperature dependency of conduction velocity, ARP and RRP and chronaxie times for a general human peripheral sensory nerve fibre of about 13.0 μm diameter. Experimentally estimated results from Lowitzsch *et al.* (1977) are indicated in parenthesis for comparison.

Parameter	**Temperature (°C)**				**Q_{10} value**		**Reference**
	20	**25**	**30**	**35**	**30 – 20**	**35 – 25**	
Conduction velocity ($m.s^{-1}$)	28.81 (29.65)	36.52 (36.18)	42.35 (42.72)	46.20 (49.26)	1.47 (1.44)	1.27 (1.36)	Lowitzsch *et al.* (1977)
ARP (ms)	2.30 (3.07)	1.70 (1.72)	1.30 (1.02)	1.00 (0.54)	$(1.77)^{-1}$ $((3.01)^{-1})$	$(1.70)^{-1}$ $((3.18)^{-1})$	Lowitzsch *et al.* (1977)
RRP (ms)	20.40 (20.09)	10.30 (10.23)	5.10 (5.76)	3.16 (3.19)	$(4.00)^{-1}$ $((3.49)^{-1})$	$(3.23)^{-1}$ $((3.21)^{-1})$	Lowitzsch *et al.* (1977)
Chronaxie (μs)	737.4	439.9	245.1	138.4 (37 °C)	$(3.01)^{-1}$	$(2.62)^{-1}$	

increased temperature, but at a slower rate compared to real nerve fibre data. The maximum simulated value of 46.20 $m.s^{-1}$ at 35 °C was 6.2% lower than the experimentally measured value. Similar to the experimental results, the Q_{10} factors were different for the temperature ranges 20 – 30 °C (Q_{10} factor of 1.47) and 25 – 35 °C (Q_{10} factor of 1.27).

4.3.5 Refractory periods

ARP and RRP of the 13.0 μm simulated nerve fibre is compared to the results (Table 4.4) obtained by Lowitzsch *et al.* (1977). At body temperature (37 °C) the ARP was 0.9 ms and the RRP 3.05 ms. Both ARP and RRP decreased with an increase in temperature. Q_{10} factors indicated that the decrease was more pronounced in the lower temperature range of 20 – 30 °C than in the higher range of 25 – 35 °C, similar to the trend observed experimentally. For RRP the calculated rates overestimated the experimentally estimated rates by less than 15.0%. However, the calculated ARP results underestimated the experimental rates by more than 40%. Simulated ARP values did not vary significantly for fibres thicker than 10.0 μm, but increased by about 30% when the fibre diameter was decreased to 5.0 μm.

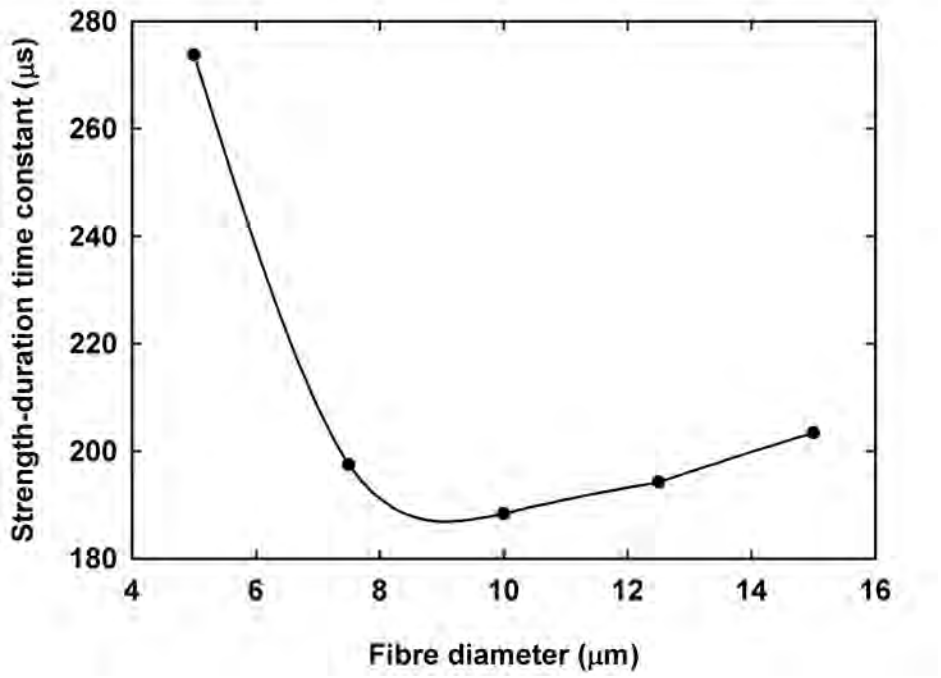

Figure 4.8: Strength-duration time constant plotted against fibre diameter. Simulation temperature was 37 °C.

4.3.6 Strength-duration relationships

Strength-duration curves were calculated for nerve fibres in the range of 5.0 – 15.0 μm. Stimulation was performed with a single monopolar external electrode placed 1.0 cm from the nerve fibre central axis. Stimulation pulses were monophasic-anodic and ranged from 0.2 – 2.0 ms in duration. The strength-duration time constant (τ_{sd}) showed nerve fibre diameter dependence (Figure 4.8), ranging from 184.3 μs to 273.6 μs at 37 °C over the studied nerve fibre diameter range. However, unlike the results obtained by Wesselink *et al.* (1999), τ_{sd} values did not decrease monotonically with increased fibre diameter, but increased again for fibre diameters larger than 10.0 μm. Chronaxie times (τ_{ch}) were about 30.5% lower than τ_{sd} values for all fibre diameters. Rheobase current was increased by 51.0% by increasing the fibre diameter from 5.0 μm to 10.0 μm and decreased by 11.6% for a further diameter increase to 15.0 μm.

Strength-duration relationships were calculated at temperatures between 20 and 37 °C

with τ_{ch} values showing an inverse relation to temperature (Table 4.4). This relationship was non-linear, with a larger rate of increase in τ_{ch} values for the temperature range 20 – 30 °C (Q_{10} factor of $(3.01)^{-1}$) compared to the range 25 – 37 °C (Q_{10} factor of $(2.62)^{-1}$), as calculated for a fibre of diameter 13.0 μm. The same trend was evident for the other fibre diameters as well.

4.4 DISCUSSION

In this chapter a new generalised human peripheral sensory nerve fibre cable model was developed. The nerve fibre model was based on the cable model by Rattay *et al.* (2001b), but modified to a simple double cable structure based on the model of Blight (1985). Modelled Ranvier nodes utilised the human Ranvier node model dynamics described in Chapter 3. The temperature dependence of all parameters was included.

Single-cable nerve fibre models include a small fast potassium (I_{Kf}) current, but since the myelin is considered a near perfect insulator with high resistance, the modelled nodes have to set their own resting potential (see for example the human nerve fibre models by Schwarz *et al.*, 1995; Wesselink *et al.*, 1999). This is effected through the inclusion of a high conductance leakage current (I_L), mostly carried by K^+ (Baker, 2002). In this human nerve fibre model the extracellular to intracellular ion concentration ratios for the I_L and I_K currents were similar, suggesting that I_L was mostly carried by K^+ (see the discussion in Section 3.4). However, in this model the myelin was not considered a near perfect insulator, resulting in smaller g_L values than the values used in the existing human nerve fibre models.

Paintal (1966) demonstrated an inverse relationship between AP duration and conduction velocity in cat sensory nerve fibres. AP duration also varies inversely with temperature in both slow and fast conducting fibres, although the slopes of these curves change at 27 °C. In slow conduction fibres the slopes are almost the same for the temperature ranges below and above 27 °C respectively, having Q_{10} factors around $(3.1)^{-1}$ below 27 °C and $(3.4)^{-1}$ above 27 °C (refer to Figure 4 in Paintal, 1966). The slopes for fast and slow conducting fibres are almost the same for temperatures above 27 °C. However, for temperatures below 27 °C, the slopes become levelled off in the faster fibres, having a Q_{10} factor of about $(2.27)^{-1}$ for a 64 m.s^{-1} fibre. This constitutes a

26.7% decrease in slope between slow and fast fibres.

In the human sensory nerve fibre model the inverse relationship between AP duration and fibre thickness, i.e. conduction velocity, held for simulated fibres thicker than 7.5 μm. AP duration varied inversely with temperature, but with the average Q_{10} factor for the slopes only being only about $(1.65)^{-1}$, compared to the value of $(3.4)^{-1}$ for the results obtained by Paintal (1966). Similar to the results of Paintal (1966), the curve slopes changed around 27 °C, but became steeper instead of flatter (see Figure 4.6). However, when the increase in slope steepness with increased fibre thickness for the temperature range below 27 °C was compared with the slope steepness increase for the temperature range above 27 °C, the former increased by about 3.0% compared to the 5.3% of the latter. In the thicker fibres the overall slope also changed less than 1% between the two temperature ranges, compared to a change of about 1.8% in the thinner fibres. It therefore seemed that the modelled human nerve fibres displayed the same trend of levelled off slopes in thicker (i.e. faster) fibres for temperatures below 27 °C, albeit a factor 10 less than for fibres in the Paintal (1966) study.

Schalow *et al.* (1995) determined that the ratio of the conduction velocity (v_c) to fibre diameter in afferent sensory nerve fibres ranges between 2.5 μs^{-1} and 4.1 μs^{-1}. In the model by Wesselink *et al.* (1999), the ratio varies between 3.1 μs^{-1} and 4.3 μs^{-1} for fibre diameters in the range of 5.0 – 15.0 μm at 37 °C. In the present human sensory nerve fibre model the simulated conduction velocity to fibre diameter ratios compare favourably with these results. However, v_c values were underestimated compared to the results of Schalow *et al.* (1995) and Wesselink *et al.* (1999) and did not display the linear relation to fibre diameter as the results of Wesselink *et al.* (1999) did. An analysis of the sensitivity of the v_c to model parameters suggested that v_c values were most sensitive to the internodal length and, to a lesser degree, the axoplasmic resistivity (ρ_{ax}) (unpublished results). For the present human nerve fibre cable model the values for ρ_{ax} and corresponding Q_{10} factor were selected to give a v_c of 58.3 m.s^{-1} at 37 °C for the 15.0 μm diameter axonal fibre. However, the same analysis study suggested different ρ_{ax} values when the internodal length for the 15.0 μm diameter fibre was varied. This added an additional degree of freedom to the optimisation procedure and would have required optimisation not only for a 15.0 μm diameter fibre, but also for fibres of different diameters. Owing to the lack of sufficient parameter data for fibres other than the 15.0 μm diameter fibre, it was assumed that it would be feasible to use the same relationship between fibre diameter and internodal length as

Wesselink *et al.* (1999). This resulted in the present model having the same internodal lengths as the model of Wesselink *et al.* (1999), but with a smaller ρ_{ax} value. Hence this difference might account for the underestimated v_c values simulated for thinner nerve fibres.

The calculated ARP of about 0.9 ms at 37 °C was longer than the experimentally estimated range of 0.58 – 0.79 ms for humans (refer to Table 1 in Wesselink *et al.*, 1999). The relation between ARP and fibre diameter was similar to the findings of Paintal (1965), who found that in cat nerve fibres, ARP values in faster (i.e. thicker) fibres varied insignificantly, but they varied inversely to v_c in slower fibres. Calculated RRP of 3.05 ms compared favourably with experimental results of about 3.0 ms at 37 °C (Lowitzsch *et al.*, 1977; Wesselink *et al.*, 1999).

Strength-duration behaviour indicated fibre diameter dependency, but unlike the model of Wesselink *et al.* (1999), rheobase current, strength-duration time constants and hence also chronaxie times did not decrease monotonically with a fibre diameter increase. Chronaxie times where shorter than experimentally estimated times (refer to Table 1 in Wesselink *et al.*, 1999). However, it must be remembered that the experimental values were estimated from compound fibre data (see for example studies by Kiernan *et al.*, 2001; Burke *et al.*, 1999), in contrast to the single fibre data presented here. Even so the chronaxie times compared favourably with times ranging from 113 – 202 μs from the Wesselink *et al.* (1999) model.

Different experimental studies on the effect of temperature on the chronaxie times in human cutaneous afferent nerve fibres show that chronaxie times do not vary significantly with a change in temperature (Mogyoros, Kiernan and Burke, 1996; Burke *et al.*, 1999; Kiernan *et al.*, 2001). Simulated results from the new human nerve fibre model were in contrast to these findings, showing an increase of more than a factor 5 for a decrease in temperature from 37 to 20 °C (see Table 4.4). Bostock (1983) suggested that the linear relationship of Weiss (1901) best estimates chronaxie times in simulated myelinated nerve fibres. Mogyoros *et al.* (1996) confirmed this finding for experimentally estimated chronaxie times in compound fibre data. Strength-duration curves at temperatures below 30 °C for single human nerve fibres modelled in the present study could not be fitted with the Weiss relationship, and were hence fitted with the exponential relationship of Lapicque (1907). As the temperature was increased from 20 °C, exponential fitting became less accurate; suggesting that a hy-

perbolic fit might be more accurate. This difference in strength-duration behaviour with temperature was not observed in previous human nerve fibre studies (compare Wesselink *et al.*, 1999), and needs further in-depth investigation.

Parameter data used in the present human sensory nerve fibre model were determined from published data from various studies of human nerve fibres. As mentioned in Section 4.2, Frijns *et al.* (1994) argued that ρ_{ax} had not been reliably measured before. Wesselink *et al.* (1999) derived their fibre-diameter-to-internodal-length relation from published data by Behse (1990). The third order polynomial relationship between nodal diameter and fibre diameter was determined by curve fitting to data derived from SEM photographs. Even though the size estimation of myelinated peripheral nerve fibres is commonly performed in quantitative neuromorphology, Geuna, Tos, Guglielmone, Battiston and Giacobini-Robecchi (2001) cautioned that the different methodologies used in such studies may bias the results. Newer computer-automated measurement approaches are more efficient and have a higher accuracy than older manual methods (Geuna *et al.*, 2001). However, the data that were available to determine the model parameter values did come from older studies and parameter values might be different from the true values for *in vivo* nerve fibres. Since the strength-duration properties of a nerve fibre depend on nodal membrane properties (Bostock, 1983), such differences might account for the discrepancy found in chronaxie values; for both temperature and fibre diameter variations.

Furthermore, the temperature dependency of a large proportion of the parameters was effected through the use of Q_{10} factors, in view of a lack of temperature-dependent studies done on individual human nerve fibre parameters. The use of Q_{10} factors assumed a linear relation between the parameter values and temperature variation. Temperature dependency results from this study suggested the assumption of such linear relationships over the entire temperature range from 20 – 37 °C might not be valid.

Lastly, mention must be made of the differences observed in the thinner, especially the 5.0 μm, nerve fibres compared to the thicker nerve fibres. Part of these behaviour differences might be explained by the above-mentioned discussion. However, the membrane parameters of the general nerve fibre were, in accordance with the previous modelling work by Schwarz *et al.* (1995) and Wesselink *et al.* (1999), developed and optimised for a 15.0 μm fibre and then 'scaled down' to model thinner fibres. Para-

meters used in the human Ranvier node model were based on values determined from studies done on thicker sensory nerve fibres (Section 3.2) and these parameter values may be different in thinner fibres. So for example, the slow potassium current at the Ranvier node is mediated by different KCNQ channels (Taylor *et al.*, 1992; Devaux *et al.*, 2004; Schwarz *et al.*, 2006). Ranvier nodes in thinner fibres showed labelling for KCNQ2 and KCNQ3, while nodes in thicker fibres showed labelling only for KCNQ2 (Schwarz *et al.*, 2006).

4.5 CONCLUSION

The objective of this study was to determine if the recently developed human Ranvier node model, which is based on a modified version of the HH model, could predict the excitability behaviour in human peripheral sensory nerve fibres. Up to now the most physiologically and morphometrically correct nerve fibre models describing these behaviour in humans are based on the Goldman-Hodgkin-Katz (GHK) current and voltage equations (Schwarz *et al.*, 1995; Wesselink *et al.*, 1999). These equations are more complex than the HH model equations used in the present model and are used to replace the linear current-voltage relationships of the opening and closing of the sodium and potassium channels in the HH model with non-linear relationships found in vertebrate excitable cells (Hille, 2001). This study was the first to show that the HH model equations could successfully be modified to predict excitability behaviour in humans without using the GHK equations.

Furthermore, temperature dependence of all parameters over the temperature range of 20 to 37 °C was addressed. The human nodal model was incorporated into a simple double cable nerve fibre model and simulation predictions compared favourably with experimentally determined results. However, as in the case of the single human Ranvier node model, chronaxie times were overestimated at temperatures lower than body temperature. This can be attributed to shortcomings in the fitting procedure employed to determine the chronaxie times, the bias in measured parameter values due to the measuring methodologies used, as well as the possible incorrect assumption of linear parameter relationships to temperature variation. Further study in this regard is advised.

In the last phase of the development of the human ANF model this general sensory nerve fibre model will be incorporated into the existing ANF model by Rattay *et al.* (2001b). This will be the topic of the next chapter.

Chapter 5

TYPE I HUMAN AUDITORY NERVE FIBRE MODEL

A preliminary study of the results presented in this chapter was presented at:
South African Institute for Physics 52nd Annual Conference, University of The Witwatersrand, Johannesburg, July 3 - 6, 2007

Conference proceedings will be published in the South African Journal of Science:
Smit, J. E., Hanekom, T. and Hanekom, J. J. (2008) Predicting human auditory action potential characteristics through modification of the Hodgkin-Huxley equations, *accepted for publication*

5.1 INTRODUCTION

Even though the physical structure of human ANFs has been investigated (Nadol Jr, 1988; Nadol Jr, 1990; Nadol Jr *et al.*, 1990; Rosbe *et al.*, 1996; Zimmermann *et al.*, 1995; Glueckert *et al.*, 2005a; Glueckert *et al.*, 2005c), the properties and types of ionic membrane currents of spiral ganglion cells have been characterised in murine (Mo *et al.*, 2002; Reid *et al.*, 2004; Hossain *et al.*, 2005; Chen and Davis, 2006) and guinea-pig (Bakondi *et al.*, 2008), but not in human. It is therefore only possible to hypothesise that since the ANF is of the sensory type, the possibility exists that similar ionic membrane currents to those found in a peripheral sensory fibre might be present.

In this chapter the general human sensory nerve fibre model is incorporated into the

Rattay *et al.* (2001b) ANF model. The axonal morphological parameters are changed to a Type I peripheral ANF and the model coupled to a volume conduction model of the cochlea. The objective of this chapter is to determine if this modified model can predict the excitability behaviour of the human peripheral auditory system betterthan previous ANF models and hence if the abovementioned hypothesis holds.

5.2 MODEL AND METHODS

5.2.1 The auditory nerve fibre model

The Type I human ANF model was based on the ANF cable model by Rattay *et al.* (2001b), but with the axon replaced with the generalised human sensory nerve fibre model described in Chapter 4. The dendrite and axon are divided into cylindrical compartments, while the soma is assumed to be spherical (Rattay *et al.*, 2001b). The nerve fibre morphometry is shown in Figure 5.1. An additional modification to the ANF model was a shortening of the dendrite to fit the somal position of its counterpart in the volume conduction cochlear model. Two types of Type I spiral ganglion cells exist with somal diameters varying between 24.6 μm and 29.9 μm (Schuknecht, 1993; Rosbe *et al.*, 1996). A value of 27.0 μm was thus assumed in the model.

Nodes of Ranvier were unmyelinated active axolemmae with only the axonal nodes utilising the human Ranvier node model described in Chapter 3. The myelinated axonal internodes were simple double cable structures as modelled by Blight (1985) and described in Chapter 4. SEM photographs and measured data of human auditory myelinated large Type I nerve fibres indicated an average fibre diameter of about 3.35 μm across the range from basal to upper middle cochlear turns, and a 2.34 μm axonal diameter (Rosbe *et al.*, 1996; Glueckert *et al.*, 2005a). This gives a fibre-to-axon diameter ratio of 0.7, in agreement with values ranging from 0.63 – 0.8, depending on the fibre thickness (Behse, 1990). The relationship between fibre diameter and internodal length that was used in the model, however, was only valid for fibre diameters larger than 3.4 μm (Wesselink *et al.*, 1999). Since the largest diameter in the basal turn described in the Rosbe *et al.* (1996) study was 4.3 μm and the smallest in the upper middle turn 3.2 μm, the average, being 3.75 μm, was assumed in the ANF model.

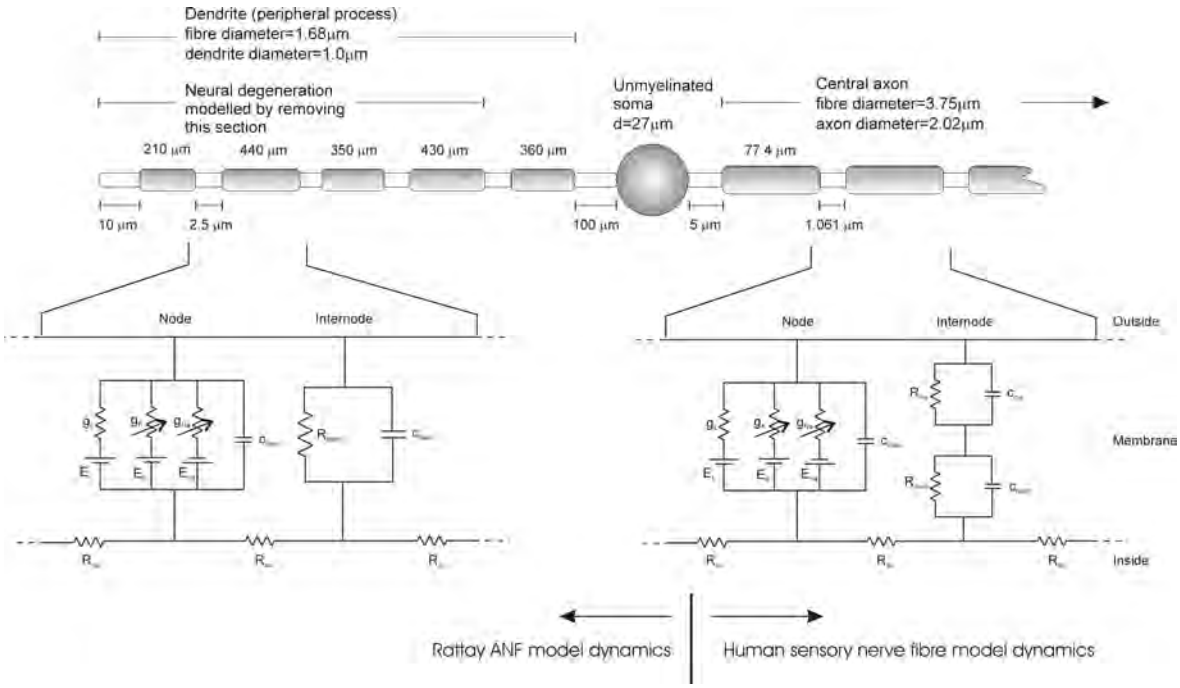

Figure 5.1: Representation of the human auditory nerve fibre. The dendrite is considered myelinated, with five internodes of variable lengths (Rattay *et al.*, 2001b). The myelin of these internodes is assumed a perfect insulator. The presomatic segment is divided into three sections (not indicated on sketch). Although the soma employs the Hodgkin-Huxley dynamics as described by Rattay *et al.* (2001b), its diameter is smaller than in the Rattay model. The axonal section employs the human sensory nerve fibre dynamics and morphometry and morphology. Unlike in the Rattay model, internodal lengths are considered constant and are shorter than in the Rattay model.

5.2.2 Modelling the degenerate nerve fibre

Retrograde neural degeneration, in which the dendrites are lost but the somas and axons survive, occurs in persons with profound sensory hearing loss (Nadol Jr, 1990; Schuknecht, 1993). The degree of retrograde neural degeneration depends on the severity of tissue alterations in the Organ of Corti during the original insult and concerns only Type I ANF's (Schuknecht, 1993).

Since not all ANFs are affected by retrograde degeneration, simulations were performed with three versions of the ANF model, simulating the effects of non-degenerated and increasingly degenerated nerve fibres respectively. A degenerate version of the ANF model, similar to Frijns, de Snoo and ten Kate (1996) and Briaire and Frijns (2006) was used to simulate the effect of neural degeneration, i.e. to simulate a nerve fibre with almost no peripheral process. This was effected by removing the first four nodal and internodal sections of the modelled ANF (refer to Figure 5.1). The first node in the degenerate version of the ANF model thus corresponded to node n_5 in Figure 5.2. An axon-only version was also modelled to simulate retrograde degeneration observed in long-term profoundly deaf persons (Schuknecht, 1993) by removing all dendritic nodes and internodes up to and including the soma in the ANF model.

5.2.3 The volume conduction cochlear model

The ANF model was coupled to a 3D spiralling finite element volume conduction model of the first one-and-a-half turns of the electrically stimulated human cochlea (Figure 5.2). For more details on the volume conduction model refer to Hanekom (2001b). Each of the nerve fibres present in the volume conduction model was described by the ANF model equations, where node n_1 in Figure 5.2 was the first node of the nerve fibre.

The cochlear model is designed to allow two possible electrode array positions, one medial and one lateral, relative to the modiolus. The Nucleus 24 straight array, which, after implantation, is positioned close to the outer wall of the cochlea (Miller, Abbas, Hay-McCutcheon, Robinson, Nourski and Jeng, 2004), is modelled with the lateral array, whereas the contour array, which lies close to the modiolus (Cohen *et al.*, 2003; Miller *et al.*, 2004) is modelled with the medial array. The straight array was

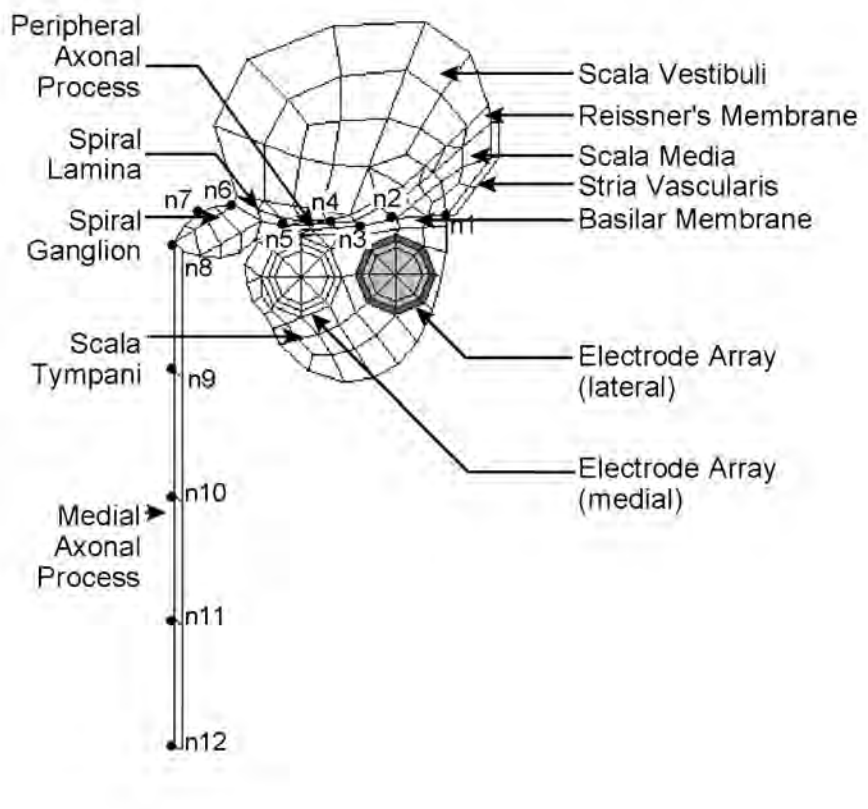

Figure 5.2: The two-dimensional finite element model geometry of a plane through the cochlea. The medial and lateral positions of the electrode array are shown as circular geometries towards the top of the scala tympani. The labels n_1 to n_{12} indicate the twelve locations (nodes) in the neural tissue where electrical potential values are calculated. (Figure used with permission from Hanekom, 2001b)

modelled with full-band electrodes and the contour array with half-band electrodes (Abbas and Miller, 2004; Miller *et al.*, 2004).

5.3 RESULTS

Simulations were performed in Matlab employing the same ODE solvers as discussed in previous chapters. Externally applied stimulation is incorporated through calculation of the external potential distribution inside the cochlea by the volume conduction cochlear model. The 3.75 μm diameter ANF fibre located in the basal cochlear turn was stimulated with a monopolar electrode configuration from either the con-

tour or straight electrode arrays at body temperature (37 °C). Stimulation pulses were square and monophasic-anodic. The computational methods used to calculate chronaxie time (τ_{ch}) values, as well as absolute (ARP) and relative refractory (RRP) periods have been described in Chapters 3 and 4. Results were compared for two classes of ANF fibres, i.e. a fibre containing only a transient sodium current (Na_t-fibre) and another fibre containing both a transient and a persistent sodium current (Na_p-fibre) at the axonal Ranvier nodes respectively. The results indicated that the Na_p-fibre best predicted Type I ANF excitation behaviour and hence only these results will be tabulated, while the results for the Na_t-fibre will only be discussed.

5.3.1 Strength-duration relationships

Chronaxie time (τ_{ch}) values were calculated for both fibre classes for stimulation with the contour and straight arrays respectively. In general τ_{ch} values decreased with a modelled increase in fibre degeneracy as shown in Table 5.1. Calculated τ_{ch} values for contour and straight arrays predicted about 10% higher values in the former case compared to the latter for non-degenerate and degenerate fibres, while values for the axon-only fibres were similar. For an axon-only fibre the Na_p-fibre had a τ_{ch} value of about 111 μs compared to a value of 86.1 μs for the Na_t-fibre, irrespective of the electrode array used. Values were also 50 – 60% higher for the Na_p-fibre compared to the Na_t-fibre.

Simulations predicted a rheobase current of 0.87 mA for a non-degenerate Na_p-fibre, 0.88 mA for a degenerate and 0.89 mA for an axon-only fibre when stimulated with the contour array. Rheobase current values for straight array stimulation were about twice higher compared to contour array stimulation. Corresponding values for a Na_t-fibre were about 10% lower for contour array and about 20% higher for straight array stimulation.

5.3.2 Refractory periods

Simulated ARP values for all versions of the Na_t-fibres and Na_p-fibres compared well to those of general sensory nerve fibres (Table 4.4), being 0.8 – 0.9 ms irrespective of the stimulation electrode array used (Table 5.1).

Table 5.1: Simulated characteristics of a human Type I ANF in the basal cochlear turn, using monopolar-monophasic stimulation for the Nucleus 24 straight and contour electrode arrays respectively. Values shown are for ANFs containing both a transient and a persistent sodium current at the axonal Ranvier nodes. Three versions of the ANF were modelled, indicating the degree of degeneracy of the ANF. All simulations were performed at 37 °C.

Parameter	**Specifications**	**Human ANF model (contour array)**	**Human ANF model (straight array)**
Chronaxie (μs)	Non-degenerate ANF	261.0	235.8
	Degenerate ANF	240.0	220.5
	Axon-only ANF	110.0	111.9
Conduction velocity (μs^{-1})	Non-degenerate ANF	2.09	2.15
	Degenerate ANF	2.05	1.95
	Axon-only ANF	6.54	5.15
ARP (ms)	All ANF versions	0.8	0.9
RRP (ms)	Non-degenerate ANF	4.6	4.5
	Degenerate ANF	4.4	4.1
	Axon-only ANF	4.3	4.2

Simulated RRP values differed, depending on the fibre used as well as the stimulation array used. Values for axon-only, degenerate and non-degenerate Na_p-fibres are listed in Table 5.1. For a non-degenerate fibre the RRP value was 11% longer compared to a degenerate fibre when stimulated with the straight array, and 6% longer when stimulated with the contour array, while values were about 3% longer for stimulation with the latter array compared to the former. For a Na_t-fibre contour array stimulation predicted about 5% longer RRP values compared to the straight array, while values were about 31% shorter compared to those for a Na_p-fibre. Values for a non-degenerate fibre were about 6% longer than for degenerate and axon-only fibres.

5.3.3 Conduction velocities

Conduction velocities and latencies were determined for monopolar stimulation with a monophasic pulse of 0.5 ms. Calculated conduction velocity (v_c) values for an axon-only Na_p-fibre were 24.5 m.s^{-1} (contour array) and 19.3 m.s^{-1} (straight array), and 12.8 m.s^{-1} (contour array) and 10.4 m.s^{-1} (straight array) for a Na_t-fibre compared to 9.0 m.s^{-1} for a similar general sensory nerve fibre stimulated externally. To aid comparison of v_c values between fibres of different diameter, it is customary to list

these values in terms of v_c values per fibre diameter (Wesselink *et al.*, 1999). Hence, for a Na_p-fibre, v_c values per fibre diameter are listed in Table 5.1. For a degenerate Na_p-fibre, v_c values were about 69% slower compared to stimulation of an axon-only fibre for contour array stimulation and about 62% slower for straight array stimulation. Non-degenerate Na_p-fibre v_c values were 2% faster compared to degenerate fibres for contour array stimulation and about 10% faster for straight array stimulation. Both non-degenerate and degenerate Na_t-fibre v_c values were similar to Na_p-fibre v_c values under the same stimulation conditions.

ANF performance is not measured in terms of v_c values and hence these values were translated into propagation times. AP propagation time is defined as the time taken by the AP to travel the length of the modelled ANF. Na_p-fibre AP propagation times for full, degenerate and axon-only fibres respectively were 0.41 ms, 0.23 ms and 0.05 ms for contour array stimulation and 0.40 ms, 0.24 ms and 0.065 ms for straight array stimulation. Propagation times for Na_t-fibres were 19% (non-degenerate), 32% (degenerate) and 257% (axon only) longer compared to Na_p-fibres for contour array stimulation. Corresponding propagation times for straight array stimulation were about 7% shorter than for contour array stimulation.

5.3.4 Mean latencies

Spike latency is defined as the time latency between stimulus onset and maximum AP amplitude, while mean latency is the mean of all the spike latencies measured for a specific stimulus intensity (Miller *et al.*, 1999b). In a deterministic model the mean latency would therefore compute to the spike latency. Mean latencies for an AP originating on the axon of a non-degenerate Na_p-fibre situated close to the stimulating electrodes in the basal cochlear turn for stimulation with the straight and contour array respectively are shown in Figure 5.3. Results for the degenerate case were similar to those of the non-degenerate fibre. Mean latencies decreased with an increase in stimulus intensity, ranging from about 0.48 ms at threshold intensity to about 0.24 – 0.25 ms at the maximum intensity calculated. In general stimulus intensities were lower for the contour array than for the straight array.

Mean latencies of APs originating on the dendrite of a fibre are shown in Figure 5.4 for non-degenerate and degenerate Na_p-fibres. All conditions were the same as for results

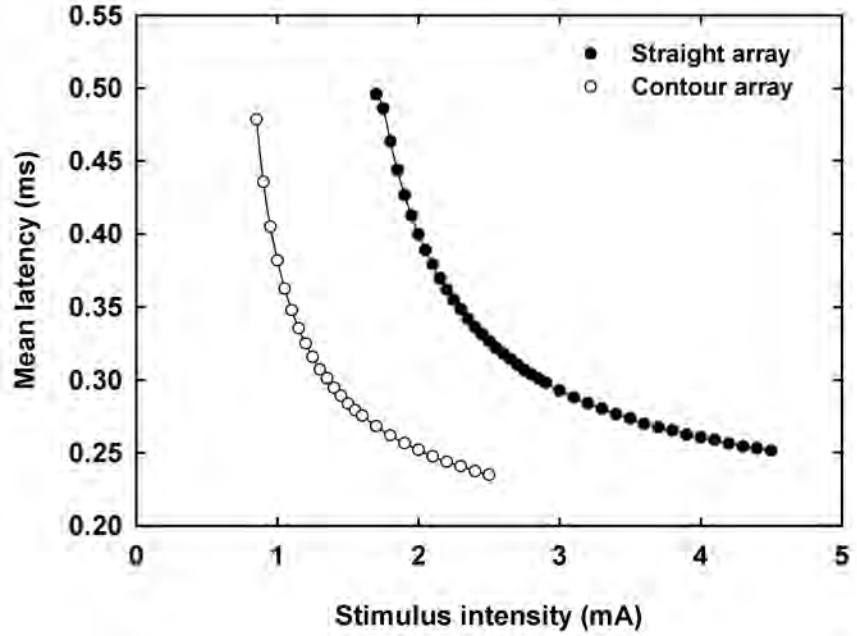

Figure 5.3: Calculated mean latencies for a non-degenerate Na_p-fibre stimulated with the straight and contour arrays respectively. The modelled fibre was situated close to the stimulating electrode in the basal turn. Open markers indicate results for contour array stimulation and closed markers results for straight array stimulation. Results for a degenerate fibre were similar to the non-degenerate case and are not shown.

shown in Figure 5.3. Mean latencies tended to decrease with an increase in retrograde degeneracy, ranging between 0.5 – 0.7 ms for a degenerate fibre compared to the range of 0.63 – 0.87 ms for a non-degenerate fibre. In contrast to the trend towards straight array stimulation, latencies calculated with contour array stimulation decreased to a minimum, after which they started to increase again, possibly suggesting a decrease in v_c with a stimulus intensity increase.

Double-peak evoked compound action potential (ECAP) responses have been observed in cats and humans (see for example studies by Van den Honert and Stypulkowski, 1984; Lai and Dillier, 2000). In these studies it has been suggested that the double positive peak response is indicative of the existence of surviving dendrites. The first positive peak (*P1*) originates from axonal excitation, while the second peak (*P2*) is due to dendritic excitation. The difference in latency between the two peaks can hence serve as an indication of propagation time across the soma. Similarly, the

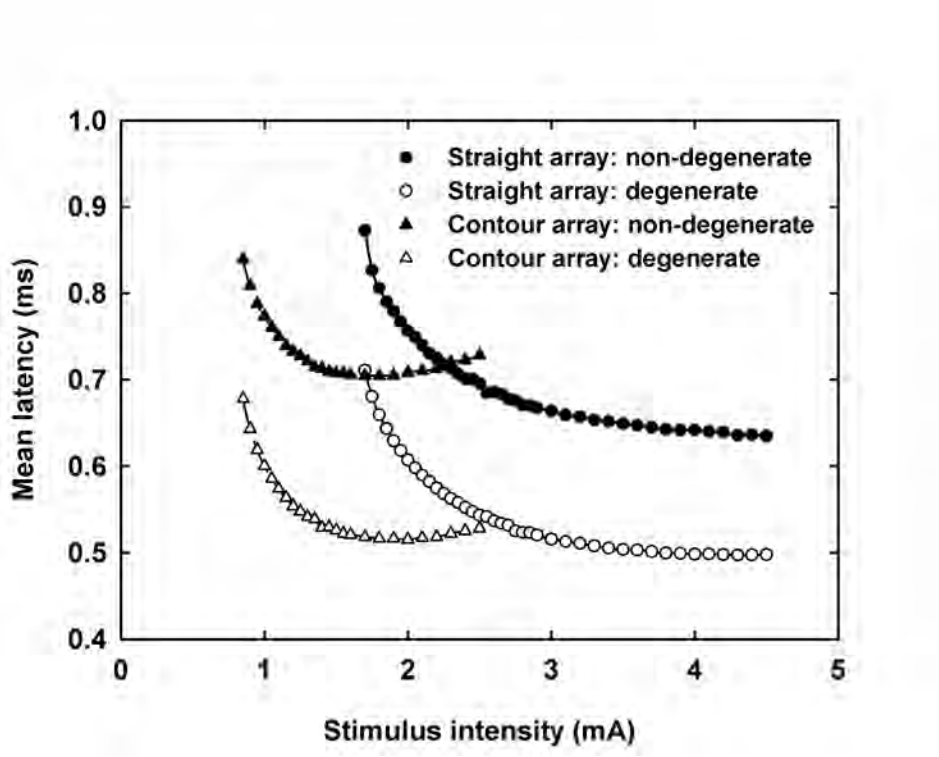

Figure 5.4: Mean latencies calculated for an AP originating from the dendritic process of non-degenerate and degenerate Na_p-fibres respectively. Fibres were situated in the basal cochlear turn close to the stimulating electrode of the straight and contour arrays respectively. Closed markers indicate non-degenerate fibre results and open markers the results for degenerate fibres. Results for straight array simulation are indicated with circles and solid lines, and contour array results with triangles and dashed lines.

propagation times across the soma can be calculated from the difference in latencies between Figures 5.3 and 5.4. Propagation times thus calculated for the contour array ranged between 0.361 and 0.493 ms for non-degenerate and 0.199 and 0.293 ms for degenerate ANFs. Propagation times calculated with the straight array were shorter compared to those of the contour array and ranged between 0.341 and 0.381 ms for non-degenerate and 0.192 and 0.238 ms for degenerate ANFs.

Results for the Na_t-fibre followed the same trends as for the Na_p-fibre. However, similar to the longer propagation times calculated for the Na_t-fibre compared to the Na_p-fibre, mean latencies where longer than for the Na_p-fibre, and are hence not shown.

5.4 DISCUSSION AND CONCLUSION

No experimental results exist regarding the fall and rise times, as well as the conduction velocity of the propagating action potential in ANFs. Instead, these fibres are classified in terms of temporal characteristics; including ARP and RRP properties, strength-duration behaviour and mean latencies (see for example a review by Abbas and Miller, 2004). All these characteristics depend, *inter alia*, on the type and strength of stimulation pulse, the electrode configuration and electrode-fibre distance (Abbas and Miller, 2004). In this study stimulation of the modelled cochlea was performed with two different Nucleus 24 electrode arrays in monopolar configuration, with the contour array positioned closer to the axonal part of the nerve fibres than the straight array. Stimulation pulses were square monophasic and anodic.

Stimulation in cochlear implants is typically in the form of pulse trains or continuous stimulation. The refractory properties of the neural membrane play an important role in the choice of stimulation used (Abbas and Miller, 2004). Firstly, it places a lower limit on the interphase / interpulse interval, raising the threshold stimulus intensity needed to elicit further responses during the RRP, and secondly, it places an upper limit on the stimulus rate used (Abbas and Miller, 2004). Mean ARP values between 0.33 ms (Miller *et al.*, 2001a) and 0.7 ms (Cartee *et al.*, 2000) and a mean recovery time constant of about 0.41 ms were estimated for cat auditory fibres (Miller *et al.*, 2001a) and an RRP of up to 5 ms (Cartee *et al.*, 2000; Abbas and Miller, 2004). ECAP studies on humans suggest an ARP value larger than 0.5 ms and a RRP value around 5 ms (Brown *et al.*, 1990). These measured human values are 44% shorter for the ARP and 15% – 23% longer for the RRP than the present model for a degenerate Na_p-fibre predicts, depending on the stimulation electrode array used. The Na_p-fibre also predicted the measured results better than the Na_t-fibre. It therefore seems that Type I ANF fibres may contain both transient and persistent sodium current components.

Although the somas and axons of the Type I ANF fibre degenerate at a slower rate than the dendrites, SEM studies of long-term profoundly deaf persons show a sharp decrease in the number of surviving fibres, compared to shorter term deaf persons (Schuknecht, 1993). Model predictions suggested that retrograde degeneration may not influence the ARP of ANFs, but this prediction has not previously been studied experimentally. The simulated RRP results for a non-degenerate fibre were longer than

for degenerate and axon-only fibres, possibly suggesting that longer-term deaf persons may benefit from implants employing faster stimulation rates than shorter-term deaf persons.

Latency measurements on normal hearing cats and cats in which the dendrites and somas were removed during a cochlear laminectomy showed a double-peak response in the normal hearing cats, while in the laminectomated cats only the first response peak appeared (Van den Honert and Stypulkowski, 1984). Van den Honert and Stypulkowski (1984) proposed that the former reflected peripheral dendritic excitation and that the shift in latency indicated a shift in excitation to a more centrally located site along the fibre. More recent ECAP studies on cats also suggested this proposition (Miller *et al.*, 1998; Miller *et al.*, 1999b; Miller *et al.*, 1999a; Miller *et al.*, 2001a). NRT measurements in human subjects implanted with the Nucleus 24 arrays also indicated the existence of similar response waveforms having either single positive or double positive peaks (Lai and Dillier, 2000). The NRT waveform is characterized by a negative (*N1*) peak, followed by the positive peak(s) (*P1* and *P2*). For a single positive peak waveform, the *N1* peak occurred around 0.3 – 0.4 ms and the *P1* peak around 0.6 – 0.7 ms. In the double positive peak responses, the *N1* peak occurred at times too short to measure with the NRT system (< 0.11 ms), while the *P1* and *P2* peaks occurred around 0.4 – 0.5 ms and 0.6 – 0.7 ms respectively. Calculated latencies for the single-peak case were hence ~ 0.3 ms. For the double-peak case it was ~ 0.4 ms and ~ 0.7 ms, while the resulting propagation times range between 0.2 and 0.3 ms. Lai and Dillier (2000) concluded that the double-peak response indicated the existence of almost intact ANF fibres, while the single-peak response might be due to retrograde degeneration. Latencies calculated for single fibres with the present human ANF Na_p-fibre model for degenerate fibres agreed well with these experimental human results. Predicted results were in agreement with the suggestion that longer latencies indicate the presence and dendritic stimulation of more intact ANFs, owing to the additional time it takes the AP to propagate along the fibre.

The strength-duration function gives the relationship between the threshold stimulus current necessary to excite a fibre and the stimulus duration. Strength-duration behaviour is characterised by the rheobase current and chronaxie time. Strength-duration curves measured for normal and damaged cat auditory nerve fibres show that for the damaged fibres, where only the axons are left intact, thresholds at short pulse durations are lower than for the normal fibres (Van den Honert and Stypulkowski, 1984).

This is most probably due to the fact that the damaged fibres are only excited in the axonal (central) part of the fibre, while for normal fibres excitation could occur either peripherally or centrally (Van den Honert and Stypulkowski, 1984). Simulations with the present model predicted higher rheobase values for axon-only fibres compared to degenerate and non-degenerate fibres. This can be attributed to the model itself. In Section 5.2 mention was made of the fact that the relationship between fibre diameter and internodal length that was used in the axonal part of the modelled fibre was only valid for fibre diameters larger than 3.4 μm. The dendritic diameter is only 1.0 μm, and hence the dendritic section of the fibre could not be replaced with the general sensory nerve fibre dynamics. Because of the difference in dynamics between the original Rattay *et al.* (2001b) model and the general sensory nerve fibre model, it is expected that the present ANF fibre model's excitation behaviour will differ from a model where the squid dynamics of the dendritic as well as the somal sections are also replaced with human dynamics.

Van den Honert and Stypulkowski (1984) also reported significantly shorter (118.0 μs versus 276.0 μs) chronaxie times for fibres of which the dendrites and somas were removed (leaving only the axons intact) compared to normal functioning fibres, indicating axonal excitation in the former. In both cases the fibres are electrically stimulated. Although the chronaxie time of about 111.0 μs for an axon-only simulated Na_p-fibre was much shorter compared to a similar general sensory human fibre, chronaxie times followed the trend of decreasing as the modelled fibre became progressively more degenerated.

According to Abbas and Miller (2004), chronaxie times depend on the electrode-axon distance. A closer separation may lead to a decrease of the strength-duration time constant and thus shorter chronaxies. The trend predicted by the present model was in contrast to the experimentally observed trend in that the chronaxie times for non-degenerate and degenerate fibres increased when the electrode-fibre distance was decreased, confirming the shortcoming in the model regarding dendritic modelling discussed previously.

In conclusion it therefore seems possible to modify the Hodgkin-Huxley equations to describe action potentials generated in the Ranvier node of a human sensory nerve fibre and apply these modification to create more realistic neural models of the electrically stimulated human auditory system. Comparison between predicted and experimentally

measured results of Type I ANF fibres also suggested the existence of similar sodium ionic membrane currents than present in general sensory nerve fibres. However, the squid-based dynamics of the dendritic and somal model sections need to be replaced with human dynamics to account fully for experimentally observed ANF excitation behaviour.

The next chapter takes a look at the development of a simple method to approximate the calculation of ECAPs. The output of the ANF model is a neural excitation profile at the location of the ANFs and is used as input to the method. ECAP profile widths at the location of the stimulating electrode array, as well as the estimated stimulus attenuation inside the cochlea can thus be determined.

Chapter 6

EVOKED COMPOUND ACTION POTENTIAL WIDTHS

The contents of this chapter is included in an article entitled:
Smit, J. E., Hanekom, T. and Hanekom, J. J. (2008) Estimation of stimulus attenuation in cochlear implants, *submitted for publication*

6.1 INTRODUCTION

The Type I ANF model described in Chapter 5 has to be verified against experimentally measured temporal characteristic data. This chapter and the next (Chapter 7) focus on applications of the ANF model to *a*) verify the model; and *b*) determine the model's applicability as part of larger models to address questions pertaining to the cochlear implant research field.

Most of the earlier temporal characteristic measurement studies centred on observations from single-fibres in cats and guinea-pigs, while more recent studies increasingly make use of gross ensemble observations through ECAP measurements. ECAP profile width data can be used to examine the extent to which psychophysical measurements reflect the amount of neural excitation spread (Cohen *et al.*, 2003; Miller *et al.*, 2003). The development of a comprehensive model to simulate ECAPs is beyond the scope of this study. However, ECAP profile widths can be used to estimate stimulus at-

tenuation. Stimulus attenuation (characterized by length constant) directly relates to current distribution and thus the extent of neural excitation inside the cochlea (Black and Clark, 1980; Spelman, Clopton and Pfingst, 1982; Black *et al.*, 1983; Kral *et al.*, 1998; Vanpoucke, Zarowski and Peeters, 2004).

This chapter focuses on the influence of the variation in the stimulus attenuation on neural excitation spread for monopolar stimulation of an electrode located in the basal part of the cochlea. The Type I ANF model was used to predict the width of neural excitation as a result of specific stimuli. The objective of this chapter is to develop a simple method to estimate stimulus attenuation values by calculating the values of stimulus attenuation that best fit the modelled excitation profile widths to the measured ECAP profile widths.

6.2 MODEL AND METHODS

6.2.1 Models of the implanted cochlea and auditory nerve fibre

Simulations were performed using the resistances from a 3D spiralling finite element volume-conduction model of the first one-and-a-half turns of the electrically stimulated human cochlea, coupled to the human ANF model (Figures 6.1(a) and (b)). The amplitudes of stimulation pulses at the nerve fibres were derived from the external potential distribution, which was in turn calculated from the Ohmic resistances from the volume-conduction model. Simulations were performed with two versions of the ANF model, simulating the effects of non-degenerate and degenerate nerve fibres respectively.

The modelled cochlea was stimulated with a monopolar electrode configuration, with the stimulated electrode located in the basal cochlear turn and the return electrode lying outside the cochlea. The pulsatile stimulus waveform was a biphasic, charge-balanced, square pulse without interphase gap, with equal cathodic and anodic phases of 40 μs duration. Only single-pulse responses were calculated.

Simulations were performed for two electrode array positions, one lateral (Nucleus 24

straight array) and one medial (Nucleus contour array), relative to the modiolus (Cohen *et al.*, 2003; Miller *et al.*, 2004). The straight array was modelled with full-band electrodes and the contour array with half-band electrodes (Miller *et al.*, 2004).

6.2.2 ECAP profile widths at the electrode array level

The output of the ANF model is a neural excitation profile (Figures 6.1(c) and 6.2), at the location of the ANFs (subsequently called neural level), showing the stimulus intensity at which a nerve fibre at a specific location along the length of the basilar membrane will be excited. To compare the predicted excitation widths and NRT results, the excitation widths, i.e. the ECAP profile widths, at the location of the stimulating electrode array (subsequently called electrode array level) need to be determined. Ideally, this will be done by solving the inverse problem, referred to as the "backward problem" (for details see Briaire and Frijns, 2005).

To facilitate estimation of the stimulus attenuation factor, a simple approximation to solving the inverse problem is used. The data of Cohen *et al.* (2003) provide ECAP response widths at various loudness levels, specified as percentages of the MCL. The position of the modelled probe electrode corresponded to Cohen *et al.*'s (2003) electrode 6 (i.e. a basal position). To model ECAP profile widths, the measured dynamic range data for electrode 6 of each of the seven Cohen *et al.* (2003) subjects were mapped onto the estimated neural excitation profiles. Mapping was performed by translating the dynamic range data to decibel values above threshold (defined at zero decibel) corresponding to the 20, 50 and 80% loudness levels for each subject. The estimated widths of the ECAP response at the neural level at these loudness levels were then read from the modelled neural excitation profiles (Figures 6.1(c) and 6.2).

A dimensionless, normalised potential step (value = 1 for activated nerve fibres, and zero elsewhere) was generated for each of these widths (Figure 6.1(d)) and used as the source in the calculation of potential field distributions at the electrode array level (Figure 6.1(e)). To perform these calculations, three simplifications with regard to real cochleae were made. Firstly, an isotropic medium was assumed in the space between the neural and electrode array levels, although an anisotropic medium was assumed in the volume-conduction cochlear model. Secondly, constant distances were assumed between the neural level and each of the respective electrode array levels.

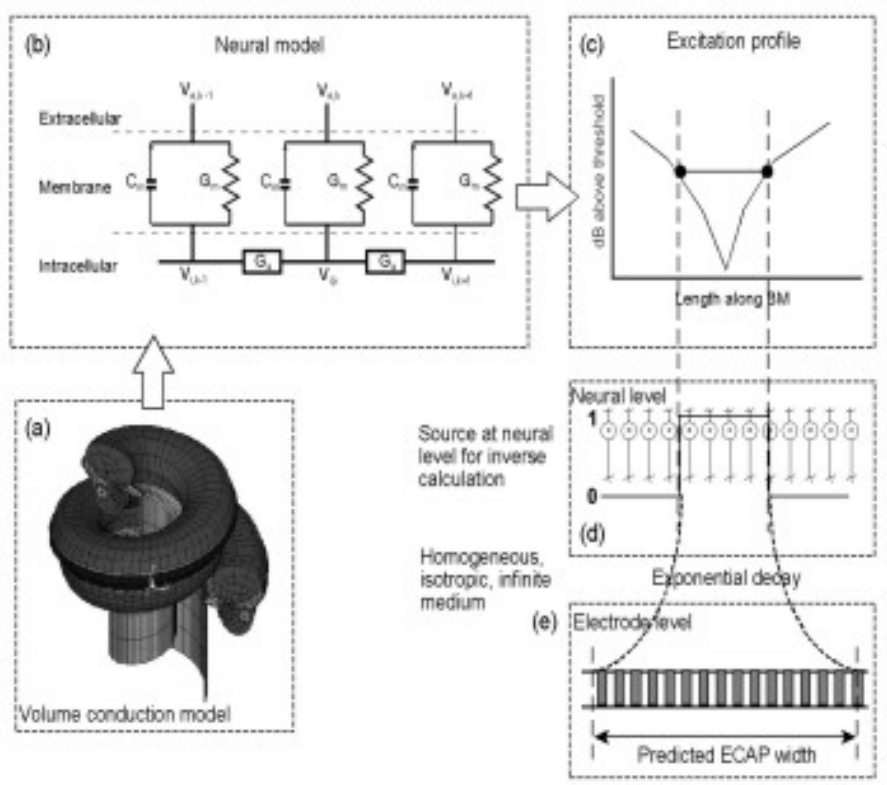

Figure 6.1: Outline of the simple method used to estimate ECAP profile widths at the electrode array level for non-degenerate and degenerate nerve fibres. Representations of the (a) volume-conductance cochlear model and (b) nerve fibre model. (c) The output of the ANF model is a neural excitation profile indicating the threshold currents at which the nerve fibres along the basilar membrane become excited. (d) Neural excitation spread is estimated at the neural level and e) the simple method estimates ECAP profile widths at the electrode array level.

Values for these distances were sourced from the volume-conduction model. Thirdly, a transverse exponential decay of voltage inside the scala tympani was assumed (Black and Clark, 1980; O'Leary, Black and Clark, 1985). Using an estimated value for the stimulus attenuation, each potential field distribution at the electrode array level was derived as the summation of the potential field contributions of all the activated ANFs as specified by the individual step functions. The full width half maximum (FWHM) of each distribution, i.e. the width of the potential distribution at 50% of its peak amplitude, determined the excitation widths, similar to the technique used by Cohen *et al.* (2003).

6.3 RESULTS

6.3.1 Neural excitation profiles

Neural excitation profiles were calculated with the ANF model (Figures 6.2(a) and (b)). For contour array stimulation profiles for degenerate nerve fibres predicted wider profiles, compared to straight array stimulation where the non-degenerate and degenerate nerve fibre populations predicted similar profile widths. Neural excitation profile widths were determined as discussed in Section 6.2.2.

Neural excitation profiles widths were also calculated with the GSEF model by Frijns and ten Kate (1994) and Frijns *et al.* (1995; 2000) in combination with the same volume-conduction model used in this study (Figures 6.2(c) and (d)). For details refer to Hanekom (2001b).

GSEF model neural excitation profiles differed from those of the ANF model. In contrast to the ANF model the GSEF model predicted similar neural excitation profiles, and hence profile widths, for degenerate and non-degenerate nerve fibre populations when stimulated with the contour array. For the straight array wider neural excitation profiles are predicted for a degenerate than a non-degenerate nerve fibre population.

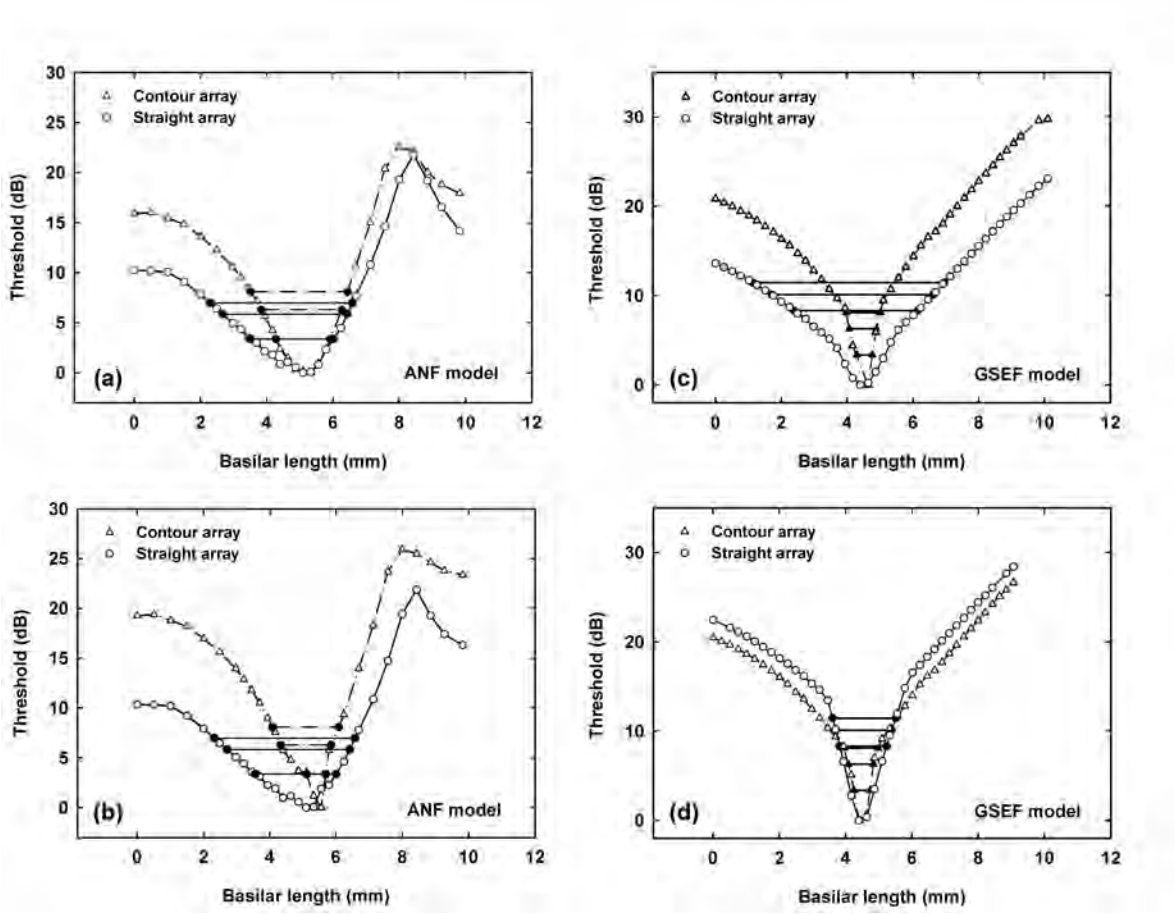

Figure 6.2: (a, b) Neural excitation profiles calculated with the volume-conduction-ANF model (open markers). Predicted neural excitation profile widths for 20, 50 and 80% loudness levels for Cohen *et al.*'s (2003) subjects S3 (straight array, solid lines) and C1 (contour array, dot-dash lines) for (a) a degenerate and (b) a non-degenerate ANF population are indicated with horizontal lines. (c, d) Neural excitation profiles simulated with the GSEF model combined with the volume-conduction model. All conditions are the same as in (a) and (b).

Table 6.1: Measured ECAP profile width ranges for electrode 6 (Cohen *et al.*, 2003) for four straight array and three contour array subjects. Width data at the 20% level were available for only one subject using the straight array, and for none of the subjects using the contour array. Profile widths were measured at FWHM, i.e. the profile width at 50% of the peak amplitude.

	80% loudness level	**50% loudness level**	**20% loudness level**
Straight array	4.26 mm to 6.78 mm	4.58 mm to 6.67 mm	3.73 mm (measured for single subject)
Contour array	2.98 mm to 3.41 mm	2.13 mm to 3.62 mm	No data available

6.3.2 Predicted versus measured ECAP profile widths

6.3.2.1 Measured ECAP profile widths

Cohen *et al.* (2003) reported the widths of the ECAP profiles at FWHM at 20, 50 and 80% loudness levels. The width ranges of seven subjects, four straight array and three contour array subjects, for probe electrode 6 are summarised in Table 6.1.

Width data at the 20% level were available for only one subject using the straight array, and for none of the subjects using the contour array. Cohen *et al.* (2003) observed that the profile widths of the contour array are narrower than those of the straight array.

6.3.2.2 Auditory nerve fibre model predicted ECAP profile widths

Predicted ECAP profile width results at the electrode array level for degenerate and non-degenerate ANF populations respectively, are shown in Table 6.2. A stimulus attenuation of 5.5 dB/mm was used in the simulations for goodness of fit to the Cohen *et al.* (2003) results. This value was within the range of stimulus attenuation values reported in literature (Black and Clark, 1980; Black *et al.*, 1983; Kral *et al.*, 1998) and was arrived at after consideration of the results presented in Table 6.3 and Figure 6.3(a) and (b). The width of the distribution was taken at FWHM.

The ECAP profile widths for both the straight and contour arrays followed the expected trend, i.e. to decrease with a decrease in loudness level. However, if the profile

Table 6.2: Simulated ECAP profile widths at the electrode array level for a stimulation attenuation of 5.5 dB/mm. Similar to Cohen *et al.* (2003) profile widths were measured at FWHM, i.e. the profile width at 50% of the peak amplitude.

	80% loudness level	**50% loudness level**	**20% loudness level**
Straight array: degenerate	3.88 mm to 6.76 mm	3.88 mm to 5.86 mm	3.65 mm to 5.29 mm
Contour array: degenerate	3.67 mm to 3.82 mm	3.31 mm to 3.67 mm	3.15 mm
Straight array: non-degenerate	3.48 mm to 6.64 mm	3.48 mm to 5.39 mm	2.92 mm to 5.09 mm
Contour array: non-degenerate	3.44 mm to 3.57 mm	3.21 mm to 3.44 mm	3.02 mm

width ranges between the two arrays were compared, the difference in width at the electrode array level was smaller compared to the difference observed at the neural level. The contour array also demonstrated narrower profile width ranges than the straight array. Furthermore, the profile width values for the contour array lay closer to the lower limit of the value range for the straight array.

Comparison between the degenerate and non-degenerate cases for the straight array predicted similar width ranges, with the degenerate case slightly wider than the non-degenerate case. For the contour array the width ranges for the degenerate case were wider than for the non-degenerate case. The reason for these differences is that at the neural level, the neural excitation profiles for the degenerate and non-degenerate cases were similar, while for the contour array there was a marked difference between the two cases.

6.3.2.3 Normalised ECAP profile width ranges

Figures 6.3(a) and (b) shows the simulated ECAP profile width ranges calculated with the ANF model, normalised to the width ranges measured by Cohen *et al.* (2003). Normalisation was done by dividing measured values by predicted widths. The ECAP profile widths for the straight array generally compared well for both degenerate and non-degenerate ANF cases, with the measured ranges at the 80% level reasonably centred on the predicted ranges, although the upper limits were underestimated by up to 48%. For the 50% levels the width ranges were underestimated, but were within

53% of the upper limits of the measured ranges. Cohen *et al.* (2003) measured the ECAP profile width for only one straight array subject at the 20% level, and the predicted value overestimated the measured valued by about 30%.

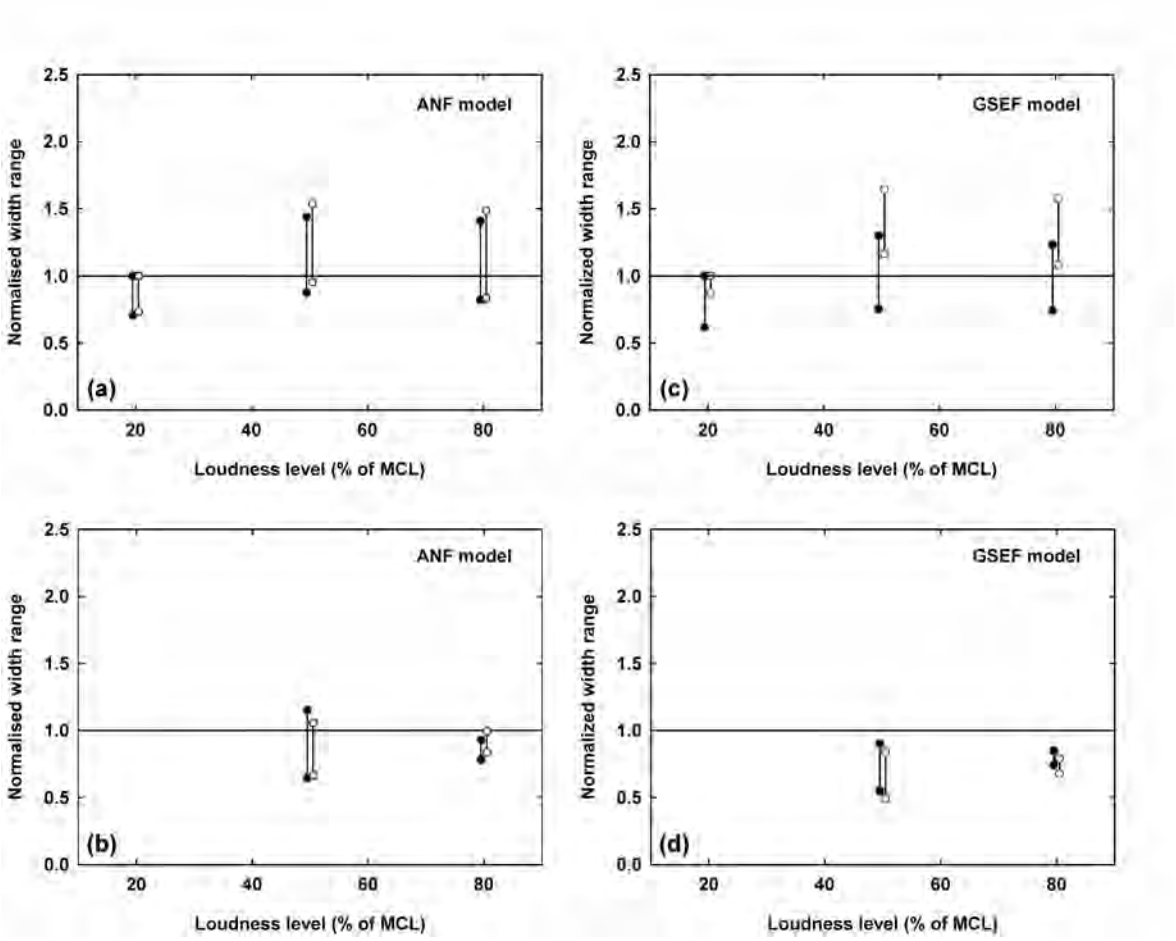

Figure 6.3: Normalised ECAP profile width ranges, at the electrode array level, calculated with the ANF model for 20, 50 and 80% loudness levels for (a) straight array and (b) contour array for a degenerate and non-degenerate ANF population. Calculations are for a stimulus attenuation of 5.5 dB/mm. Filled symbols indicates degenerate and open symbols non-degenerate ANF cases respectively. The horizontal line indicates the predicted widths. (c, d) Normalised ECAP profile width ranges calculated with the GSEF model. ECAP profile widths shown are for a stimulus attenuation of 3.5 dB/mm. All conditions are the same as in (a) and (b).

Width ranges at the 80% level were overestimated for the contour array, but the upper limits of the measured ranges were within 22% of the predicted ranges. The upper limits of the measured values at the 50% level were overestimated up to 36%

by the predicted values, while the lower limits fell within 15% underestimation by the predicted values.

Normalised ECAP width ranges calculate with the GSEF model for straight and contour arrays for degenerate and non-degenerate nerve fibre populations are shown in Figures 6.3(c) and (d). Normalisation was done in the same way as for Figures 6.3(a) and (b). The best fit to the Cohen *et al.* (2003) results was for a stimulus attenuation of 3.5 dB/mm. The contour array demonstrated narrower profile width ranges than the straight array. The profile width ranges between the two arrays for the non-degenerate case were also similar, in contrast to the larger differences observed for the degenerate case (compare with Figures 6.2(c) and (d)). Furthermore, the profile width values for the contour array lie closer to the upper limit of the value range for the straight array. The reasons for these differences lay in the way the two cases were modelled, with resultant similar potential step functions for the non-degenerate case resulting in similar neural response potential distributions.

6.3.3 Stimulus attenuation predicted with the auditory nerve fibre model

To exemplify the effect of stimulus attenuation on ECAP profile widths, the latter (for Cohen's subject S3) are shown as a function of stimulus attenuation at the electrode array level (Figure 6.4). Results for the other subjects were similar and are not shown. The ECAP profile widths decreased with increasing stimulus attenuation and asymptotically approached zero for large values of the stimulus attenuation.

The stimulus attenuation values that provided the best fit to Cohen *et al.*'s (2003) results are presented in Table 6.3. Owing to lack of information about the 20% loudness level data for the contour array, no stimulus attenuation values could be estimated. It appeared as though i) stimulus attenuation was relatively unchanged between the 50 and 80% loudness levels but increased for the 20% level and ii) that intersubject variation in stimulus attenuation existed at a specific loudness level.

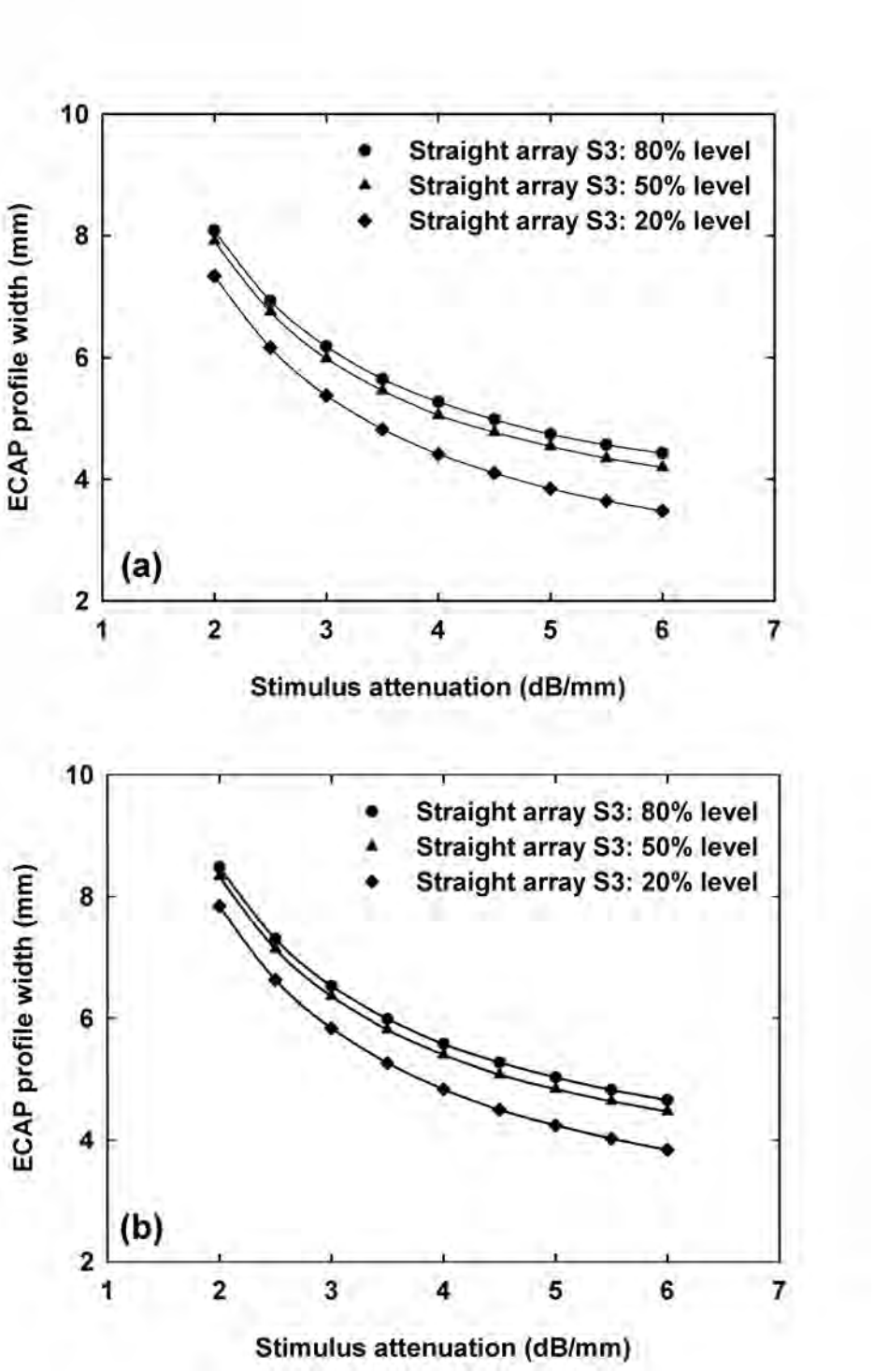

Figure 6.4: Predicted ECAP profile widths, at the electrode array level, for 20, 50 and 80% loudness levels for subject S3 (straight array) for (a) a degenerate and (b) a non-degenerate ANF population. The ECAP profile widths are plotted against stimulus attenuation.

Table 6.3: Stimulus attenuation values that provide the best fit of the modelled human ANF model data to the data of Cohen *et al.* (2003).

	80% loudness level	**50% loudness level**	**20% loudness level**
Straight array: degenerate	2.5 - 6.0 dB/mm	2.5 - 6.0 dB/mm	5.5 - 6.0 dB/mm
Contour array: degenerate	5.5 - 6.0 dB/mm	5.0 - 6.0 dB/mm	No data to compare with
Straight array: non-degenerate	2.5 - 6.0 dB/mm	2.5 - 6.0 dB/mm	4.0 - 4.5 dB/mm
Contour array: non-degenerate	5.5 - 6.0 dB/mm	5.0 - 6.0 dB/mm	No data to compare with

6.4 DISCUSSION

The modelled results for the human ANF model showed that, as the loudness levels (or stimulus intensity) increased, the ECAP profile width (i.e. neural excitation spread) increased. This agrees with the findings of Cohen *et al.* (2003) and Briaire and Frijns (2005). A comparison between the simulation results for the non-degenerate and degenerate nerve fibres showed more localised excitation spread for the contour array compared to the straight array. This is consistent with the observation that the straight array is located further away from the modiolus than the contour array, with a resultant wider potential field distribution, which causes a larger number of nerve fibres to be excited at a specific stimulus intensity relative to the threshold stimulus intensity, (e.g. Shepherd *et al.*, 1993; Cohen, Saunders and Clark, 2001; Frijns *et al.*, 2001; Cohen *et al.*, 2003).

The simulated neural response profile width data were sensitive to the value of the stimulus attenuation parameter chosen (see Figure 6.4 and Table 6.3). Larger parameter values predicted smaller spread of neural excitation. Also, a homogeneous, isotropic medium was assumed in the space between the neural and electrode array levels in the simple approximation method. This assumption is in contrast to an actual cochlea, where the conductivities of the different cochlear tissues vary significantly (see for example Frijns *et al.*, 1995). Since stimulus attenuation is a function of conductivity, predictions of neural excitation spread will be influenced by a non-homogeneous, anisotropic model of the space between the nerve fibres and the electrode array.

The observation that stimulus attenuation seemed to vary with stimulus intensity (Table 6.3) might be related to a more localised spread of excitation at lower stimulus intensities relative to that at higher stimulus intensities. Stimulus decay occurs in two directions: transversal (i.e. perpendicular to the electrode array) and longitudinal (i.e. in a direction parallel to the electrode array) because currents distribute in both directions throughout the cochlear tissue, as reported by Kral *et al.* (1998). It is possible that the weight that stimulus decay in each direction carries toward the determination of the neural excitation profiles is dependent on stimulus intensity. However, this hypothesis requires further investigation. Variations in cochlear structure and location of the electrode array inside the scala tympani could also lead to variations in the conductivity profile of the cochlear tissue between the array and the nerve fibres and could thus be responsible for observed intersubject variability in stimulus attenuation. A further observation is that the electrode-electrolyte interface impedance is a function of stimulus intensity (i.e., current density through the interface) (Ragheb and Geddes, 1990). The impedance of the electrode-electrolyte interface is disregarded in the volume-conduction model. In the model a current source is modelled instead of a potential source and the input current will be constant as long as the impedance of the electrode-electrolyte interface stays within required compliance limits. Hence the forward calculation problem does not dependent on the impedance. However, the data from Cohen *et al.* (2003), which are an integral part of the reverse calculation, include the effect of the interface impedance. Hence, the dependency of stimulus attenuation on stimulus intensity may partly be explained by the volume-conduction cochlear model characteristics, rather than the ANF model. Since the development of the volume-conduction model falls outside the scope of this study, these issues will be addressed in a follow-up study.

There was a marked difference in the stimulus attenuation parameter values between the GSEF and human ANF models that best predicted the experimental results. The value of 3.5 dB/mm predicted with the GSEF model was closer to the measured values of 0.54 – 1.09 dB/mm for monopolar stimulation in living cats performed by Black and Clark (1980) and Black *et al.* (1983), than the value of 5.5 dB/mm predicted with the human ANF model. However, the differences in cochlear structural morphology between animals and humans, differences in the number and percentage myelination of ANFs and innervation patterns of both inner and outer hair cells across species, may be physiologically significant and care must be taken when extrapolating the animal results to predict results in human implantees (Nadol Jr, 1988; Frijns *et al.*,

2001). Matsuoka *et al.* (2000b) also discussed the differences and similarities between animal and human data. In most animal studies, acutely deafened animals are used. Therefore, a larger relatively intact nerve fibre population is expected, in contrast to the more degenerative nerve fibre population of the longer-term deafened animal or human. Acutely deafened animal models can thus only give a best case scenario for the electrical excitation of the human ANF (Abbas and Miller, 2004). In many of the animal experiments, a single electrode is placed inside the cochlea (Van den Honert and Stypulkowski, 1984), while in humans multiple-electrode arrays are used. The anatomy of the animal and human nerve fibres also differs (Rattay *et al.*, 2001b; Briaire and Frijns, 2005). Thus, nerve fibre models based on animal physiology at this stage can only roughly approximate human ANF behaviour.

In general, ECAP profile widths calculated with the GSEF model (Figures 6.3(c) and (d)) were narrower than those calculated with the human ANF model (Figure 6.3(a) and (b)). Similar to the ANF model, the ECAP profile widths for both the straight and contour arrays decreased with a decrease in loudness level. The inclusion of non-homogeneous, anisotropic material properties in the inverse calculation of the ECAP profile widths could also improve the estimated value of the stimulus attenuation parameter and could relate this parameter to the specific location of the electrode array relative to the target nerve fibres. Individualised volume-conduction models that take the location of the electrode array relative to the target nerve fibres of a subject into account, could also improve the stimulus attenuation value estimate.

In spite of a number of shortcomings in the current model as discussed above, results suggested that matching predicted neural excitation profile widths to ECAP data by manipulation of the stimulus attenuation parameter could provide estimates of stimulus attenuation for specific subjects. An accurate estimate of stimulus attenuation could be useful in models that depend on stimulus attenuation to calculate excitation profiles (e.g. Bruce *et al.*, 1999c; Conning, 2006).

6.5 CONCLUSION

The human ANF model correctly predicts an increase in excitation spread with an increase in loudness level, as well as wider ECAP profile widths for the straight array

compared to those for the contour array. The model also predicted realistic ECAP profile width ranges for the straight array while the lower limit for the width ranges predicted for the contour electrode is comparable to measured width ranges.

It is observed that the fitting of modelled excitation profile widths to measured ECAP profile widths requires different stimulus attenuation values at different stimulation levels. Whether this actually indicates a shortcoming in the model is not certain since the impedance, which is related to stimulus attenuation, could be dependent on stimulus intensity. This observation thus suggests that the effects of stimulus intensity on the mechanisms of stimulus decay and on the electrode-electrolyte interface impedance require further investigation.

Chapter 7

INFLUENCE OF PULSATILE WAVEFORMS ON THRESHOLD PREDICTIONS

The contents of this chapter is included in an article entitled:
Smit, J. E., Hanekom, T., Hanekom, J. J., van Wieringen, A. and Wouters, J. (2008) Effects of pulseshape on threshold and comfortable level predictions from a human auditory nerve fibre model containing persistent sodium and slow potassium currents, *submitted for publication*

7.1 INTRODUCTION

Macherey *et al.* (2007) recently developed a dual-process integrator-resonator phenomenological model of the human auditory nerve. The model assumed a population of 10,000 nerve fibres divided into two classes with half the population integrator ANFs and the other half resonator ANFs. In general, nerve fibres can be divided into a number of types, not to be confused with the Type I and Type II ANFs discussed in Chapter 2. The Type I nerve fibres exhibit integrator behaviour and Type II nerve fibres resonator behaviour (Izhikevich, 2007). The HH model is a resonator (Type II) model (Izhikevich, 2007) and hence it cannot fully explain the non-monotonic trends in ANF behaviour (Macherey *et al.*, 2007). Macherey *et al.* (2007) suggested that the voltage-gated ion channel currents that may explain these non-monotonic trends

are either a hyperpolarisation-activated current (I_h) already observed in mammalian spiral ganglion cells (Chen, 1997), or a combination of a slow potassium current and persistent sodium current (see for example the motor nerve fibre model by McIntyre, Richardson and Grill, 2002).

The ANF model described in Chapter 5 contains both persistent sodium and slow potassium currents. In this chapter the possibility is investigated that the ANF model will be able to predict threshold changes observed for different pulsatile waveforms. The objectives of the chapter are *a*) to verify the model against results from previous experimental studies; *b*) to determine the model's suitability to predict temporal characteristics of the different waveforms; and *c*) to investigate whether the combination of persistent sodium and slow potassium currents are sufficient to explain the non-monotonic trends observed in ANF behaviour.

7.2 MODEL AND METHODS

7.2.1 Stimuli and stimulation conditions

Simulations in this chapter were performed for a degenerate ANF population only, except for waveform rate simulations where both non-degenerate and degenerate populations are considered. Monopolar stimulation was simulated on a basal turn electrode from the contour (medial) array. Stimuli were charge-balanced and both anodic-first and cathodic-first pulse-train stimuli were considered. Phase durations for the high-amplitude short-duration phases of different stimuli were 40 μs/phase, except where stated differently, while the low-amplitude long-durations phases were eight times longer. Owing to the computational intensiveness of the model, stimuli were presented for 12 ms. Pilot calculations for stimuli presented at 12, 25, 50 and 100 ms indicated a threshold difference of less than 5% between stimuli presentations of 12 and 100 ms.

Simulations were performed for different pulsatile waveforms shown in Figure 7.1. Results were compared with experimental and model results from Macherey *et al.* (2006; 2007) and Van Wieringen *et al.* (2005; 2006). The nomenclature of the waveforms is the same as that provided by Van Wieringen *et al.* (2005) and Macherey

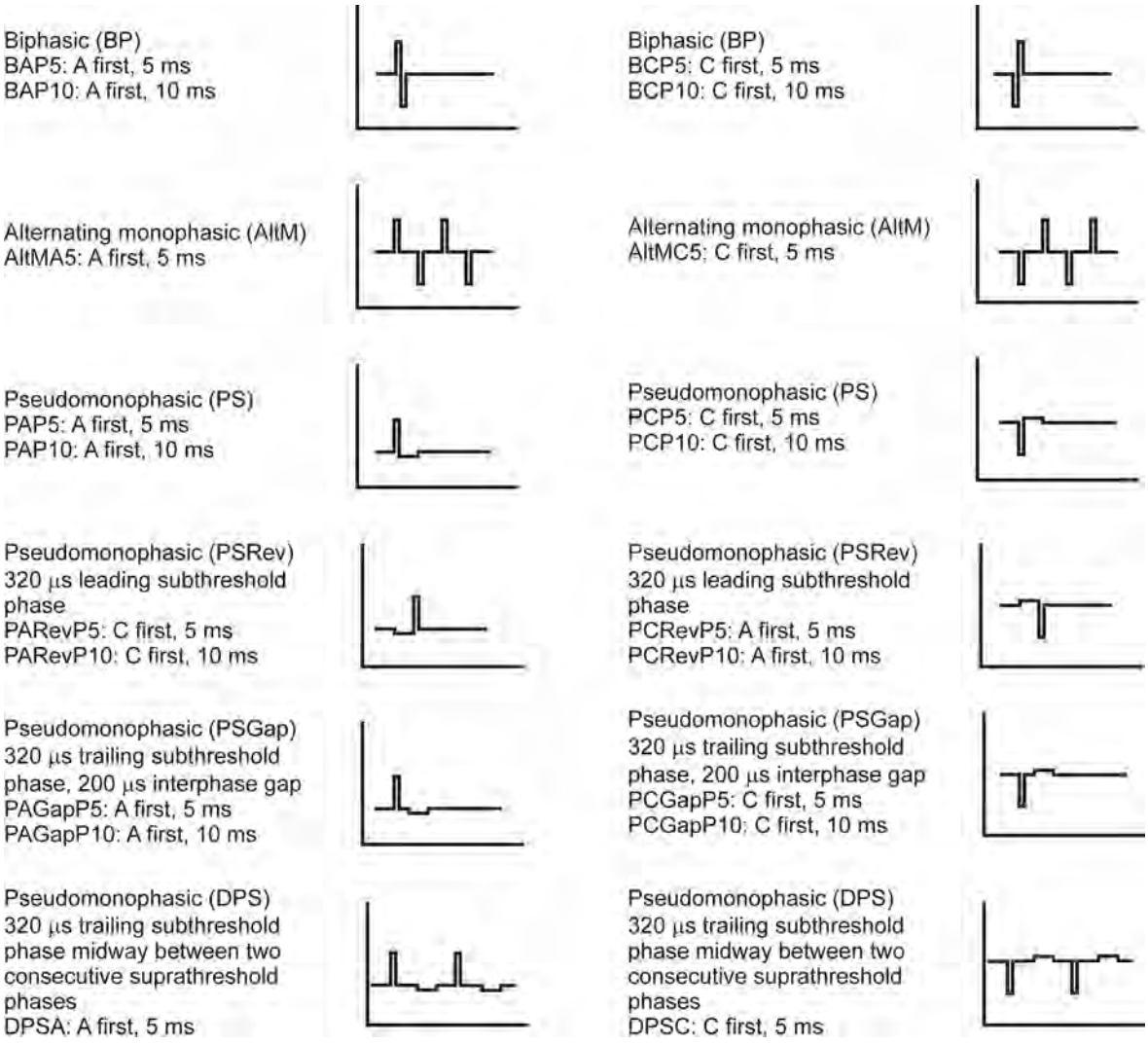

Figure 7.1: Overview of the different stimulus waveforms used to predict thresholds. The nomenclature is the same as that provided by Van Wieringen *et al.* (2005) and Macherey *et al.* (2006). Note that for the PSRev waveforms the polarity nomenclature in the name refers to the original PS waveform polarity, although the polarity is reversed.

et al. (2006). "BP" indicates a biphasic, "PS" a pseudomonophasic, "DPS" a delayed pseudomonophasic and "AltM" an alternating monophasic waveform respectively. Anodic-first stimulation is indicated by "A" and cathodic-first by "C". "P5" and "P10" refer to a 5.0 ms or 10.0 ms stimulation period respectively.

Phase durations for biphasic waveforms (BAP5, BCP5, BAP10 and BCP10) and alternating monophasic waveforms (AltMAP5 and AltMCP5) were 40 μs/phase. The high-amplitude short-duration phase of the pseudomonophasic waveforms (PAP5, PCP5, PAP10, PCP10) was 40 μs/phase, while the low-amplitude long-duration phase was eight times longer. The temporal effect of the two different phases of the pseudomonophasic waveforms was examined by reversing the two phases so that the low-amplitude long-duration phase leads (PARevP5, PCRevP5, PARevP10 and PCRevP10). Alternatively an interphase gap (IPG) of five times longer than the short-duration phase was introduced (PAGapP5, PCGapP5, PAGapP10, PCGapP10), as well as a longer IPG in the form of delayed pseudomonophasic waveforms (DPSAP5 and DPSCP5) as described by Macherey *et al.* (2006).

7.2.2 Threshold predictions

Thresholds were determined by calculating neural excitation curves for each stimulus waveform condition. The minimum threshold current for each curve was considered the threshold for the specific condition, with these minima located in close vicinity to the stimulating electrode.

Thresholds observed for different pulsatile waveforms differ widely among implantees as a result of variability in factors such as implant type, degree of degeneration of the ANF population, electrode geometry, intrascalar electrode location and stimulation strategy (Nadol Jr, 1990; Schuknecht, 1993; Zimmermann *et al.*, 1995; Nadol Jr, 1997; Arts *et al.*, 2003; Cohen *et al.*, 2003; Abbas *et al.*, 2004; Van Wieringen *et al.*, 2005; Fayad and Linthicum Jr, 2006). The model is hence only used to predict and compare relative threshold differences between different stimuli and not to predict thresholds differences observed in and between implantees.

7.3 RESULTS

7.3.1 Effect of electrode array position

Thresholds calculated for stimulation with the contour and straight electrode arrays respectively, using biphasic stimuli of 100 μs/phase, are shown in Figure 7.2. Threshold differences between different stimulus conditions and nerve fibre degeneracy were more pronounced with contour array stimulation than with straight array stimulation. It was therefore decided to consider only contour array stimulation in order to observe threshold differences between different pulsatile waveforms better.

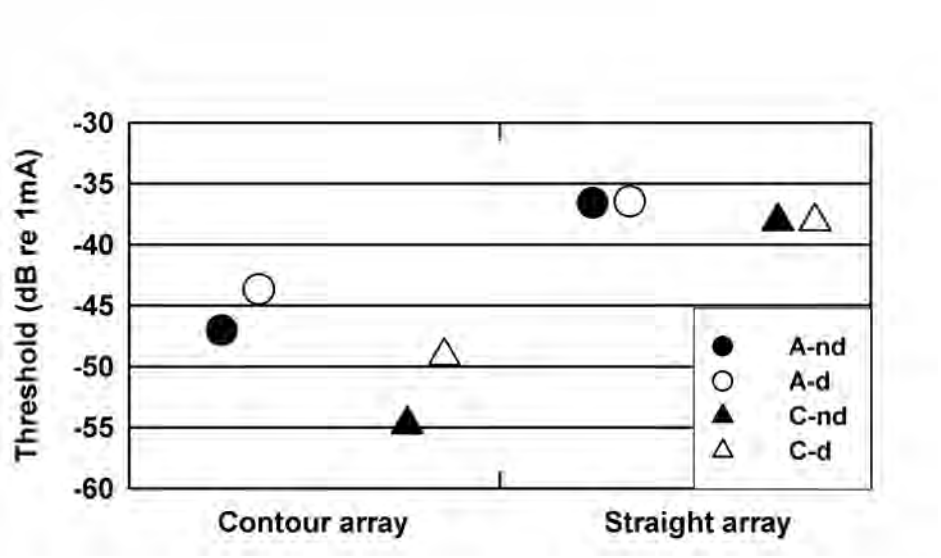

Figure 7.2: Thresholds determined for stimulation with the contour and straight electrode arrays respectively for non-degenerate (nd) and degenerate (d) ANF populations. Stimuli were charge-balanced and biphasic with 100 μs/phase phase durations and delivered to a monopolar stimulated electrode in the basal cochlear turn. Both anodic-first (A) and cathodic-first (C) stimuli were considered. Filled markers indicate non-degenerate and open markers degenerate nerve fibre populations. Anodic-first stimulation is indicated with circles and cathodic-first stimulation with triangles.

In general, cathodic-first stimuli produced lower thresholds compared to anodic-first stimuli in both non-degenerate and degenerate nerve fibre populations. With contour array stimulation, thresholds were 6.0 – 7.0 dB lower for cathodic-first stimuli. An increase in nerve fibre degeneracy elevated thresholds by 3.5 dB for cathodic-first

stimuli compared to 5.7 dB for anodic-first stimuli. With straight array stimulation, thresholds were about 1.5 – 2.0 dB lower for cathodic-first stimuli and nerve fibre degeneracy did not seem to influence threshold levels.

7.3.2 Effects of a low-amplitude long-duration phase

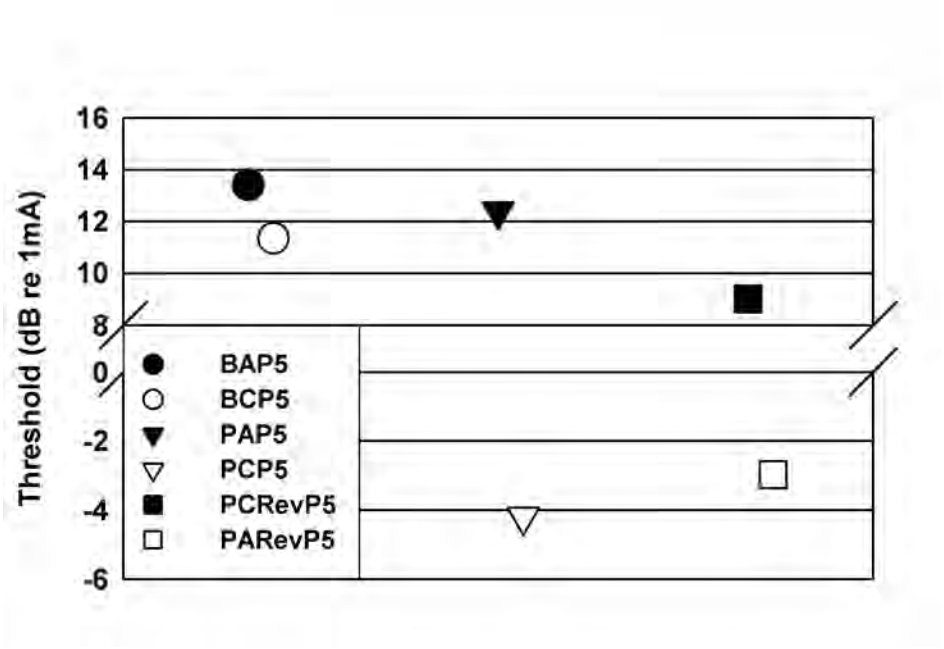

Figure 7.3: Threshold predictions for anodic-first (A) and cathodic-first (C) stimuli of biphasic waveforms (BAP5, BCP5) and pseudomonophasic waveforms with trailing (PAP5, PCP5) and leading (PARevP5, PCRevP5) subthreshold phases. Phase durations for high-amplitude short-duration phases were 40 μs/phase and 320 μs/phase for the low-amplitude long-duration phases. Pulse rates were 200 pps. Closed markers indicate anodic-first and open markers indicate cathodic-first stimuli.

The effectiveness of replacing either one of the phases of the BP waveforms with a pseudomonophasic phase of low amplitude and long duration was investigated. Figure 7.3 shows the threshold comparisons between biphasic (BAP5, BCP5), pseudomonophasic (PAP5, PCP5) and reversed pseudomonophasic (PARevP5, PCRevP5) waveforms for cathodic-first and anodic-first stimuli. Phase durations of the biphasic and high-amplitude short-duration phases of the PS and PSRev waveforms were 40 μs/phase, with the low-amplitude long-duration phases of the latter two waveforms 320 μs/phase.

For biphasic waveforms, thresholds for cathodic-first stimuli were 2.07 dB lower than for anodic-first stimuli. This is about 4.0 dB less than the same stimulus polarity threshold reductions predicted for the longer phase biphasic waveforms in Figure 7.2. The trend of a threshold reduction with increased phase duration compared favourably with similar measured results of threshold reductions ranging between 3.0 and 6.0 dB for PS waveforms reported previously for bipolar (Van Wieringen *et al.*, 2006) and a mean threshold reduction of 2.0 dB for anodic-first PS waveforms using monopolar stimulation (Macherey *et al.*, 2006).

Results further predicted a reduction in threshold for both stimulus polarities when one of the phases of the BP waveform was replaced with the prolonged phase. Replacement of the trailing phase resulted in thresholds being 1.02 dB lower for anodic-first and 15.54 dB lower for cathodic-first. Replacement of the leading phase of the BP waveform resulted in a threshold reduction of 14.33 dB for cathodic-first stimuli compared to only 4.41 dB for anodic-first stimuli.

In general, threshold reductions followed the same trends observed in the Van Wieringen *et al.* (2005) study. They observed lower thresholds for cathodic-first biphasic stimuli compared to anodic-first stimuli, as well as reduced thresholds for leading and trailing prolonged phase PS waveforms compared to BP waveforms. However, for three of the four subjects observed, anodic-first stimuli produce lower thresholds than cathodic-first stimuli in both types of PS waveforms. Threshold differences are also less pronounced than those predicted in this study.

7.3.3 Effects of an interphase gap

The effects of delaying the charge recovered from the leading phase were predicted through addition of a gap between the leading and trailing phases of BP and PS waveforms. For the BP waveforms of rate 200 pps (i.e. BP waveforms having a 5.0 ms stimulation period), a gap of 5.0 ms was inserted between the two phases. This resulted in alternating monophasic (AltM) waveforms of rate 100 pps (i.e. having a stimulation period of 10.0 ms). For PS waveforms two such alternations were made by *a*) inserting a 200 μs gap between the two phases; and *b*) delaying the low-amplitude long-duration trailing phase to be halfway between two consecutive high-amplitude short-duration leading phases.

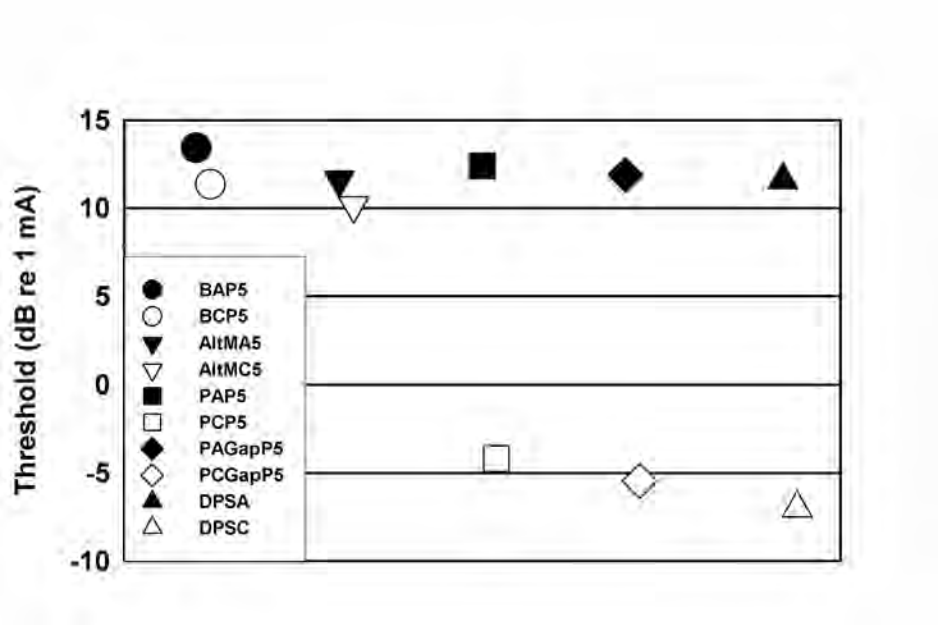

Figure 7.4: Threshold predictions for increasing the interphase gap of BP and PS waveforms. BP and PS stimuli are the same as presented in Figure 7.3. Predictions were made for anodic-first (A) and cathodic-first (C) stimuli of alternating monophasic (AltMA5, AltMC5), pseudomonophasic (PAGapP5, PCGapP5) with a 200 μs interphase gap and delayed pseudomonophasic (DPSA, DPSC) waveforms. Waveform parameters are the same as in Figure 7.3.

In the Van Wieringen *et al.* (2006) study threshold reductions range between 5.0 and 8.0 dB in the case of AltM waveforms for bipolar stimulation, while for monopolar stimulations a mean reduction of about 18.0 dB is observed for both anodic-first and cathodic-first stimuli (Macherey *et al.*, 2006). Predicted threshold reductions are shown in Figure 7.4. In the case of AltM waveforms of both stimulus polarities, only small threshold reductions were predicted and ranged between 1.21 and 1.82 dB. Increasing the IPG of PS waveforms also resulted in increased threshold reductions. Reductions were more pronounced for cathodic-first stimuli, being 1.27 dB lower for PSGap and 2.81 dB lower for DPS. For anodic-first stimuli reductions ranged between 0.51 and 0.79 dB. Compared to experimental results, these reductions were less than expected.

7.3.4 Effect of an increase in the interpulse interval

Interpulse intervals (IPIs) for BP and PS waveforms were increased from 5 ms to 10 ms, while all other waveform parameters were kept constant. The effect of the IPI increase on both anodic-first and cathodic-first stimuli is shown in Figure 7.5.

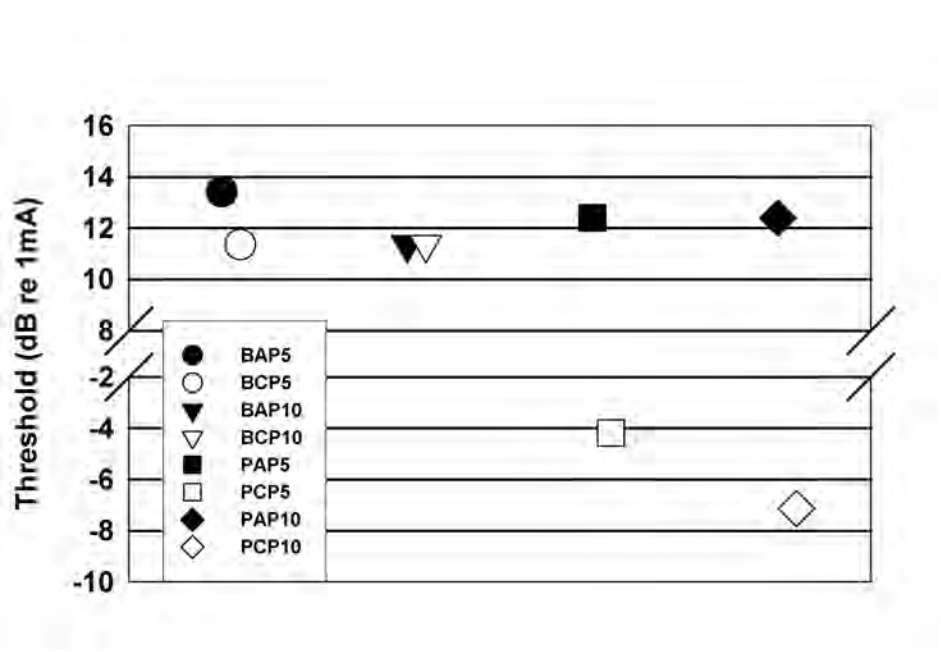

Figure 7.5: Threshold predictions for increasing the interpulse interval of anodic-first (A) and cathodic-first (C) BP and PS waveforms from 5 ms to 10 ms. BP and PS stimuli, as well as waveform parameters, are the same as in Figure 7.3.

For the BP waveform anodic-first stimulation resulted in a 2.07 dB reduction in threshold, while the reduction predicted for cathodic-first stimulation was negligible. These small threshold differences are comparable to the results of Van Wieringen *et al.* (2005) and Macherey *et al.* (2006), indicating threshold changes with an IPI increase of 5 ms of less than 1.0 dB for bipolar and less than 3.0 dB for monopolar anodic-first stimulation.

Increasing the IPI of the PS waveform resulted in a threshold reduction of 2.94 dB for cathodic-first and a negligible reduction for anodic-first stimulation, indicating an opposite threshold dependence on stimulus polarity compared to BP waveforms. Macherey *et al.* (2006) observed no significant threshold dependence on polarity for

PS and DPS waveforms, with threshold differences between the two polarities less than 1.0 dB.

7.3.5 Comparison between measured and modelled results

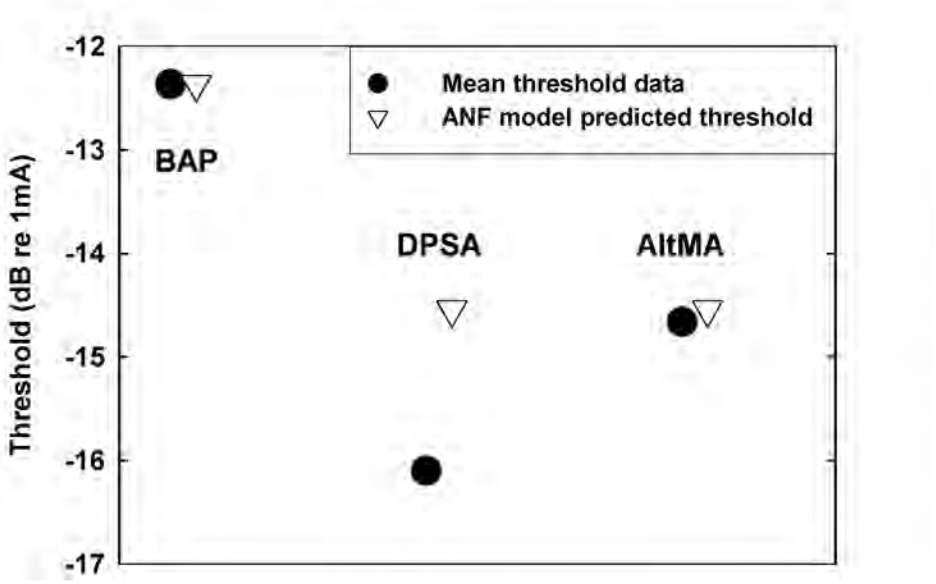

Figure 7.6: Threshold comparisons between predicted ANF model and observed mean threshold data reproduced from Figure 10 in Macherey *et al.* (2006) for anodic-first stimuli of BP, DPS and AltM. For the Macherey *et al.* (2006) data (closed markers) the high-amplitude short-duration phase is 21.6 μs, the low-amplitude long-duration phase is 172.4 μs, and the rate is 813 pps for the BP and DPS waveforms and 407 pps for the AltM waveform. For the ANF model predictions (open markers) the high-amplitude short-duration phase is 40.0 μs, the low-amplitude long-duration phase is 320.0 μs, and the rate is 800 pps for the BP, 200 pps for the DPSA and 400 pps for the AltM waveforms.

All of the above results were model predictions of tendencies observed when varying the parameters of biphasic and asymmetric waveform shapes. Of interest is how well the model can predict measured results. All simulations in this study were performed for a monopolar electrode configuration and the model predictions cannot be arbitrarily referenced to the biphasic anodic-first reference waveforms of the Van Wieringen *et al.* (2005) study that employed a bipolar electrode configuration. However, Macherey *et*

al. (2006) employed monopolar stimulation and ANF model predictions could hence be arbitrarily referenced to their biphasic anodic-first reference stimuli.

Comparisons between anodic-first BP, DPS and AltM waveforms are illustrated in Figure 7.6. Phase duration and stimulus rate values are indicated in the figure legend, with phase durations of the Macherey *et al.* (2006) stimuli about half of the modelled stimuli. Given the threshold differences predicted when varying phase duration, IPG and IPI, the model was able to make reasonable predictions of general trends measured for mean thresholds from human subjects. Pulse rates for the DPSA stimuli used in the Macherey *et al.* (2006) study were four times faster than pulse rates employed in the simulations. The difference between the measured and calculated thresholds for the DPSA waveforms may be attributed to refractory period differences between real and simulated ANFs, as discussed below in Section 7.4.

7.3.6 Effects of pulse rate

Pulse rate effects on thresholds were studied by Van Wieringen *et al.* (2006) and Macherey *et al.* (2007) for BP and AltM waveforms at different phase durations. Results show a monotonic decrease in threshold for the BP waveform over the pulse rate range investigated, while non-monotonic behaviour is observed at low pulse rate AltM waveforms. Shannon (1985) also observed non-monotonic trends in threshold behaviour for BP waveforms over a wider range of pulse rates than those in the Van Wieringen *et al.* (2006) study.

Pulse rate effects were investigated with the ANF model over the range 200 – 5,000 pps for BP and AltM waveforms of 40 μs/phase durations for non-degenerate and degenerate nerve fibres (Figures 7.7(a) and (b)). Results were arbitrarily referenced to a 200 pps BP reference waveform. This was performed by determining a guestimate of the threshold that a measured 200 pps BP waveform of 40 μs/phase would have from Figures 3b and 5 in Van Wieringen *et al.* (2006). Fayad and Linthicum Jr (2006) reported a mean spiral ganglion cell count in 14 implanted temporal bones of about 67% less than that known to be in normal hearing persons (Schuknecht, 1993). Mean threshold curves for the two waveforms were thus calculated from Figures 7.7(a) and (b) by assuming a mixed population of 33% non-degenerate and 67% degenerate nerve fibres (Figures 7.7(c) and (d)).

In general thresholds were higher for degenerate compared to non-degenerate nerve fibres (Figures 7.7(a) and (b)). Results indicated threshold reductions for both BP and AltM waveforms at pulse rates higher than 1,000 pps, although the average reduction of 1.3 dB/doubling predicted for the mean BP waveform was less than the 3.6 dB/doubling predicted for the AltM waveform (Figures 7.7(c) and (d)). For BP waveforms having pulse rates less than 1,000 pps, thresholds did not follow the trend of a monotonic decrease with increasing pulse rate. Results also did not predict the non-monotonicities observed at low pulse rate AltM waveforms.

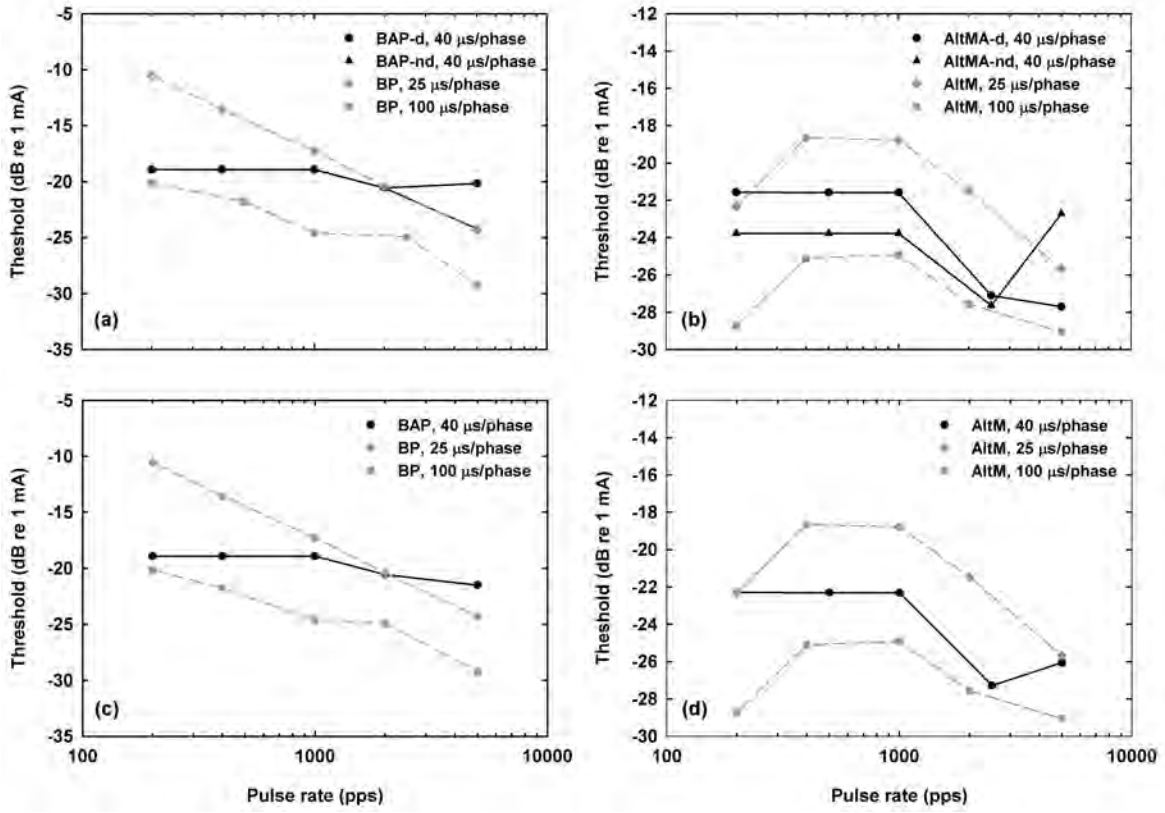

Figure 7.7: Thresholds as a function of pulse rate of (a, c) BP and (b, d) AltM waveforms at 25, 40 and 100 μs/phase durations for anodic-first stimuli. The experimental results at 25 and 100 μs/phase are reproduced from Figure 5 in Van Wieringen *et al.* (2006) and are indicated in grey (dashed lines). (a, b) Thresholds at 40 μs/phase were calculated for non-degenerate (*nd*, black solid lines, triangles) and degenerate (*d*, black solid lines, circles) nerve fibres. (c, d) Mean thresholds were calculated from (a) and (b) by assuming a mixed nerve fibre population of 33% non-degenerate and 67% degenerate nerve fibres.

7.4 DISCUSSION

In this chapter the possibility is investigated that the ANF model is able to predict threshold changes observed for different waveform shapes of different polarity, phase duration and pulse rate. Stimulation was monopolar for a contour array electrode located in the basal turn of the modelled cochlea.

Deurloo, Holsheimer and Bergveld (2001) investigated the threshold-distance relationship between a monopolar electrode and mammalian nerve fibres with a 3D volume conduction model by analysing the effect that presentation of subthreshold prepulses, i.e. pulses similar to the PS waveform, have on the nerve fibre's electrical behaviour. They stated that "the two basic relations of the stimulus current needed for nerve fibre activation are: (1) the current is inversely related to the calibre of the myelinated nerve fibre and (2) the current increases approximately proportional to the square of the distance between the nerve fibre and the stimulating electrode .... These two relations imply that with a given stimulus amplitude, larger fibres will be activated up to a larger distance from the cathode than smaller fibres. Therefore, larger fibres will be activated in a larger area of a nerve trunk than smaller fibres."

The first relation is in part based on a report by McNeal (1976) that, because of their longer internodal lengths, nerve fibres having a larger calibre, i.e. a larger diameter, are excited at lower threshold currents than thinner fibres. Simulation studies by Wesselink *et al.* (1999) and Rattay (1990) are in accord with this observation. As discussed in Chapter 5, the axonal part of the ANF model is based on the general peripheral sensory nerve fibre model developed in Chapters 3 and 4. In Sections 4.3.6 and 4.4 evidence was provided that the general sensory nerve fibre model is not in full accord with the abovementioned results, since for larger diameter fibres (larger than 10.0 μm) an increase in threshold current occurred with an increase in diameter. However, in the smaller diameter regime in which ANF fibre diameters fall, the general nerve fibre model, and hence the ANF model as well, complied with the first relation.

Single-fibre studies by Ranck Jr (1975) and model results by, among others, Rattay (1990) indicate that the threshold current increases with the square of the distance from the electrode, complying with the second relationship stated above. The electric and potential fields become weaker as the electrode-to-fibre distance increases, with the result that larger threshold stimulus currents are necessary to excite the fibre at larger

distances. This has the effect that as the fibre distance from the electrode increases, the excitation region around the electrode increases, since more Ranvier nodes fall inside the depolarised region. In cochlear implant research both experimental and modelling studies reported lower thresholds for fibres located closer to the stimulating electrodes, with the greatest reduction for fibres lying closest to the electrodes (Javel *et al.*, 1987; Miller *et al.*, 1993; Shepherd *et al.*, 1993; Hanekom, 2001b; Briaire and Frijns, 2006). These results are also supported by the results presented in Figure 7.2, with thresholds for fibres obtained with contour array stimulation reduced compared to straight array stimulation.

From the two relationships presented by Deurloo *et al.* (2001) it can be argued that when a stimulating monopolar electrode is located an equal distance from the dendrite on the one hand and the axon on the other, the axon would be excited at lower threshold currents than the dendrite. Current-distance relationships calculated for a myelinated nerve fibre confirm this argument (refer to Figure 6 in Rattay, 1987). However, the difference predicted in Figure 7.2 between non-degenerate and degenerate ANFs cannot be explained by this argument alone. The situation in the cochlea is more complicated owing to the spatial arrangement of fibres (refer for example to the cross-sectional diagram of the modelled cochlea employed in this study, as shown in Figure 5.2). From Figure 5.2 it is clear that each ANF is shaped in a curved fashion, with the dendrites in general located closer to the electrode array than the axons, even more so for ANFs located close to an electrode compared to ANFs located between two consecutive electrodes. Since retrograde degeneration causes the dendrites to retract, while the somas and axons survive (Spoendlin and Schrott, 1989; Nadol Jr, 1990; Schuknecht, 1993), excitation in degenerate fibres is expected to occur more centrally along the fibre, i.e. axonal excitation. It can therefore be deduced that thresholds predicted for non-degenerate fibres located close to the stimulating electrode will be lower than for degenerate fibres. This is clearly observed in the case of contour array stimulation, but not in the case of straight array stimulation. The reason is found in the way the ANF is modelled. The dendritic part of the Rattay *et al.* (2001b) model, which is assumed myelinated, is reserved in the ANF model (refer to Figure 5.1). This is in contrast to real ANFs where the dendrites are mostly unmyelinated (Glueckert *et al.*, 2005a). Furthermore, comparison between the internodal lengths of the dendrite and axon shows longer dendritic than axonal internodal lengths. In myelinated fibres located closely to electrodes, the threshold current is mainly dependent on the electrode-to-node distances and not so much on the electrode-to-fibre distance as is

the case of unmyelinated fibres (refer to Figure 6 in Rattay, 1987). Threshold currents are also lower when the electrode is located at a node compared to when it is located between nodes. The straight array is located closer to the terminal of the ANF than the contour array (refer to Figure 5.2) and therefore has to excite a larger part of the dendrite in a non-degenerate fibre to create a propagating AP. The degenerate fibre was simulated with almost no dendrite left (Figure 5.1) and excitation occurred in the axon. Since the nodes of the axon are spaced close together, lower thresholds currents might be expected than for dendritic excitation, but the additional electrode-to-fibre distance increases the threshold current. This is confirmed by the results shown in Figure 6 in Rattay (1987), where simulations predicted similar thresholds at longer electrode-to-fibre distances for a myelinated fibre of double the diameter to thresholds predicted in the thinner fibres when the electrode is located closer to the node in the former case than in the latter.

Thresholds are reported to be dependent on electrode configuration with monopolar stimulation in cats and guinea-pigs yielding lower thresholds than bipolar stimulation (Black and Clark, 1980; Black *et al.*, 1983; Miller *et al.*, 1995; Rebscher *et al.*, 2001). Lower thresholds are also recorded for monophasic stimuli compared to BP stimuli in single-fibre and ECAP studies performed by Miller *et al.* (1995; 1999b; 2001b) on cats and guinea-pigs. Miller *et al.* (2003) measured the growth in ECAP amplitudes in cats employing monophasic and BP stimuli for both monopolar and bipolar stimulation modes. Results indicate larger threshold differences between the monophasic and BP stimuli for monopolar stimulation than for bipolar stimulation. They attributed the threshold differences to the difference in voltage gradient produced by the two stimulation modes. With a monopolar electrode a single potential gradient is produced, while bipolar stimulation produces two gradients. Simulations performed with 3D spiralling cochlear models also indicate two potential gradients of opposite sign (Briaire and Frijns, 2000; Hanekom, 2005). Miller *et al.* (2003) hence argued that with a bipolar electrode pair nerve fibres close to one of the electrodes will always be excited, irrespective of the type of stimulus presented. They reasoned that for monopolar stimulation a BP waveform will introduce a second polarity, and hence the change in the potential field will be greater than for a monophasic waveform, leading to the larger observed threshold differences. Increasing the duration of the second phase of BP stimuli, i.e. stimulation with PS stimuli, leads to a relatively large reduction in threshold compared to BP stimuli (Miller *et al.*, 1995; Shepherd and Javel, 1999; Miller *et al.*, 2001b; Van Wieringen *et al.*, 2005; Macherey *et al.*, 2006). Furthermore, reversal

of stimulus polarity resulted in larger observed threshold differences when monophasic stimulation was used (Miller *et al.*, 1999b), compared to the differences observed with BP stimuli (Shepherd and Javel, 1999).

Predicted threshold reductions shown in Figure 7.3 for BP waveform replacement with PS waveforms followed the trend of larger threshold reductions for monopolar stimulation than for bipolar stimulation. Lower thresholds were also predicted for PS waveforms compared to BP waveform for both stimulus polarities. However, the threshold differences between BP and AltM waveforms shown in Figure 7.4 were less than experimentally observed for both bipolar and monopolar stimulation (compare with Van Wieringen *et al.*, 2005; Macherey *et al.*, 2006). This may be attributed to the refractory periods of the modelled ANF. Calculated ARP values of about 0.8 – 0.9 ms were 44% longer than the measured ARP values of 0.5 ms for humans, while the calculated RRP values were 15 – 23% shorter than RRP values of about 5.0 ms (compare Section 5.3.2 and Brown *et al.*, 1990). The results in Figure 7.3 were for low pulse rate predictions and from the effect pulse rate has on thresholds, presented in Figure 7.7, it can be deduced that the longer ARP value of the modelled ANF resulted in an overestimation of thresholds for low pulse rate AltM waveforms. This can be explained as follows: For each anodic-cathodic phase-pair in the AltM stimulus, the leading anodic phases hyperpolarise the membrane, thus lowering the fibre's threshold. The lower threshold enables the trailing cathodic phases to depolarise the membrane more easily to elicit an AP. However, with low pulse rate pulses, the membrane has time to recover from the hyperpolarised state before it is depolarised. If the AP is elicited during the ARP time window, the AP amplitude will be too low to propagate. Hence, the threshold current needed to elicit a propagating AP will be raised.

Thresholds recorded for monopolar simulation display dependence on stimulus polarity with single-fibre studies by Van den Honert and Stypulkowski (1987b) and ECAP studies by Miller *et al.* (1998; 1999b; 2001a) recording lower thresholds for cathodic stimuli than for anodic stimuli in cats. However, in guinea-pigs the situation is reversed, with anodic stimuli yielding lower thresholds (Miller *et al.*, 1998). The threshold differences in the cat studies may be attributed to the observation that cathodic stimuli excite fibres more distally than anodic stimuli do, although the influence the soma plays is unclear (Miller *et al.*, 1999b). No preference is observed between the stimulus polarities with bipolar stimulation (Miller *et al.*, 2003). Calculated thresholds in this study were in accord with observations on stimulus polarity for monopolar stimulation in

cat. However, simulations were performed for a degenerate ANF population and stimulus polarity differences could hence not be attributed to the difference in stimulation site between the two polarities. As discussed earlier in this section, the combination of contour array stimulation and ANF degeneracy most probably resulted in axonal stimulation irrespective of stimulus polarity. The calculated differences might rather be the result of the way in which the two polarities depolarises the fibre (Rattay, 1987). However, this was not investigated further and additional study in this regard is advised.

Subthreshold prepulses similar to PSRev waveforms, but with both phases having a cathodic polarity, have been investigated as a possible way to stimulate nerve fibres in a nerve trunk selectively (Grill and Mortimer, 1995; Grill and Mortimer, 1997; Deurloo *et al.*, 2001). Simulation reports indicate an inversion of the threshold-distance relationship with lower thresholds observed for fibres located further away from the electrode, and those within a certain distance from the electrode threshold currents for small nerve fibres are lower than for thicker nerve fibres. The authors argued that a possible mechanism for these simulation predictions is two-fold. Firstly, the prepulse activates a certain percentage of the sodium channels at the Ranvier nodes closest to the electrode, thus reducing the sodium conductance. When the actual pulse stimulates the nerve fibre, the resulting AP has a reduced amplitude. Secondly, the threshold current needed to activate the nodes is elevated to such an extent that the neighbouring nodes are strongly hyperpolarised and hence the AP is blocked from propagating. Comparison between the neural excitation curves for PCP5 and PARevP5 waveforms showed a shift in the position of the minimum threshold predicted for the PARevP5 waveform away from the stimulating electrode compared to the PCP5 waveform (results not shown). However, an investigation into the sodium conductance reduction mechanism links up with the stimulus polarity investigation suggested in the previous paragraph as a further study.

Shannon (1985) measured thresholds in humans for BP waveforms of varying pulse rate and phase duration using monopolar stimulation. Thresholds are reduced with an increase in phase duration. Furthermore, for short phase durations (< 0.5 ms), thresholds are constant for pulse rates up to 100 pps, after which it decreases by about 3 dB/octave (see Figure 1 in Shannon, 1985). Van Wieringen *et al.* (2006) observed similar non-monotonical behaviour with an increase in pulse rate for BP and AltM stimuli. For BP stimuli reported thresholds reduce between 1.6 and 2.6 dB/doubling

of rate for pulse rates between 200 and 5,000 pps. Threshold reductions for AltM stimuli vary between 1.1 and 2.0 dB/doubling of rate over the same range of pulse rates. Shannon (1985) suggested that two different mechanisms are at play for short and long pulse durations respectively, with the long pulse duration mechanism being an integrator process with a 1 – 2 ms time constant. He referred to results from Pfingst and Sutton (1983) reporting that low frequency thresholds, i.e. long pulse duration thresholds, in monkeys correlate with dendritic survival near the stimulating electrode. Thresholds are elevated in regions of degenerate nerve fibres, and hence poor dendritic survival, compared to regions with more intact nerve fibres with more dendritic survival. Furthermore, he referred to the suggestions made by Van den Honert and Stypulkowski (1984) of two sites of activation on the nerve fibre relative to the soma and that dendrites integrate current slower than the soma with a time constant of 1 – 2 ms. Shannon (1985) argued that these findings suggest that the higher thresholds observed for lower frequency, i.e. long pulse duration, stimuli can be attributed to low dendritic survival.

Macherey *et al.* (2007) expanded the Carlyon *et al.* (2005) phenomenological model and reported that simulated predictions of the stochastic model version are able to follow the trends observed in the Shannon (1985) study, but not for the deterministic version. Van den Honert and Stypulkowski (1984), among others, observed a reduction in jitter, and hence in stochastic behaviour, when the amount of degeneracy of nerve fibres is increased, while Miller *et al.* (1999b) recorded greater jitter for longer pulse durations in cats and a reduction in jitter with an increase in FE. This suggests that for long pulse durations less jitter, and hence dendritic activity, will result in higher observed thresholds. Thus it can be argued that the stochastic Macherey *et al.* (2007) model does not simulate a population of non-degenerate nerve fibres only, but rather a mixed population of degenerate and non-degenerate nerve fibres. The inability of the deterministic version of the Macherey *et al.* (2007) model to predict the Shannon (1985) results of threshold reductions with an increase in pulse rate, may be an indication of either an underestimation of thresholds at low pulse rates or an overestimation of thresholds observed at higher pulse rates. In the former case, the lower threshold predictions at lower pulse rates will then suggest that their deterministic model possibly simulates mostly a population of non-degenerate nerve fibres.

The dual-process model by Macherey *et al.* (2007) consists of integrator and resonator

processes. They showed that the non-monotonicities can be attributed to the resonant process. They argued that even though the HH model is a resonator model, the model's ion channels are insufficient to account for the non-monotonicities experimentally observed, since the model's time constants are too small. The ion channels responsible for the correct time constants may be a combination of persistent sodium and slow potassium currents. The ANF model used in this study was a deterministic model containing persistent sodium and slow potassium currents. It could be used to simulate non-degenerate and degenerate nerve fibres. Figure 7.7 shows that the model was able, within reason, to predict the non-monotonic behaviour in thresholds for pulse rates higher than 1,000 pps, confirming the suggestion by Macherey *et al.* (2007).

However, at low pulse rate BP waveforms the ANF model underestimated thresholds and at high pulse rates overestimated thresholds. The model also did not correctly predict the threshold changes observed for low pulse rate AltM waveforms. This can be attributed partly to a difference in the refractory periods between real and simulated ANFs as discussed previously. In addition, the inclusion of stochastic behaviour in the model would enable modelling of the relationship between jitter and FE mentioned earlier. Hence, it could possibly better predict the threshold differences observed at low pulse rates between non-degenerate and degenerate nerve fibres. The development of a stochastic version is therefore advised.

7.5 CONCLUSION

In conclusion it seems possible that the human ANF model is able to make a reasonable prediction of temporal characteristics of different biphasic, pseudomonophasic and alternating monophasic waveforms, as well as the non-monotonic behaviour observed at high pulse rates. Since the model contained both persistent sodium and slow potassium currents, it is suggested that the inclusion of these currents can in part simulate non-monotonic behaviour in ANFs. However, these non-monotonic trends observed cannot be explained by the combination of persistent sodium and slow potassium currents alone. Results indicate that other possible contributing factors include refractory behaviour of the nerve fibre and the stochastic representation of the ion channels at the Ranvier nodes.

Chapter 8

GENERAL DISCUSSION AND CONCLUSION

8.1 RESEARCH OVERVIEW

In 1952 Hodgkin and Huxley published an empirical set of equations describing changes in the neural membrane potential of the squid giant axon during the application of depolarising or hyperpolarising stimuli. Since these equations were derived for an unmyelinated nerve fibre, reservations exist about their applicability to describe action potential propagation in myelinated mammalian nerve fibres adequately.

Huxley (1959) suggested that by accelerating the activation and inactivation of membrane sodium ion permeability of the HH model fourfold, firing behaviour at a myelinated amphibian Ranvier node can be represented. The HH model is able to predict human ANF excitation, provided the nodal ion channel kinetics are accelerated tenfold (Rattay, 1990; Rattay and Aberham, 1993). This modified HH model shows improved human ANF response predictions by replacement of the squid morphometric properties by human morphometric properties, as well as changing the cable morphometric properties to those of human (Rattay *et al.*, 2001b).

The main endeavour of this study was to determine whether the HH model for unmyelinated nerve fibres could be modified more comprehensively to predict excitability

behaviour at Ranvier nodes of a human sensory nerve fibre, as applied specifically to the prediction of temporal characteristics of the human auditory system. The model was developed in three phases. Firstly, the HH-model was modified to describe action potential dynamics at Ranvier nodes using recorded ionic membrane current data from single human myelinated peripheral nerve fibres (Reid *et al.*, 1993; Scholz *et al.*, 1993; Schwarz *et al.*, 1995; Reid *et al.*, 1999) together with the temperature dependency of all parameters (Chapter 3). Secondly a nerve fibre cable model, based on a combination of the models by Rattay *et al.* (2001b) and Blight (1985), was constructed using human sensory nerve fibre morphometric data (Chapter 4). Lastly the morphological parameters of the nerve fibre model were changed to a Type I peripheral ANF and coupled to a volume conduction model of the cochlea (Chapter 5).

The Type I ANF model had to be verified against experimentally measured temporal characteristic data. Chapters 6 and 7 focussed on applications of the ANF model to verify the model and to determine its applicability as part of larger models to address questions pertaining to the cochlear implant research field.

8.2 RESULTS AND DISCUSSION

In Chapter 3 a model of a single Ranvier node was developed as part of a larger model to describe excitation behaviour in a generalised human peripheral sensory nerve fibre (Research objective 1). Parameter values describing the ionic and leakage conductances, corresponding equilibrium potentials, resting membrane potential and membrane capacitance of the original HH model were modified to reflect the corresponding parameter values for human, with the equations left unaltered. Parameter temperature dependence was included. The activation kinetics of the HH model's potassium current were slowed down to represent the activation and deactivation kinetics of a slow potassium current experimentally observed at mammalian Ranvier nodes (Taylor *et al.*, 1992; Devaux *et al.*, 2004; Schwarz *et al.*, 2006).

Action potential shape and amplitude were satisfactorily predicted at 20, 25 and 37 °C and were not influenced by this potassium current, in accordance with experimental observations. The chronaxie time constant of 65.5 μs compared favourably with the estimated value of 64.9 $\pm$ 8.3 μs at 37 °C for normal rat Ranvier nodes (Bostock *et*

al., 1983). No comparison could be made with human data owing to a lack of similar Ranvier node studies for humans. Temperature dependence simulations overestimated chronaxie times by almost a factor 2 for temperatures lower than body temperature.

Chapter 4 endeavoured to determine if the human Ranvier node model developed in Chapter 3 could predict the excitability behaviour in human peripheral sensory nerve fibres with diameters ranging from 5.0 – 15 μm (Research objective 1). The Ranvier node model was extended to include a persistent sodium current and was incorporated into a generalised simple double-cable nerve fibre model. Parameter temperature dependence was included. Simulated results suggested that the new nerve fibre cable model could satisfactorily predict excitability behaviour observed in human sensory nerve fibres at different temperatures and fibre diameters.

Similar to the results of the Ranvier node model the predicted AP characteristics compared favourably with experimental results. AP durations varied inversely with fibre diameter at temperatures higher than 27 °C, but at lower temperatures this relationship was valid only for fibres thicker than 12.5 μm. Conduction velocity values varied from 2.9 to 3.5 μs^{-1} for fibre diameters ranging from 5.0 – 15.0 μm at 37 °C, but values were underestimated for fibre diameters thinner than 12.5 μm. Conduction velocities also increased with a decrease in temperature, but at a slower rate compared to experimental data. ARP and RRP values decreased with an increase in temperature. Calculated RRP values overestimated and ARP values underestimated the experimental rates by 15% and 20% respectively. The strength-duration time constant ranged from 184.3 to 273.6 μs at 37 °C over the studied nerve fibre diameter range. However, just as in the case of the Ranvier node model, time constants were overestimated at temperatures lower than body temperature. Possible explanations included the fitting procedure employed to determine the chronaxie times, bias in measured parameter values due to the measuring methodologies used, as well as an assumption of linear parameter relationships to temperature variation.

The development of the Type I ANF model was undertaken in Chapter 5 (Research objectives 1 and 4). The general human sensory nerve fibre model was incorporated into the Rattay *et al.* (2001b) ANF model. The axonal morphological parameters were changed to a Type I peripheral ANF and the model coupled to a volume conduction model of the cochlea. The 3.75 μm diameter ANF fibre located in the basal cochlear turn was stimulated with a monopolar electrode configuration from either the contour

or straight electrode arrays at body temperature (37 °C).

ARPs and RRPs compared well and were similar to those of general sensory nerve fibres of the same calibre. RRPs decreased with progressive retrograde ANF degeneration. Chronaxie times deceased and rheobase current values increased when retrograde ANF fibre degeneration was simulated. Rheobase current values were also larger for straight array compared with contour array stimulation. Mean latencies decreased with progressive retrograde ANF degeneration and agreed well with NRT measurements (Lai and Dillier, 2000). They also decreased with an increase in stimulus intensity.

The objective of Chapter 6 was to develop a simple method to estimate stimulus attenuation values by calculating the values that best fitted the modelled neural excitation profile widths to the measured ECAP profile widths (Research objectives 2 and 3). Neural excitation profile widths at the neural level for monopolar stimulation with Nucleus straight and contour arrays respectively, were simulated using a combined volume conduction-neural model. Simulations were performed for the ANF and GSEF models respectively.

The simple model correctly predicted an increase in excitation spread with an increase in loudness level as well as wider ECAP profile widths for the straight array compared to the contour array. For both nerve fibre models, the simple model predicted realistic ECAP profile width ranges for the straight array while the lower limit for the width ranges predicted for the contour electrode was comparable to measured width ranges.

Results further indicated that the modelled excitation profile widths decreased with increasing stimulus attenuation. The predicted stimulus attenuation value that best fitted the experimental results was 3.5 dB/mm for the GSEF model compared to 5.5 dB/mm for the ANF model. Despite this difference it was suggested that the proposed simple model could provide an estimate of stimulus attenuation by calculating the value of the parameter that produces the best fit to experimental data in specific human subjects.

Fitting of modelled neural excitation profile widths to measured ECAP profile widths showed that different stimulus attenuation values were needed for different stimulation levels. This might be attributed to the impedance of the electrode-electrolyte interface, which is related to stimulus attenuation, and could be dependent on stimulus intensity

Whether this actually indicated a shortcoming in the model was not certain and it was suggested that the effects of stimulus intensity on the mechanisms of stimulus decay and on the electrode-electrolyte interface impedance require further investigation.

The ability of the ANF model to predict threshold differences for biphasic, pseudomonophasic and alternating monophasic waveforms was investigated in Chapter 7 (Research objectives 4 and 5). The effect of increases in the IPG, IPI, as well as pulse rate, on thresholds was also simulated. Simulations were performed for both anodic-first and cathodic-first stimuli.

Results indicated that the model correctly predicted threshold reductions for pseudomonophasic compared to biphasic waveforms, although reduction for alternating monophasic waveforms was underestimated. Threshold reductions were more pronounced for cathodic-first stimuli compared to anodic-first stimuli. Increases in IPG and IPI respectively also predicted threshold reductions. Reversal of the phases in pseudomonophasic stimuli suggested a threshold reduction for anodic-first stimuli, but a threshold increase in cathodic-first stimuli. The inclusion of the persistent sodium and slow potassium currents in the model resulted in a reasonably accurate prediction of the non-monotonic behaviour in thresholds for pulse rates higher than 1000 pps. However, thresholds were underestimated in biphasic waveforms at lower pulse rates. The model also did not correctly predict the threshold changes observed for low pulse rate alternating monophasic waveforms. It was suggested that these results could in part be explained by the difference in the refractory periods between real and simulated ANFs, but also the lack of representation of stochasticity observed in real ANFs.

8.3 CONCLUSION AND FUTURE RESEARCH DIRECTIVES

In this study evidence was presented that the temporal characteristics of the human auditory system might be better predicted by using a modified version of the original HH model. Since the ANF model contained both persistent sodium and slow potassium currents, it is suggested that the inclusion of these currents can in part simulate non-monotonic behaviour in ANFs. This finding is valuable to create more realistic neural

models of the electrically stimulated human auditory system.

However, the squid-based dynamics of the dendritic and somal model sections need to be replaced with human dynamics to account fully for experimentally observed ANF excitation behaviour. The general sensory nerve fibre model, on which the ANF model is based, was developed from measurement data on large diameter human peripheral sensory nerve fibres. The ion channel protein (KCNQ2) responsible for slow potassium current represented in this model co-locate with sodium channels at the Ranvier nodes of larger diameter fibres (Taylor *et al.*, 1992; Devaux *et al.*, 2004; Schwarz *et al.*, 2006). Although this protein is also found at Ranvier nodes in smaller diameter fibres, in smaller diameter fibres it co-locates with KCNQ3. The distribution and density of KCNQ3 is fibre diameter dependent, with a very low density of KCNQ3 found in large diameter fibres (Schwarz *et al.*, 2006). KCNQ2 is also not found in cell bodies (Devaux *et al.*, 2004). Hence, the general sensory nerve fibre model can most probably not be used to represent ionic membrane currents in the somas and dendrites of ANF fibres. Furthermore, the dendrite in die ANF model is assumed myelinated, while SEM and TEM studies indicate unmyelinated dendrites in Type I ANF fibres (Glueckert *et al.*, 2005a). Hence a remodelling of these components is advised. Furthermore, the properties and types of ionic membrane currents of spiral ganglion cells have been characterised in murine (Mo *et al.*, 2002; Reid *et al.*, 2004; Hossain *et al.*, 2005; Chen and Davis, 2006) and guinea-pig (Bakondi *et al.*, 2008), but not in human. Consideration to the existence of similar ionic current characteristics in human spiral ganglion cells is advised in further expansions of the ANF model.

The combination of persistent sodium and slow potassium currents alone cannot explain the non-monotonic trends observed in ANF excitation behaviour. A possible contributor to explain these trends may be the inclusion of a stochastic representation of the ion channels at the Ranvier nodes (Macherey *et al.*, 2007). Temporal characteristics such as jitter, FE and refractoriness are dependent on the stochasticity of the fibre and cannot be adequately investigated with a deterministic model (refer for example to Miller *et al.*, 1999b; White, Rubinstein and Kay, 2000; Matsuoka *et al.*, 2001). A stochastic representation of the ion membrane currents of the Ranvier nodes is thus advised.

In persons with longer-term sensory loss, surviving degenerate somas and axons are demyelinated and significantly smaller than in non-degenerate ANFs (Nadol Jr, 1990;

Schuknecht, 1993; Zimmermann *et al.*, 1995; Glueckert *et al.*, 2005a). In Chapter 7 mention was made of the dependency of threshold current on fibre diameter (McNeal, 1976; Deurloo *et al.*, 2001). Furthermore, evidence exists that demyelisation alters excitation behaviour in degenerate myelinated fibres (Dimitrov, 2005; Stephanova, Daskalova and Alexandrov, 2005; Stephanova and Daskalova, 2005a; Stephanova and Daskalova, 2005b). The inclusion of the double cable model as suggested by Nygren and Halter (1999) and Dimitrov (2005) to aid in the modelling of demyelisation of the long-term degenerated ANF is suggested.

Nerve fibre behaviour is also characterised in terms of afterpotentials, the super- and subnormality of the recovery cycle and threshold electrotonus (refer for example to the review by Burke *et al.*, 2001). Initially, after the nodal membrane has depolarised, the nodal and internodal discharges rapidly. This is followed by a slower discharge of the internodal axolemma creating the afterpotentials responsibly for the supernormal phase (Blight, 1985; Burke *et al.*, 2001). The extent of this supernormality is determined by the activation and inactivation of fast potassium ion channels under the myelin sheath in the paranodal region (Burke *et al.*, 2001; McIntyre *et al.*, 2002) as well as internodal sodium ion channels (Dimitrov, 2005). In the current model no internodal ion channels are modelled. The double cable model suggested in the previous paragraph does include representations of internodal ion channels. Inclusion of the double cable model will enable an investigation of the afterpotentials and recovery phase and is thus advised.

References

Abbas, P. J. and Miller, C. A. (2004). Biophysics and physiology, *in* F. G. Zeng, A. N. Popper and R. R. Fay (eds), *Cochlear Implants: Auditory prostheses and electric hearing*, Vol. 20 of *Springer handbook of audiory research*, Springer-Verlag, New York, chapter 5, pp. 149–212.

Abbas, P. J., Brown, C. J., Shallop, J. K., Firszt, J. B., Hughes, M. L., Hong, S. H. and Staller, S. J. (1999). Summary of results using the Nucleus CI24M implant to record the electrically evoked compound action potential, *Ear & Hearing* **20**(1): 45–59.

Abbas, P. J., Hughes, M. L., Brown, C. J., Miller, C. A. and South, H. (2004). Channel interaction in cochlear implant users evaluated using the electrically evoked compound action potential, *Audiology & Neuro-Otology* **9**(4): 203–213.

Arts, H. A., Jones, D. A. and Anderson, D. J. (2003). Prosthetic stimulation of the auditory system with intraneural electrodes, *The Annals of Otology, Rhinology & Laryngology. Supplement* **191**: 20–25.

Atkins, P. W. (1995). *Physical Chemistry*, Fifth edn, Oxford University Press, Oxford.

Baker, M. D. (2002). Electrophysiology of mammalian Schwann cells, *Progress in Biophysics and Molecular Biology* **78**(2-3): 83–103.

Bakondi, G., Pór, A., Kovács, I., Szucs, G. and Rusznák, Z. (2008). Voltage-gated K^+ channel (Kv) subunit expression of the guinea pig spiral ganglion cells studied in a newly developed cochlear free-floating preparation, *Brain Research* **1210**(C): 148–162.

Behse, F. (1990). Morphometric studies on the human sural nerve, *Acta Neurologica Scandinavica. Supplementum* **82**(132): 1–38.

Black, R. C. and Clark, G. M. (1980). Differential electrical excitation of the auditory nerve, *Journal of the Acoustical Society of America* **67**(3): 868–874.

Black, R. C., Clark, G. M., Tong, Y. C. and Patrick, J. F. (1983). Current distributions in cochlear stimulation, *Annals of the New York Academy of Sciences* **405**: 137–145.

Blight, A. R. (1985). Computer simulation of action potentials and afterpotentials in mammalian myelinated axons: The case for a lower resistance myelin sheath, *Neuroscience* **15**(1): 13–31.

Boiko, T., Rasband, M. N., Levinson, S. R., Caldwell, J. H., Mandel, G., Trimmer, J. S. and Matthews, G. (2001). Compact myelin dictates the differential targeting of two sodium channel isoforms in the same axon, *Neuron* **30**(1): 91–104.

Bostock, H. (1983). The strength-duration relationship for excitation of myelinated nerve: Computed dependence on membrane parameters, *Journal of Physiology* **341**: 59–74.

Bostock, H. and Rothwell, J. C. (1997). Latent addition in motor and sensory fibres of human peripheral nerve, *Journal of Physiology* **498**(1): 277–294.

Bostock, H., Sears, T. A. and Sherratt, R. M. (1983). The spatial distribution of excitability and membrane current in normal and demyelinated mammalian nerve fibres, *Journal of Physiology* **341**: 41–58.

Briaire, J. J. and Frijns, J. H. M. (2000). Fields patterns in a 3D tapered spiral model of the electrically stimulated cochlea, *Hearing Research* **148**: 18–30.

Briaire, J. J. and Frijns, J. H. M. (2005). Unraveling the electrically evoked compound action potential, *Hearing Research* **205**: 143–156.

Briaire, J. J. and Frijns, J. H. M. (2006). The consequences of neural degeneration regarding optimal cochlear implant position in scala tympani: a model approach, *Hearing Research* **214**: 17–27.

Brown, C. J., Abbas, P. J. and Gantz, B. (1990). Electrically evoked whole-nerve action potentials: Data from human cochlear implant users, *Journal of the Acoustical Society of America* **88**(3): 1385–1391.

Brown, C. J. and Abbas, P. J. (1990). Electrically evoked whole-nerve action potentials: parametric data from the cat, *Journal of the Acoustical Society of America* **88**(5): 2205–2210.

Bruce, I. C. (2007). Implementation issues in approximate methods for stochastic Hodgkin-Huxley models, *Annals of Biomedical Engineering* **35**(2): 315–318.

Bruce, I. C., Irlicht, L. S., White, M. W., O'Leary, S. J., Dynes, S., Javel, E. and Clark, G. M. (1999a). A stochastic model of the electrically stimulated auditory nerve: pulse-train response, *IEEE Transactions on Biomedical Engineering* **46**(6): 630–637.

Bruce, I. C., White, M. W., Irlicht, L. S., O'Leary, S. J. and Clark, G. M. (1999b). The effects of stochastic neural activity in a model predicting intensity perception with cochlear implants: low-rate stimulation, *IEEE Transactions on Biomedical Engineering* **46**(12): 1393–1404.

Bruce, I. C., White, M. W., Irlicht, L. S., O'Leary, S. J., Dynes, S., Javel, E. and Clark, G. M. (1999c). A stochastic model of the electrically stimulated auditory nerve: single-pulse response, *IEEE Transactions on Biomedical Engineering* **46**(6): 617–629.

Buchthal, F. and Rosenfalck, A. (1966). Evoked action potentials and conduction velocity in human sensory nerves, *Brain Research* **3**(1): 1–122.

Burke, D., Kiernan, M. C. and Bostock, H. (2001). Excitability of human axons, *Clinical Neurophysiology* **112**(9): 1575–1585.

Burke, D., Mogyoros, I., Vagg, R. and Kiernan, M. C. (1999). Temperature dependence of excitability indices of human cutaneous afferents, *Muscle and Nerve* **22**(1): 51–60.

Caldwell, J. H., Schaller, K. L., Lasher, R. S., Peles, E. and Levinson, S. R. (2000). Sodium channel $Na_v1.6$ is localized at nodes of Ranvier, dendrites, and synapses, *Proceedings of the National Academy of Sciences of the United States of America* **97**(10): 5616–5620.

Carlyon, R. P., van Wieringen, A., Deeks, J. M., Long, C. J., Lyzenga, J. and Wouters, J. (2005). Effect of interphase-gap on the sensitivity of cochlear implant users to electrical stimulation, *Hearing Research* **205**: 210–224.

Cartee, L. A., van den Honert, C., Finley, C. C. and Miller, R. L. (2000). Evaluation of a model of the cochlear neural membrane. I. Physiological measurement of membrane characteristics in response to intrameatal electrical stimulation, *Hearing Research* **146**: 143–152.

Catterall, W. A., Goldin, A. L. and Waxman, S. G. (2005). International Union of Pharmacology. XLVII. Nomenclature and structure-function relationships of voltage-gated sodium channels, *Pharmacological Reviews* **57**(4): 397–409.

Chatterjee, M. and Shannon, R. V. (1998). Forward masked excitation patterns in multielectrode electrical stimulation, *Journal of the Acoustical Society of America* **103**(5I): 2565–2572.

Chen, C. (1997). Hyperpolarization-activated current (I_h) in primary auditory neurons, *Hearing Research* **110**: 179–190.

Chen, W. C. and Davis, R. L. (2006). Voltage-gated and two-pore-domain potassium channels in murine spiral ganglion neurons, *Hearing Research* **222**: 89–99.

Chiu, S. Y., Ritchie, J. M., Rogart, R. B. and Stagg, D. (1979). A quantitative description of membrane currents in rabbit myelinated nerve, *Journal of Physiology* **292**: 149–166.

Chiu, S. Y., Zhou, L., Zhang, C. L. and Messing, A. (1999). Analysis of potassium channel functions in mammalian axons by gene knockouts, *Journal of Neurocytology* **28**(4-5): 349–364.

Cohen, L. T., Richardson, L. M., Saunders, E. and Cowan, R. S. C. (2003). Spatial spread of neural excitation in cochlear implant recipients: comparison of improved ECAP method and psychophysical forward masking, *Hearing Research* **179**: 72–87.

Cohen, L. T., Saunders, E. and Clark, G. M. (2001). Psychophysics of a prototype peri-modiolar cochlear implant electrode array, *Hearing Research* **155**: 63–81.

Cohen, L. T., Saunders, E. and Richardson, L. M. (2004). Spatial spread of neural excitation: comparison of compound action potential and forward-masking data in cochlear implant recipients, *International Journal of Audiology* **43**(6): 346–355.

Cohen, L. T., Saunders, E., Knight, M. R. and Cowan, R. S. C. (2006). Psychophysical measures in patients fitted with Contour™ and straight Nucleus electrode arrays, *Hearing Research* **212**: 160–175.

Colombo, J. and Parkins, C. W. (1987). A model of electrical excitation of the mammalian auditory-nerve neruon, *Hearing Research* **31**: 287–312.

Conning, M. (2006). *Acoustic modelling of cochlear implants*, Master's thesis, University of Pretoria, Pretoria, South Africa.

Deurloo, K. E. I., Holsheimer, J. and Bergveld, P. (2001). The effect of subthreshold prepulses on the recruitment order in a nerve trunk analyzed in a simple and a realistic volume conductor model, *Biological Cybernetics* **85**(4): 281–291.

Devaux, J. J., Kleopa, K. A., Cooper, E. C. and Scherer, S. S. (2004). KCNQ2 is a nodal K^+ channel, *Journal of Neuroscience* **24**(5): 1236–1244.

Dillier, N., Lai, W. K., Almqvist, B., Frohne, C., Müller-Deile, J., Stecker, M. and van Wallenberg, E. (2002). Measurement of the electrically evoked compound action potential via a neural response telemetry system, *Annals of Otology, Rhinology and Laryngology* **111**(5): 407–414.

Dimitrov, A. G. (2005). Internodal sodium channels ensure active processes under myelin manifesting in depolarizing afterpotentials, *Journal of Theoretical Biology* **235**(4): 451–462.

Dynes, S. C. B. and Delgutte, B. (1992). Phase-locking of auditory-nerve discharges to sinusoidal electric stimulation of the cochlea, *Hearing Research* **58**: 79–90.

Etler, C. P., Abbas, P. J., Hughes, M. L., Brown, C. J., Dunn, S. M., Zubrod, L. J. and van Voorst, T. L. (2004). Comparison of psychophysical and electrophysiologic measures of channel interaction, *in* R. T. Miyamoto (ed.), *International Congress Series*, Vol. 1273 of *Cochlear Implants. Proceedings of the VIII International Cochlear Implant Conference, 10-13 May 2004*, Indianapolis, IN, USA, pp. 44–47.

Fayad, J. N. and Linthicum Jr, F. H. (2006). Multichannel cochlear implants: Relation of histopathology to performance, *Laryngoscope* **116**(8): 1310–1320.

Felder, E., Kanonier, G., Scholtz, A., Rask-Andersen, H. and Schrott-Fischer, A. (1997). Quantitative evaluation of cochlear neuronal and computer-aided three-

dimensional reconstruction of spiral ganglion cells in humans with a peripheral loss of nerve fibres, *Hearing Research* **105**: 183–190.

Franck, K. H. and Norton, S. J. (2001). Estimation of psychophysical levels using the electrically evoked compound action potential measured with the neural response telemetry capabilities of Cochlear Corporation's CI24M device, *Ear & Hearing* **22**(4): 289–299.

Frankenhaeuser, B. and Huxley, A. F. (1964). The action potential in the myelinated nerve fibre of *Xenopus laevis* as computed on the basis of voltage clamp data, *Journal of Physiology* **171**: 302–315.

Frijns, J. H. M. and ten Kate, J. H. (1994). A model of myelinated nerve fibres for electrical prosthesis design, *Medical and Biological Engineering and Computing* **32**(4): 391–398.

Frijns, J. H. M., Briaire, J. J. and Grote, J. J. (2001). The importance of human cochlear anatomy for the results of modiolus-hugging multichannel cochlear implants, *Otology & Neurotology* **22**: 340–349.

Frijns, J. H. M., Briaire, J. J. and Schoonhoven, R. (2000). Integrated use of volume conduction and neural models to simulate the response to cochlear implants, *Simulation Practice and Theory* **8**: 75–97.

Frijns, J. H. M., de Snoo, S. L. and Schoonhoven, R. (1995). Potential distributions and neural excitation patterns in a rotationally symmetric model of the electrically stimulated cochlea, *Hearing Research* **87**: 170–186.

Frijns, J. H. M., de Snoo, S. L. and ten Kate, J. H. (1996). Spatial selectivity in a rotationally symmetric model of the electrically stimulated cochlea, *Hearing Research* **95**: 33–48.

Frijns, J. H. M., Mooij, J. and ten Kate, J. H. (1994). A quantitative approach to modeling mammalian myelinated nerve fibers for electrical prosthesis design, *IEEE Transactions on Biomedical Engineering* **41**(6): 556–566.

Geuna, S., Tos, P., Guglielmone, R., Battiston, B. and Giacobini-Robecchi, M. G. (2001). Methodological issues in size estimation of myelinated nerve fibers in peripheral nerves, *Anatomy and Embryology* **203**(6): 1–10.

Glueckert, R., Pfaller, K., Kinnefors, A., Rask-Andersen, H. and Schrott-Fischer, A. (2005a). The human spiral ganglion: New insights into ultrastructure, survival rate and implications for cochlear implants, *Audiology & Neurotology* **10**(5): 258–273.

Glueckert, R., Pfaller, K., Kinnefors, A., Rask-Andersen, H. and Schrott-Fischer, A. (2005b). Ultrastructure of the normal human organ of Corti. New anatomical findings in surgical specimens, *Acta Oto-Laryngologica* **125**(5): 534–539.

Glueckert, R., Pfaller, K., Kinnefors, A., Schrott-Fischer, A. and Rask-Andersen, H. (2005c). High resolution scanning electron microscopy of the human organ of Corti. A study using freshly fixed surgical specimens, *Hearing Research* **199**: 40–56.

Grill, W. M. and Mortimer, J. T. (1995). Stimulus waveforms for selective neural stimulation, *IEEE Engineering in Medicine and Biology Magazine* **14**(4): 375–385.

Grill, W. M. and Mortimer, J. T. (1997). Inversion of the current-distance relationship by transient depolarization, *IEEE Transactions on Biomedical Engineering* **44**(1): 1–9.

Hanekom, T. (2001a). *Modelling of the electrode-auditory nerve fibre interface in cochlear prostheses*, PhD thesis, University of Pretoria, Pretoria, South Africa.

Hanekom, T. (2001b). Three-dimensional spiraling finite element model of the electrically stimulated cochlea, *Ear & Hearing* **22**(4): 300–315.

Hanekom, T. (2005). Modelling encapsulation tissue around cochlear implant electrodes, *Medical and Biological Engineering and Computing* **43**(1): 47–55.

Hartmann, R. and Klinke, R. (1990). Response characteristics of nerve fibers to patterned electrical stimulation, *in* J. M. Miller and F. A. Spelman (eds), *Cochlear implants. Models of the electrically stimulated ear*, Springer-Verlag Inc., New York, chapter 10, pp. 135–160.

Hartmann, R., Topp, G. and Klinke, R. (1982). Comparison of auditory single fiber responses during acoustic and electric stimulation of the intact cat cochlea, *Archives of Oto-Rhino-Laryngology* **234**(2): 187–188.

Hartmann, R., Topp, G. and Klinke, R. (1984). Discharge patterns of cat primary auditory nerve fibers with elecrical stimulation of the cochlea, *Hearing Research* **13**: 47–62.

Hille, B. (2001). *Ionic Channels of Excitable Membrane*, Third edn, Sinauer Associates Inc., Sunderland, Massachusetts.

Hodgkin, A. L. and Huxley, A. F. (1952). A quantitative description of membrane current and its application to conduction and excitation in nerve, *Journal of Physiology* **117**(4): 500–544.

Hong, R. S., Rubinstein, J. T., Wehner, D. and Horn, D. (2003). Dynamic range enhancement for cochlear implants, *Otology and Neurotology* **24**(4): 590–595.

Hossain, W. A., Antic, S. D., Yang, Y., Rasband, M. N. and Morest, D. K. (2005). Where is the spike generator of the cochlear nerve? Voltage-gated sodium channels in the mouse cochlea, *Journal of Neuroscience* **25**(29): 6857–6868.

Huxley, A. F. (1959). Ion movements during nerve activity, *Annals of the New York Academy of Sciences* **81**: 221–246.

Huys, Q. J. M., Ahrens, M. B. and Paninski, L. (2006). Efficient estimation of detailed single-neuron models, *Journal of Neurophysiology* **96**(2): 872–890.

Izhikevich, M. E. (2007). *Dynamical systems in neuroscience: the geometry of excitability and bursting*, First edn, The MIT Press, Cambridge, Massachusetts.

Javel, E. (1990). Acoustic and electrical encoding of temporal information, *in* J. M. Miller and F. A. Spelman (eds), *Cochlear implants. Models of the electrically stimulated ear*, Springer-Verlag Inc., New York, chapter 17, pp. 247–296.

Javel, E. and Shepherd, R. K. (2000). Electrical stimulation of the auditory nerve III. Response initiation sites and temporal fine structure, *Hearing Research* **140**: 45–76.

Javel, E., Tong, Y. C., Shepherd, R. K. and Clark, G. M. (1987). Responses of cat auditory nerve fibers to biphasic electrical current pulses, *Annals of Otology, Rhinology and Laryngology* **96**(Suppl. 128): 26–30.

Jolly, C. N., Spelman, F. A. and Clopton, B. M. (1996). Quadrupolar stimulation for cochlear prostheses: Modeling and experimental data, *IEEE Transactions on Biomedical Engineering* **43**(8): 857–865.

Jönsson, R., Hanekom, T. and Hanekom, J. J. (2008). Initial results from a model of ephaptic excitation in the electrically excited peripheral auditory nervous system, *Hearing Research* **237**: 49–56.

Kiang, N. Y. and Moxon, E. C. (1972). Physiological considerations in artificial stimulation of the inner ear, *Annals of Otology, Rhinology and Laryngology* **81**(5): 714–730.

Kiernan, M. C., Cikurel, K. and Bostock, H. (2001). Effects of temperature on the excitability properties of human motor axons, *Brain* **124**(4): 816–825.

Klinke, R. and Hartmann, R. (1997). Basic neurophysiology of cochlear-implants, *The American Journal of Otology* **18**(6 (Suppl)): S7–S10.

Kral, A., Hartmann, R., Mortazavi, D. and Klinke, R. (1998). Spatial resolution of cochlear implants: the electrical field and excitation of auditory afferents, *Hearing Research* **121**: 11–28.

Lai, W. K. and Dillier, N. (2000). A simple two-component model of the electrically evoked compound action potential in the human cochlea, *Audiology & Neuro-Otology* **5**: 333–345.

Lai, W. K. and Dillier, N. (2008). Comparing neural response telemetry amplitude growth functions with loudness growth functions: Preliminary results, *Ear & Hearing* **28**(2 (Suppl)): 42S–45S.

Lapicque, L. (1907). Recherches quantitatifs sur l'excitation electrique des nerfs traitee comme un polarisation, *Journal of Physiology* **9**: 620–635.

Leake, P. A. and Rebscher, S. J. (2004). Anatomical considerations of electrical stimulation, *in* F. G. Zeng, A. N. Popper and R. R. Fay (eds), *Cochlear Implants: Auditory prostheses and electric hearing*, Vol. 20 of *Springer handbook of audiory research*, Springer-Verlag, New York, chapter 4, pp. 101–148.

Liang, D. H., Lusted, H. S. and White, R. L. (1999). The nerve-electrode interface of the cochlear implant: current spread, *IEEE Transactions on Biomedical Engineering* **46**(1): 35–43.

Linthicum Jr, F. H. and Anderson, W. (1991). Cochlear implantation of totally deaf ears, *Acta Otolaryngology* **111**(2): 327–331.

Loeb, G. E., White, M. W. and Jenkins, W. M. (1983). Biophysical considerations in electrical stimulation of the auditory nervous system, *Annals of the New York Academy of Sciences* **405**: 123–136.

Loizou, P. C. (1998). Mimicking the human ear, *IEEE Signal Processing Magazine* **15**(5): 101–130.

Lowitzsch, K., Hopf, H. C. and Galland, J. (1977). Changes of sensory conduction velocity and refractory periods with decreasing tissue temperature in man, *Journal of Neurology* **216**(3): 181–188.

Macherey, O., Carlyon, R. P., van Wieringen, A. and Wouters, J. (2007). A dual-process integrator-resonator model of the electrically stimulated human auditory nerve, *Journal of the Association for Research in Otolaryngology* **8**(1): 84–104.

Macherey, O., van Wieringen, A., Carlyon, R. P., Deeks, J. M. and Wouters, J. (2006). Asymmetric pulses in cochlear implants: Effects of pulse shape, polarity, and rate, *Journal of the Association for Research in Otolaryngology* **7**(3): 253–266.

Matsuoka, A. J., Abbas, P. J., Rubinstein, J. T. and Miller, C. A. (2000a). The neuronal response to electrical constant-amplitude pulse train stimulation: additive Gaussian noise, *Hearing Research* **149**: 129–137.

Matsuoka, A. J., Abbas, P. J., Rubinstein, J. T. and Miller, C. A. (2000b). The neuronal response to electrical constant-amplitude pulse train stimulation: evoked compound action potential recordings, *Hearing Research* **149**: 115–128.

Matsuoka, A. J., Rubinstein, J. T., Abbas, P. J. and Miller, C. A. (2001). The effects of interpulse interval on stochastic properties of electrical stimulation: models and measurements, *IEEE Transactions on Biomedical Engineering* **48**(4): 416–424.

McIntyre, C. C., Richardson, A. G. and Grill, W. M. (2002). Modeling the excitability of mammalian nerve fibers: Influence of afterpotentials on the recovery cycle, *Journal of Neurophysiology* **87**(2): 995–1006.

McNeal, D. R. (1976). Anaysis of a model for excitation of myelinated nerve, *IEEE Transactions on Biomedical Engineering* **23**(4): 329–337.

Miller, C. A., Abbas, P. J. and Brown, C. J. (1993). Electrically evoked auditory brainstem response to stimulation of different sites in the cochlea, *Hearing Research* **66**: 130–142.

Miller, C. A., Abbas, P. J. and Brown, C. J. (2000). An improved method of reducing stimulus artifact in the electrically evoked whole-nerve potential, *Ear & Hearing* **21**(4): 280–290.

Miller, C. A., Abbas, P. J. and Robinson, B. K. (2001a). Response properties of the refractory auditory nerve fibre, *Journal of the Association for Research in Otolaryngology* **2**(3): 216–232.

Miller, C. A., Abbas, P. J. and Rubinstein, J. T. (1999a). An empirically based model of the electrically evoked compound action potential, *Hearing Research* **135**: 1–18.

Miller, C. A., Abbas, P. J., Hay-McCutcheon, M. J., Robinson, B. K., Nourski, K. V. and Jeng, F. C. (2004). Intracochlear and extracochlear ECAPs suggest antidromic action potentials, *Hearing Research* **198**: 75–86.

Miller, C. A., Abbas, P. J., Nourski, K. V., Hu, N. and Robinson, B. K. (2003). Electrode configuration influences action potential initiation site and ensemble stochastic response properties, *Hearing Research* **175**: 200–214.

Miller, C. A., Abbas, P. J., Robinson, B. K., Rubinstein, J. T. and Matsuoka, A. J. (1999b). Electrically evoked single-fiber action potentials from cat: responses to monopolar, monophasic stimulation, *Hearing Research* **130**: 197–218.

Miller, C. A., Abbas, P. J., Rubinstein, J. T., Robinson, B. K., Matsuoka, A. J. and Woodworth, G. (1998). Electrically evoked compound action potentials of guinea pig and cat: responses to monopolar, monophasic stimulation, *Hearing Research* **119**: 142–154.

Miller, C. A., Robinson, B. K., Rubinstein, J. T., Abbas, P. J. and Runge-Samuelson, C. L. (2001b). Auditory nerve responses to monophasic and biphasic electric stimuli, *Hearing Research* **151**: 79–94.

Miller, C. A., Woodruff, K. E. and Pfingst, B. E. (1995). Functional responses from guinea pigs with cochlear implants. I. Electrophysiological and psychophysical measures, *Hearing Research* **92**: 85–99.

Mo, Z. L., Adamson, C. L. and Davis, R. L. (2002). Dendrotoxin-sensitive K^+ currents contribute to accomodation in murine spiral ganglion neurons, *Journal of Physiology* **542**(3): 763–778.

Mogyoros, I., Kiernan, M. C. and Burke, D. (1996). Strength-duration properties of human peripheral nerve, *Brain* **119**(2): 439–447.

Moore, J. W., Joyner, R. W., Brill, M. H., Waxman, S. D. and Najar-Joa, M. (1978). Simulations of conduction in uniform myelinated fibers. Relative sensitivity to changes in nodal and internodal parameters, *Biophysical Journal* **21**(2): 147–160.

Morse, R. P. and Evans, E. F. (2003). The sciatic nerve of the toad *Xenopus laevis* as a physiological model of the human cochlear nerve, *Hearing Research* **182**: 97–118.

Moxon, E. C. (1971). *Neural and mechanical responses to electric stimulation of the cat's inner ear*, PhD thesis, Massachusetts Institute of Technology, Cambridge, Massachusetts.

Murray, J. A. H., Simpson, J. A. and Weiner, E. S. C. (eds) (1989). *The Oxford English Dictionary*, Second edn, Clarendon Press, Oxford.

Nadol Jr, J. B. (1988). Comparative anatomy of the cochlea and auditory nerve in mammals, *Hearing Research* **34**: 253–266.

Nadol Jr, J. B. (1990). Degeneration of cochlear neurons as seen in the spiral ganglion of man, *Hearing Research* **49**: 141–154.

Nadol Jr, J. B. (1997). Patterns of neural degeneration in the human cochlea and auditory nerve: Implications for cochlear implantation, *Otolaryngology - Head and Neck Surgery* **117**(3): 220–228.

Nadol Jr, J. B. and Xu, W. Z. (1992). Diameter of the cochlear nerve in deaf humans: Implications for cochlear implantation, *Annals of Otology, Rhinology and Laryngology* **101**(12): 988–993.

Nadol Jr, J. B., Burgess, B. J. and Reisser, C. (1990). Morphometric analysis of normal human spiral ganglion cells, *Annals of Otology, Rhinology and Laryngology* **99**(5I): 340–348.

Niparko, J. K. (2004). Cochlear implants: Clinical applications, *in* F. G. Zeng, A. N. Popper and R. R. Fay (eds), *Cochlear Implants: Auditory prostheses and electric hearing*, Vol. 20 of *Springer handbook of audiory research*, Springer-Verlag, New York, chapter 3, pp. 53–100.

Nygren, A. and Halter, J. A. (1999). A general approach to modeling conduction and concentration dynamics in excitable cells of concentric cylindrical geometry, *Journal of Theoretical Biology* **199**(3): 329–358.

O'Leary, S. J., Black, R. C. and Clark, G. M. (1985). Current distributions in the cat cochlea: a modelling and electrophysiological study, *Hearing Research* **18**: 273–281.

Paintal, A. S. (1965). Effects of temperature on conduction in single vagal and saphenous myelinated nerve fibres of the cat, *Journal of Physiology* **180**(1): 20–49.

Paintal, A. S. (1966). The influence of diameter of medullated nerve fibres of cats on the rising and falling phases of the spike and its recovery, *Journal of Physiology* **184**(4): 791–811.

Palti, Y. and Adelman Jr., W. J. (1969). Measurement of axonal membrane conductances and capacity by means of a varying potential control voltage clamp, *Journal of Membrane Biology* **1**(1): 431–458.

Pamulova, L., Linder, B. and Rask-Andersen, H. (2006). Innervation of the apical turn of the human cochlea: A light microscopic and transmission electron microscopic investigation, *Otology & Neurotology* **27**(2): 270–275.

Pfingst, B. E. and Sutton, D. (1983). Relation of cochlear implant function to histopathology in monkeys, *Annals of the New York Academy of Sciences* **405**: 224–239.

Polak, M., Hodges, A. V., King, J. E. and Balkany, T. J. (2004). Further prospective findings with compound action potentials from Nucleus 24 cochlear implants, *Hearing Research* **188**: 104–116.

Ragheb, T. and Geddes, L. A. (1990). Electrical properties of metallic electrodes, *Medical and Biological Engineering and Computing* **28**(2): 182–186.

Ranck Jr, J. B. (1975). Which elements are excited in electrical stimulation of mammalian central nervous system: a review, *Brain Research* **98**(3): 417–440.

Rasband, M. N. (2006). Neuron-glia interactions at the node of Ranvier, *in* E. Gundelfinger, C. Seidenbecher and B. Schraven (eds), *Cell Communication in Nervous and Immune System*, Results and Problems in Cell Differentiation, Springer Berlin / Heidelberg, pp. 129–149.

Rasband, M. N. and Trimmer, J. S. (2001). Developmental clustering of ion channels at and near the node of Ranvier, *Developmental Biology* **236**(1): 5–16.

Rask-Andersen, H., Tylstedt, S., Kinnefors, A. and Schrott-Fischer, A. (1997). Nerve fibre interaction with large ganglion cells in the human spiral ganglion: A TEM study, *Auris Nasus Larynx* **24**(1): 1–11.

Rattay, F. (1987). Ways to approximate current-distance relations for electrically stimulated fibers, *Journal of Theoretical Biology* **125**(3): 339–349.

Rattay, F. (1990). *Electrical nerve stimulation: theory, experiments and applications*, Springer Verlag, Wien, New York.

Rattay, F. and Aberham, M. (1993). Modeling axon membranes for functional electrical stimulation, *IEEE Transactions on Biomedical Engineering* **40**(12): 1201–1209.

Rattay, F., Leao, R. N. and Felix, H. (2001a). A model of the electrically excited human cochlear neuron. II. Influence of the three-dimensional cochlear structure on neural excitability, *Hearing Research* **153**: 64–79.

Rattay, F., Lutter, P. and Felix, H. (2001b). A model of the electrically excited human cochlear neuron I. Contribution of neural substructures to the generation and propagation of spikes, *Hearing Research* **153**: 43–63.

Rattay, F., Resatz, S., Lutter, P., Minassian, K., Jilge, B. and Dimitrijevic, M. R. (2003). Mechanisms of electrical stimulation with neural prostheses, *Neuromodulation* **6**(1): 42–56.

Rebscher, S. J., Snyder, R. L. and Leake, P. A. (2001). The effect of electrode configuration and duration of deafness on threshold and selectivity of responses to intracochlear electrical stimulation, *Journal of the Acoustical Society of America* **109**(5): 2035–2048.

Reid, G., Bostock, H. and Schwarz, J. R. (1993). Quantitative description of action potentials and membrane currents in human node of Ranvier, *Journal of Physiology* **467**: 247P.

Reid, G., Scholz, A., Bostock, H. and Vogel, W. (1999). Human axons contain at least five types of voltage-dependent potassium channel, *Journal of Physiology* **518**(3): 681–696.

Reid, M. A., Flores-Otero, J. and Davis, R. L. (2004). Firing patterns of Type II spiral ganglion neurons *in vitro*, *The Journal of Neuroscience* **24**(3): 733–742.

Röper, J. and Schwarz, J. R. (1989). Heterogeneous distribution of fast and slow potassium channels in myelinated rat nerve fibres, *Journal of Physiology* **416**: 93–110.

Rosbe, K. W., Burgess, B. J., Glynn, R. J. and Nadol Jr, J. B. (1996). Morphologic evidence for three cell types in the human spiral ganglion, *Hearing Research* **93**: 120–127.

Rubinstein, J. T. (1993). Axon termination conditions for electrical stimulation, *IEEE Transactions on Biomedical Engineering* **40**(7): 654–663.

Rubinstein, J. T. (1995). Threshold fluctuations in an N sodium channel model of the node of Ranvier, *Biophysical Journal* **68**(3): 779–785.

Rubinstein, J. T., Miller, C. A., Mino, H. and Abbas, P. J. (2001). Analysis of monophasic and biphasic electrical stimulation of nerve, *IEEE Transactions on Biomedical Engineering* **48**(10): 1065–1070.

Rubinstein, J. T., Wilson, B. S., Finley, C. C. and Abbas, P. J. (1999). Pseudospontaneous activity: stochastic independence of auditory nerve fibers with electrical stimulation, *Hearing Research* **127**: 108–118.

Runge-Samuelson, C. L., Abbas, P. J., Rubinstein, J. T., Miller, C. A. and Robinson, B. K. (2004). Response of the auditory nerve to sinusoidal electrical stimulation: effects of high-rate pulse trains, *Hearing Research* **194**: 1–13.

Safronov, B. V., Kampe, K. and Vogel, W. (1993). Single voltage-dependent potassium channels in rat peripheral nerve membrane, *Journal of Physiology* **460**: 675–691.

Salzer, J. L. (1997). Clustering sodium channels at the node of Ranvier: Close encounters of the axon-glia kind, *Neuron* **18**(6): 843–846.

Saunders, E., Cohen, L. T., Aschendorff, A., Shapiro, W., Knight, M., Stecker, M., Richter, B., Waltzman, S., Tykocinski, M., Roland, T., Laszig, R. and Cowan, R. S. C. (2002). Threshold, comfortable level and impedance changes as a function of electrode-modiolar distance, *Ear & Hearing* **23**(1S): 28S–40S.

Schalow, G., Zäch, G. A. and Warzok, R. (1995). Classification of human peripheral nerve fibre groups by conduction velocity and nerve fibre diameter is preserved following spinal cord lesion, *Journal of the Autonomic Nervous System* **52**(2-3): 125–150.

Scherer, S. S. and Arroyo, E. J. (2002). Recent progress on the molecular organization of myelinated axons, *Journal of the Peripheral Nervous System* **7**(1): 1–12.

Scholz, A., Reid, G., Vogel, W. and Bostock, H. (1993). Ion channels in human axons, *Journal of Neurophysiology* **70**(3): 1274–1279.

Schuknecht, H. F. (1993). *Pathology of the ear*, Second edn, Lea and Febiger, Philadelphia.

Schwarz, J. R. and Eikhof, G. (1987). Na currents and action potentials in rat myelinated nerve fibres at 20 and 37 °C, *Pflügers Archiv: European Journal of Physiology* **409**: 569–577.

Schwarz, J. R., Glassmeier, G., Cooper, E. C., Kao, T. C., Nodera, H., Tabuena, D., Kaji, R. and Bostock, H. (2006). KCNQ channels mediate I_{Ks}, a slow K^+ current regulating excitability in the rat node of Ranvier, *Journal of Physiology* **573**(1): 17–34.

Schwarz, J. R., Reid, G. and Bostock, H. (1995). Action potentials and membrane currents in the human node of ranvier, *Pflügers Archiv: European Journal of Physiology* **430**(2): 283–292.

Shannon, R. V. (1985). Threshold and loudness functions for pulsatile stimulation of cochlear implants, *Hearing Research* **18**: 135–143.

Shannon, R. V. (1989). A model of threshold for pulsatile electrical stimulation of cochlear implants, *Hearing Research* **40**: 197–204.

Shannon, R. V., Fu, Q. J., Galvin III, J. J. and Friesen, L. (2004). Speech perception with cochlear implants, *in* F. G. Zeng, A. N. Popper and R. R. Fay (eds), *Cochlear Implants: Auditory prostheses and electric hearing*, Vol. 20 of *Springer handbook of audiory research*, Springer-Verlag, New York, chapter 8, pp. 334–376.

Shepherd, R. K. and Javel, E. (1997). Electrical stimulation of the auditory nerve. I. Correlation of physiological responses with cochlear status, *Hearing Research* **108**: 112–144.

Shepherd, R. K. and Javel, E. (1999). Electrical stimulation of the auditory nerve: II. Effect of stimulus waveshape on single fibre response properties, *Hearing Research* **130**: 171–188.

Shepherd, R. K., Hatshushika, S. and Clark, G. M. (1993). Electrical stimulation of the auditory nerve: the effect of electrode position on neural excitation, *Hearing Research* **66**: 108–120.

Smith, R. L. and Brachman, M. L. (1982). Adaptation in auditory-nerve fibers: A revised model, *Biological Cybernetics* **44**(2): 107–120.

Spelman, F. A., Clopton, B. M. and Pfingst, B. E. (1982). Tissue impedance and current flow in the implanted ear. Implications for the cochlear prosthesis, *The Annals of Otology, Rhinology & Laryngology. Supplement* **98**(91): 3–8.

Spoendlin, H. and Schrott, A. (1989). Analysis of the human auditory nerve, *Hearing Research* **43**: 25–38.

Stephanova, D. I. and Daskalova, M. (2005a). Differences in potentials and excitability properties in simulated cases of demyelinating neuropathies. Part II. Paranodal demyelination, *Clinical Neurophysiology* **116**(5): 1159–1166.

Stephanova, D. I. and Daskalova, M. (2005b). Differences in potentials and excitability properties in simulated cases of demyelinating neuropathies. Part III. Paranodal internodal demyelination, *Clinical Neurophysiology* **116**(10): 2334–2341.

Stephanova, D. I., Daskalova, M. and Alexandrov, A. S. (2005). Differences in potentials and excitability properties in simulated cases of demyelinating neuropathies. Part I, *Clinical Neurophysiology* **116**(5): 1153–1158.

Taylor, J. T., Burke, D. and Heywood, J. (1992). Physiological evidence for a slow K^+ conductance in human cutaneous afferents, *Journal of Physiology* **453**: 575–589.

Townshend, B. and White, R. L. (1987). Reduction of electrical interaction in auditory prostheses, *IEEE Transactions on Biomedical Engineering* **34**(11): 891–897.

Tykocinski, M., Cohen, L. T., Pyman, B. C., Roland, T., Treaba, C., Palamara, J., Dahm, M. C., Shepherd, R. K., Xu, J., Cowan, R. S. C., Cohen, N. L. and Clark, G. M. (2000). Comparison of electrode position in the human cochlea using various perimodiolar electrode arrays, *The American Journal of Otology* **21**(2): 205–211.

Tylstedt, S. and Rask-Andersen, H. (2001). A 3-D model of membrane specializations between human auditory spiral ganglion cells, *Journal of Neurocytology* **30**(6): 465–473.

Vabnick, L. and Shrager, P. (1998). Ion channel redistribution and function during development of the myelinated axon, *Journal of Neurobiology* **37**(1): 80–96.

Vabnick, L., Trimmer, J. S., Schwarz, T. L., Levinson, S. R., Risal, D. and Shrager, P. (1999). Dynamic potassium channel distributions during axonal development prevent aberrant firing patterns, *Journal of Neuroscience* **19**(2): 747–758.

Van den Honert, C. and Stypulkowski, P. H. (1984). Physiological properties of the electrically stimulated auditory nerve. II. Single fiber recordings, *Hearing Research* **14**: 225–243.

Van den Honert, C. and Stypulkowski, P. H. (1987a). Single fiber mapping of spatial excitation patterns in the electrically stimulated auditory nerve, *Hearing Research* **29**: 195–206.

Van den Honert, C. and Stypulkowski, P. H. (1987b). Temporal response patterns of single auditory nerve fibers elicited by periodic electrical stimuli, *Hearing Research* **29**: 207–222.

van der Heijden, M. and Kohlrausch, A. (1994). Using an excitation-pattern model to predict auditory masking, *Hearing Research* **80**: 38–52.

Van Wieringen, A., Carlyon, R. P., Laneau, J. and Wouters, J. (2005). Effects of waveform shape on human sensitivity to electrical stimulation of the inner ear, *Hearing Research* **200**: 73–86.

Van Wieringen, A., Carlyon, R. P., Macherey, O. and Wouters, J. (2006). Effects of pulse rate on thresholds and loudness of biphasic and alternating monophasic pulse trains in electrical hearing, *Hearing Research* **220**: 49–60.

Vanpoucke, F. J., Zarowski, A. J. and Peeters, S. A. (2004). Identification of the impedance model of an implanted cochlear prosthesis from intracochlear potential measurements, *IEEE Transactions on Biomedical Engineering* **51**(12): 2174–2183.

Waxman, S. G. (2000). The neuron as a dynamic electrogenic machine: modulation of sodium-channel expression as a basis for functional plasticity in neurons, *Philo-*

sophical Transactions of the Royal Society of London Series B Biological Sciences **355**(1394): 199–213.

Weiss, G. (1901). Sur la possibilité de rendre comparables entre eux les appareils servant a l'excitation électrique, *Archives Italiennes de Biologie* **35**: 413–446.

Wesselink, W. A., Holsheimer, J. and Boom, H. B. K. (1999). A model of the electrical behaviour of myelinated sensory nerve fibres based on human data, *Medical and Biological Engineering and Computing* **37**(1): 228–235.

White, J. A., Rubinstein, J. T. and Kay, A. R. (2000). Channel noise in neurons, *Trends in Neurosciences* **23**(3): 131–137.

Zhang, X., Heinz, M. G., Bruce, I. C. and Carney, L. H. (2001). A phenomenological model for the responses of auditory-nerve fibers: I. Nonlinear tuning with compression and suppression, *Journal of the Acoustical Society of America* **109**(2): 648–670.

Zimmermann, C. E., Burgess, B. J. and Nadol Jr, J. B. (1995). Patterns of degeneration in the human cochlear nerve, *Hearing Research* **90**: 192–201.

Addendum A

ADDITIONAL TEMPORAL CHARACTERISTICS

The model of the human Type I ANF developed in this study is verified against measured temporal characteristic data from literature. In Chapter 2 a review is presented on the temporal characteristics investigated in this study. For the sake of completeness, the temporal characteristics not covered are briefly reviewed in this addendum. These are:

1. discharge rate
2. adaptation
3. alternation
4. entrainment, also referred to as time-locking
5. phase-locking
6. synchronisation

A.1 DISCHARGE RATE

Discharge rate refers to the rate at which APs (also referred to as spikes) are elicited from a fibre given a specific input pulse train stimulus. In single-fibre studies of cat auditory neurons Moxon (1971) reported direct activation in response to pulsatile and sinusoidal electrical stimuli. Responses to pulsatile stimuli included *a*) an initial short latency ($<$ 1.0 ms) and high firing rates (of up to 900 Hz); and *b*) an adaptation rate of tens of seconds to lower (up to 480 Hz) firing rates. Responses to sinusoidal stimuli included *a*) a very fast increase in firing rate for a small increase in stimulus intensity; *b*) a gradual threshold change with frequency; *c*) at high stimulus frequencies the appearance of a quasi-periodic firing which is not related to the stimulus period; and *d*) at high frequencies the occurrence of a substantial firing rate adaptation.

Interval histograms by Dynes and Delgutte (1992) indicated that at high stimulus frequencies ($>$ 1.0 kHz) fibres show regular discharging in response to sinusoidal waves, similar to what has been seen in low-frequency studies. However, owing to the variation in interspike intervals that correspond to many stimulus cycles, high-frequency electrical stimulation causes fewer regular discharge responses than low-frequency stimulation. Javel (1990) also reported a decrease in discharge rate as the pulse rate of pulse train stimuli increased from 100 to 800 pps. The regularity of fibre discharge thus depends on both the stimulus frequency and stimulation mode, with discharge responses due to high-frequency stimulation falling between the irregular responses observed with high-frequency acoustic stimulation and regular responses observed with low-frequency electrical stimulation. These observations may be explained by the notion that repeated stimulation causes partial refractoriness in fibres, but other phenomena such as adaptation effects cannot be ruled out (Miller *et al.*, 2001a).

Discharge rate also increases for increasing stimulus intensities. Javel *et al.* (1987) observed this for biphasic pulse-trains and interpreted this as implying that *a*) the increase in discharge growth rate with increasing stimulus intensity does not differ much with pulse rate presentation; and *b*) the discharge rate depends on the stimulus intensity and not on pulse rate. They attributed this to the build-up of stimulus intensity and neural refractoriness.

A.2 ADAPTATION

Adaptation refers to the behaviour of fibres, after excitation with a long duration pulse train, initially to start firing action potentials at a high discharge rate and, after a certain time period, which can be as long as a few seconds in some cases, start to reduce their discharge rate until a steady state is reached, i.e. reduced responsiveness to stimuli. Smith and Brachman (1982) attributed adaptation partly to hair cell synapses, but electrical stimulation can cause adaptation, even though it bypasses the synapses. This suggests that a different mechanism may be causing the adaptation effect seen in electrical stimulation.

Adaptation is observed in fibres stimulated with high-frequency pulse trains (Moxon, 1971). Responses to high-frequency pulsatile and sinusoidal stimuli initially show high firing rates (of up to 900 Hz), after which a substantial firing rate adaptation of tens of seconds to lower (up to 480 Hz) firing rates occur. Fibre discharge rates rise quickly with increasing stimulus intensity up to as high as 900 pps for the first few seconds, dropping thereafter to a more steady state rate of 500 pps. With shorter pulse trains even higher discharge rates can be obtained. The same trend in discharge rate is also observed by Van den Honert and Stypulkowski (1987b) for sinusoidal stimuli of up to 2.0 kHz stimulus frequency. Javel (1990) observed adaptation in fibres stimulated with biphasic pulses of long phase duration at 200 Hz stimulation rate. The adaptation effect is greatest for stimulation intensities falling in the dynamic ranges of the fibres, while at high stimulation intensities, fibres prove to respond to every stimulus pulse and the adaptation effect disappears. It is concluded that not all adaptation effects originate from hair cell / fibre synapses, but that some adaptation effects in electrical stimulation originate in the spiral ganglion cell.

The adaptation effect only exists over a narrow intensity range. Dynes and Delgutte (1992) observed adaptation of between 25% and 80% at high stimulus frequencies ($>$ 1.0 kHz) for sinusoidal electrical stimulation. Their results also indicate a considerable inter-fibre variability in adaptation behaviour over time. Similar adaptation effects are also observed by Shepherd and Javel (1997) for biphasic stimuli in normal, short-term and long-term deafened cats.

Although not used in the true sense of the word, adaptation-like effects are observed for monopolar, monophasic stimulation of cat fibres, showing a reduction in respon-

siveness to stimuli after some time of continuous stimulation has transpired (Miller *et al.*, 1999b). The reduction in responsiveness is more evident with anodic than with cathodic stimuli and resulted in an upward threshold shift of 0.85 dB for anodic and 0.28 dB for cathodic stimulation with time. ECAP simulation results with an empirically based model based on cat fibre data confirmed the more pronounced adaptation effects with anodic stimuli (Miller *et al.*, 1999a). The effect is thought to be due to refractoriness of the neural membrane as a result of prior stimulation rate. When the simulation rate is decreased, the responsiveness returns to levels prior to stimulation at the higher rate. Similar adaptation-like effects have been observed previously, but usually for shorter interpulse intervals (IPIs) (see for example Van den Honert and Stypulkowski, 1984; Van den Honert and Stypulkowski, 1987a).

A.3 ALTERNATION

In addition to the adaptation observed in electrically stimulated auditory nerve fibres, an alternation in response probability between successive stimulus pulses has been observed. Javel (1990) observed alternation with biphasic stimulus pulses in fibres when the stimulation rates exceed the maximum possible discharge rate of the fibre. The alternation appears to converge to an intermediate response probability steady state after a few tens of milliseconds. The effect is attributed to neural membrane refractoriness. Alternation in short-term deafened fibre responses due to biphasic stimuli is observed by Shepherd and Javel (1997) in fibres which show a reduction in entrainment for stimulus rates greater than 400 pps. Almost no alternation is observed in fibres having 100% entrainment for stimulus rates up to the tested 800 pps.

Matsuoka *et al.* (2000b) observed alternation in cat and guinea-pig ECAP responses for fibres stimulated with pseudomonophasic constant-amplitude pulse trains. Results indicate that amplitude alternation is stimulus intensity, polarity and IPI dependent. In cats, the maximum alternation amplitude increases with an increase in stimulus intensity. For cathodic stimuli maximum alternation amplitudes are observed at IPIs about 1.0 ms longer than with anodic stimulation, while more alternation is observed with cathodic than with anodic stimuli. This can be attributed to the combined effects of across-fibre synchronous responses and refractory properties of the stimulated fibres, with maximum alternation amplitude occurring when the pulse train's IPI falls

within the fibre's RRP. Furthermore, the persistence of the alternation pattern probably relates to the stochastic nature of the fibre, with reduced stochasticity resulting in a more persistent pattern. In guinea-pigs amplitude alternation is more pronounced than in cats, but polarity effects are not as clearly observable as in cats. These differences are attributed to the difference in cochlear structure between the two species which results in a difference in fibre excitation sites. The addition of Gaussian noise to the input constant-amplitude pulse train signal results in reversible across-fibre desynchonisation and hence reduced amplitude alternation (Matsuoka, Abbas, Rubinstein and Miller, 2000a). However, the added noise does not have an adaptive effect on the ECAP response amplitude, since its effect is only sub-threshold.

A.4 ENTRAINMENT, ALSO REFERRED TO AS TIME-LOCKING

An acoustic tone presented to an auditory nerve fibre will, if it is presented at a low enough frequency, cause the fibre's discharges to become partially entrained (time-locked) to the stimulus period. This means that intervals between successive discharges will synchronise around integer multiples of the stimulation period (see Javel *et al.*, 1987). Entrainment that is similar to acoustic entrainment is reported for fibres from normal cochleae (Javel *et al.*, 1987; Javel, 1990), except that for electrical stimulation, the degree of entrainment is much higher than for acoustic stimulation. Also, for high stimulus intensities at pulse rates exceeding 800 pps, the fibre's discharges are entrained to the period of the stimulus and the discharge rate will never exceed that of the stimulus. In short-termed deafened animals, Shepherd and Javel (1997) found 100% entrainment in some fibres for stimulus pulse rates of up to 800 pps, while in most others, 100% entrainment only occurred for stimulus pulse rates of up to 400 pps. At higher stimulus rates, activity will switch between 100% entrainment and periods of complete inactivity. Difficulty in following high stimulus rates at 100% entrainment is also observed in long-term deafened animals (Shepherd and Javel, 1997).

A.5 PHASE-LOCKING

Phase-locking to the formant frequencies in a speech signal have proved to be an important cue for speech discrimination. Several studies show that the auditory fibres phase-lock to sinusoidal and pulse train stimuli for frequencies below 1.0 kHz (Kiang and Moxon, 1972; Javel *et al.*, 1987; Van den Honert and Stypulkowski, 1987b; Javel, 1990).

At high stimulus frequencies ($>$ 1.0 kHz), discharges tend to be only moderately phase-locked to the stimulus, unlike the phase-locked response to low-frequency stimuli, not displaying the sharp peak in the period histograms but rather a roughly sinusoidal shape (Dynes and Delgutte, 1992).

For low-frequency, large amplitude, bipolar sinusoidal stimulation, Van den Honert and Stypulkowski (1987b) reported discharges during both the opposite phases of the signal, with sometimes even multiple discharges during one half cycle. At threshold, however, discharges occur for only one of the phases. They attributed this to a difference in excitation sites along the fibre for the opposite phases. Stimulation with triangular and square pulses shows the same behaviour, although the threshold current needed is always highest for triangular pulses and lowest for square pulses for a given frequency. At frequencies below 200 Hz double-peak responses are often seen within the same phase, but sometimes even in both phases. The points within the phases where the responses occur only show very small variations with stimulus intensity, with those for sinusoidal and triangular pulses similar in timing and stimulus intensity dependence. Responses to square pulses differ from those to sinusoidal and triangular pulses. The dominant response peak has a higher synchrony, appears in a different phase and shifts between phases with increasing stimulus intensity. Jitter and discharge rate also vary non-monotonically with increasing stimulus intensity. Dynes and Delgutte (1992) also reported less frequent responses to opposite stimulus phases at high-frequency stimulation and concluded that the origin of this effect is not clear.

A.6 SYNCHRONISATION

Synchronisation refers to the tendency of an ensemble of fibres to fire in synchrony. Kiang and Moxon (1972) and Hartmann *et al.* (1984) reported spike fire synchronisation to electrically delivered sinusoidal stimuli with an increase in synchronisation as the stimulus intensity increases. This tendency is confirmed by Van den Honert and Stypulkowski (1984) and Javel *et al.* (1987) who reported an increase in synchronisation, together with an increase in FE, with an increase in pulsatile electrical stimulus intensity in normal hearing and acutely deafened cats respectively. In cats that had undergone a laminectomy, synchronous firing occurs even at low stimulus intensities, with no spontaneous activity present. Observations by Miller *et al.* (1999b) on latency, jitter and FE with monopolar, monophasic stimuli of acutely deafened cats also suggest an increase in synchronisation and FE.

Synchronisation also decreases as the stimulus frequency is increased. Results reported by Van den Honert and Stypulkowski (1987b) indicate that at high frequencies (> 500 Hz), fibres do not fire at each stimulus cycle of the sinusoidal stimulus signal.

Since synchronisation decreases the dynamic range of the implantee, a decrease in synchronisation may lead to an increase in dynamic range. Rubinstein *et al.* (1999) introduced pseudospontaneous activity, and hence less synchrony, in fibres through electrical stimulation with a sufficiently high rate. Runge-Samuelson, Abbas, Rubinstein, Miller and Robinson (2004) confirmed the possibility of simulating increased spontaneous nerve fibre activity in cats and guinea-pigs with electrical stimulation by adding a high rate conditioner to sinusoidal stimuli. The results from a study by Runge-Samuelson *et al.* (2004) confirm the results of a similar study by Hong, Rubinstein, Wehner and Horn (2003) performed on humans that decreased synchrony leads to a dynamic range increase in implantees by lowering thresholds.